

AD-A166 468

OPTICAL PROPERTIES OF BLOW-OFF PARTICULATES(U)

1/2

INSTITUTE OF PAPER CHEMISTRY APPLTTON NIS

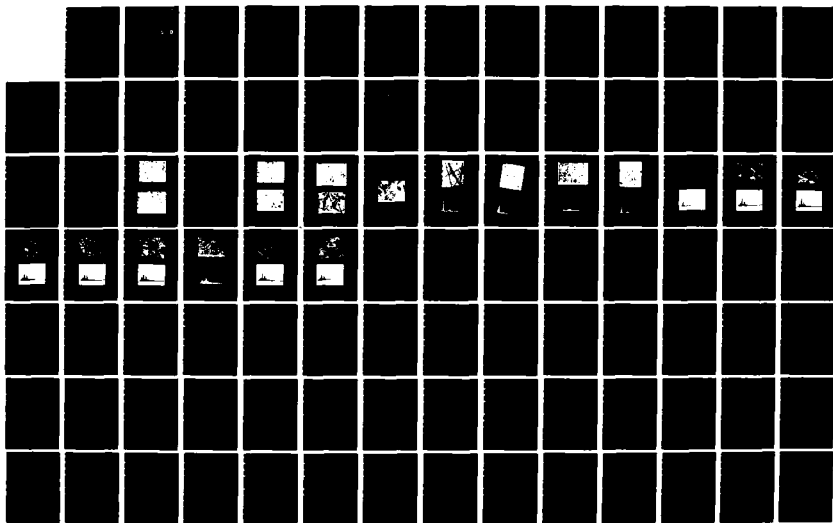
E J DAVIS ET AL 29 FEB 84 DNA-RR-84-69

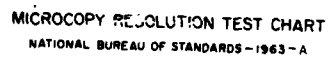
UNCLASSIFIED

DNA011-82-C-0224

F/G 20/6

NL





MICROCOPY RESOLUTION TEST CHART
NATIONAL BUREAU OF STANDARDS-1963-A

AD-A166 460



DNA-TR-84-69

OPTICAL PROPERTIES OF BLOW-OFF PARTICULATES

**Earl J. Davis
Ravindran Periasamy
University of Washington
Department of Chemical Engineering
Seattle, WA 98195**

29 February 1984

**DTIC
ELECTE
APR 10 1986
S D**

Technical Report

CONTRACT No. DNA 001-82-C-0224

**Approved for public release;
distribution is unlimited.**

**THIS WORK WAS SPONSORED BY THE DEFENSE NUCLEAR AGENCY
UNDER RDT&E RMSS CODE B344082466 X99QAXSG00046 H2590D.**

**Prepared for
Director
DEFENSE NUCLEAR AGENCY
Washington, DC 20305-1000**

DTIC FILE COPY

86 1 08 063

UNCLASSIFIED

SECURITY CLASSIFICATION OF THIS PAGE

AD A166460

REPORT DOCUMENTATION PAGE

1a. REPORT SECURITY CLASSIFICATION UNCLASSIFIED			1b. RESTRICTIVE MARKINGS		
2a. SECURITY CLASSIFICATION AUTHORITY			3. DISTRIBUTION/AVAILABILITY OF REPORT Approved for public release; distribution is unlimited.		
2b. DECLASSIFICATION/DOWNGRADING SCHEDULE N/A since UNCLASSIFIED			5. MONITORING ORGANIZATION REPORT NUMBER(S) DNA-TR-84-69		
4. PERFORMING ORGANIZATION REPORT NUMBER(S) IPC Project 3485; UW Project 65-4319			7a. NAME OF MONITORING ORGANIZATION Director Defense Nuclear Agency		
6a. NAME OF PERFORMING ORGANIZATION University of Washington		6b. OFFICE SYMBOL (If applicable)	7b. ADDRESS (City, State, and ZIP Code) Washington, DC 20305-1000		
6c. ADDRESS (City, State, and ZIP Code) Department of Chemical Engineering Mail Stop BF-10 Seattle, Washington 98195		9. PROCUREMENT INSTRUMENT IDENTIFICATION NUMBER DNA 001-82-C-0224			
9a. NAME OF FUNDING/SPONSORING ORGANIZATION		8b. OFFICE SYMBOL (If applicable)	10. SOURCE OF FUNDING NUMBERS		
8c. ADDRESS (City, State, and ZIP Code)		PROGRAM ELEMENT NO 62715H	PROJECT NO X99QAXS	TASK NO G	WORK UNIT ACCESSION NO DH006209
11. TITLE (Include Security Classification) OPTICAL PROPERTIES OF BLOW-OFF PARTICULATES					
12. PERSONAL AUTHOR(S) Earl James Davis and Ravindran Periasamy					
13a. TYPE OF REPORT Technical		13b. TIME COVERED FROM 820801 TO 840131		14. DATE OF REPORT (Year, Month, Day) 1984, February 29	
15. PAGE COUNT 112					
16. SUPPLEMENTARY NOTATION This work was sponsored by the Defense Nuclear Agency under RDT&E RMSS Code B344082466 X99QAXSG00046 H2590D.					
17. COSATI CODES			18. SUBJECT TERMS (Continue on reverse if necessary and identify by block number)		
FIELD 20	GROUP 6	SUB-GROUP 4	Aerosols Complex Refractive Index Optical Properties		
			Albedo Dust Thermal Dust		
			Blow-Off Particulates Light-Scattering		
19. ABSTRACT (Continue on reverse if necessary and identify by block number) The results of the second phase of baseline studies on the electromagnetic scattering properties of dust particles generated in simulated nuclear explosions are presented. Using techniques and equipment developed by the Principal Investigator, complex refractive indices, particle sizes, and albedos of thermal dust particulates were measured as a function of the wavelength of the laser light source. The particulates were obtained from solar furnace experiments performed by Science Applications, Inc. under a separate contract. <i>Keywords: Light scattering</i>					
20. DISTRIBUTION/AVAILABILITY OF ABSTRACT <input type="checkbox"/> UNCLASSIFIED/UNLIMITED <input checked="" type="checkbox"/> SAME AS RPT. <input type="checkbox"/> DTIC USERS			21. ABSTRACT SECURITY CLASSIFICATION UNCLASSIFIED		
22a. NAME OF RESPONSIBLE INDIVIDUAL Betty L. Fox			22b. TELEPHONE (Include Area Code) (202) 325-7042		22c. OFFICE SYMBOL DNA/STTI

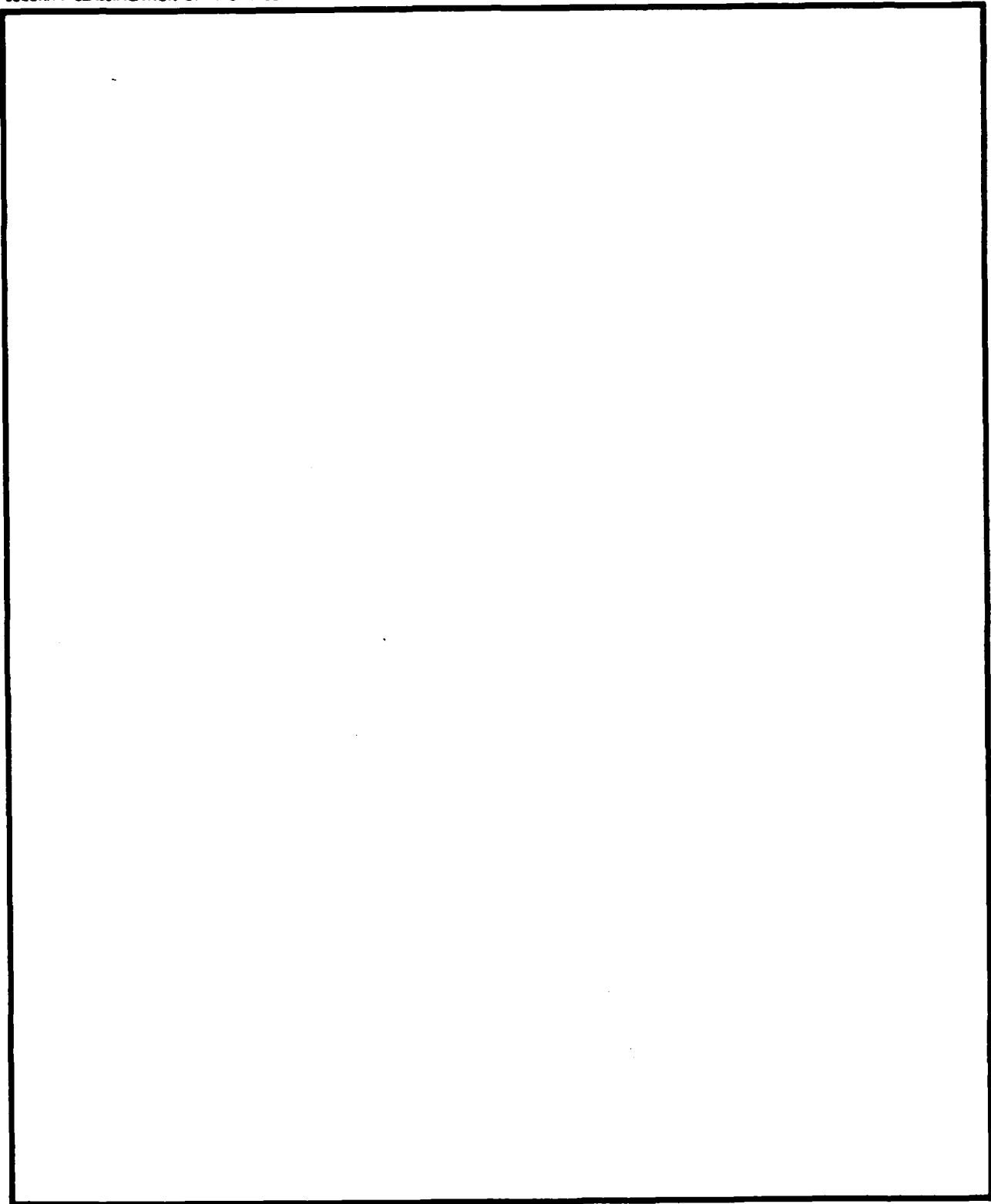
DD FORM 1473, 84 MAR

33 APR edition may be used until exhausted
All other editions are obsolete.

SECURITY CLASSIFICATION OF THIS PAGE

UNCLASSIFIED

UNCLASSIFIED
SECURITY CLASSIFICATION OF THIS PAGE



SECURITY CLASSIFICATION OF THIS PAGE
UNCLASSIFIED

SUMMARY

This document is a report of the measurements of the light-scattering properties of blow-off particulates generated in simulated thermonuclear blasts. The thermal dust particles studied were generated in experiments performed by Science Applications Inc. under a separate DNA contract, using a solar furnace in Odeillo, France. The samples obtained from Science Applications Inc. consisted of filters, wall-wipings and loose dust taken from various locations in the solar furnace, and they correspond to several soil samples placed in the furnace for the tests.

The data reported include particle size, complex refractive index and albedo measurements obtained for three wavelengths of light in the visible (blue-green) range of the spectrum of electromagnetic radiation; 457.9, 488.0 and 514.5 nm. Earlier, measurements were made at 632.8 nm. These light-scattering data were obtained by suspending single, charged particles in an electrodynamic balance in the path of a polarized laser beam. The equipment, techniques and methods of data analysis are outlined herein.

The light-scattering data are supplemented by scanning electron micrographs (SEM) and EDAX (energy dispersive x-ray spectrometry) analyses, which provide information on the sizes, shapes and chemical composition of the particles. The EDAX analyses indicate that most of the dust studied was mixed silicates of aluminum, calcium, iron and potassium. Particle dimensions ranged from about 0.5 μm to 100 μm . The complex refractive index ($m = m_1 - im_2$) was found to have a real component, m_1 , in the range 1.481 - 1.723, which is consistent with available data on the bulk refractive index of silicates and clays. The imaginary component, m_2 , was small ($m_2 < 0.06$) compared with results available for highly absorbing particulates such as carbon particles ($m_2 = 0.6 - 1.0$). The particle albedos were found to be in the range 0.49 - 0.99.

PREFACE

The work reported here represents Phase II of baseline studies on the light-scattering properties of blow-off particulates. Phase I involved the development and testing of equipment, techniques and computer software, and the results of Phase I were summarized in Report number DNA 6274F, dated April 1983. That initial work was supported under Contract Number DNA 001-80-C-0213.

Phase II was continued at the Institute of Paper Chemistry (IPC) in Appleton, Wisconsin, but in August 1983 the Principal Investigator, Dr. E. James Davis, joined the faculty of chemical engineering at the University of Washington. His light-scattering laboratory was re-established at the University, and the research on Phase II was continued there under a subcontract with IPC.

This research provides information on the scattering and absorption properties in the visible region of the spectrum of electromagnetic radiation needed to interpret and assess field measurements of dust particles generated in a simulated thermonuclear explosion.

CONVERSION TABLE

To convert from	to	multiply by
Å, Angstrom Units	m, meters	1.0E-10
µm, micrometers	m, meters	1.0E-06
nm, nanometers	m, meters	1.0E-09

Accession For	
NTIS CRA&I	<input checked="" type="checkbox"/>
DTIC TAB	<input type="checkbox"/>
Unannounced	<input type="checkbox"/>
Justification:	
By	
Distribution /	
Availability Codes	
Dist	Avail and/or Special
A-1	



TABLE OF CONTENTS

<u>Section</u>	<u>Page</u>
SUMMARY	1
PREFACE	2
CONVERSION TABLE	3
LIST OF ILLUSTRATIONS	5
LIST OF TABLES	10
1 OBJECTIVES	11
1.1 BACKGROUND	11
1.1.1 Light Scattering Theory	11
1.1.2 Principles of the Electrodynamic Balance ..	15
2 THE EXPERIMENTAL APPARATUS AND DATA ANALYSIS	18
2.1 THE EXPERIMENTAL SYSTEM	18
2.2 INTERPRETATION OF THE DATA	21
3 RESULTS	24
3.1 SAMPLE IDENTIFICATION	24
3.2 ELECTRON MICROSCOPY	24
3.3 LIGHT SCATTERING PHASE FUNCTIONS	45
4 DISCUSSION OF RESULTS	56
<u>APPENDIX</u>	
I EXPERIMENTAL PHASE FUNCTION DIAGRAMS FOR THE DUST PARTICLES	63

LIST OF ILLUSTRATIONS

<u>Figure</u>		<u>Page</u>
1	The dependence of scattered intensity I_s , on optical size α and angle θ for a refractive index $m = 1.696 - i0.0$	13
2	The effects of scattering angle θ and m_2 on the scattering intensity for $m_1 = 1.55$ and $\alpha = 10.0$	14
3	The electrodynamic balance/light scattering photometer and peripheral equipment	16
4	An exploded view of the electrodynamic balance	16
5	The electric circuitry for the picobalance	18
6	Raw light scattering data from a dust particle, $\lambda = 457.9$ nm	20
7	An SEM of loose dust from Run 57	26
8	An SEM of wall wipings from Run 57	26
9	An SEM of loose dust from Run 69	28
10	An SEM of loose dust from Run 1180	28
11	An SEM of wall wipings from Run 136 at lower magnification (X200)	29
12	An SEM of wall wipings from Run 136 for a magnification (X1000)	29
13	An SEM of wall wipings from Run 136 at high magnification (X2400)	30
14a	An SEM for a bottom filter from Run 57	31
14b	An elemental analysis (EDAX) for a bottom filter from Run 57	31
15a	An SEM for a wall wiping from Run 57	32
15b	An elemental analysis for a wall wiping from Run 57 ..	32
16a	An SEM for a wall wiping from Run 60	33
16b	An elemental analysis for a wall wiping from Run 60 ..	33
17a	An SEM for a wall wiping from Run 69	34
17b	An elemental analysis for a wall wiping from Run 69 ..	34
18a	An SEM for a bottom filter from Run 69	35
18b	An elemental analysis for a bottom filter from Run 69 .	35

LIST OF ILLUSTRATIONS

<u>Figure</u>		<u>Page</u>
19a	An SEM for a wall wiping from Run 101	36
19b	An elemental analysis for a wall wiping from Run 101 .	36
20a	An SEM for a wall wiping from Run 104	37
20b	An elemental analysis for a wall wiping from Run 104 .	37
21a	An SEM for a wall wiping from Run 107	38
21b	An elemental analysis for a wall wiping from Run 107 .	38
22a	An SEM for a wall wiping from Run 108	39
22b	An elemental analysis for a wall wiping from Run 108 .	39
23a	An SEM for a wall wiping from Run 136	40
23b	An elemental analysis for a wall wiping from Run 136 .	40
24a	An SEM for a wall wiping from Run 138	41
24b	An elemental analysis for a wall wiping from Run 138 .	41
25a	An SEM for a wall wiping from Run 147	42
25b	An elemental analysis for a wall wiping from Run 147 .	42
26a	An SEM for a wall wiping from Run 1180	43
26b	An elemental analysis for a wall wiping from Run 1180 .	43
27	Experimental phase function data for a particle from Run 60 for $\lambda = 457.9$ nm compared with Mie Theory for $\alpha = 5.01$ and $m = 1.705 - i 0.054$	46
28	Experimental phase function data for a particle from Run 60 for $\lambda = 488.0$ nm compared with Mie theory for $\alpha = 4.91$ and $m = 1.590 - i0.049$	47
29	Experimental phase function data for a particle from Run 60 for $\lambda = 514.5$ nm compared with Mie theory for $\alpha = 5.38$ and $m = 1.571 - i0.018$	48
30	Experimental phase function data for a particle from Run 1180 for $\lambda = 457.9$ nm compared with Mie theory for $\alpha = 9.61$ and $m = 1.719 - i0.029$	50
31	Experimental phase function data for a particle from Run 1180 for $\lambda = 488.0$ nm compared with Mie theory for $\alpha = 9.20$ and $m = 1.716 - i0.001$	51

LIST OF ILLUSTRATIONS

<u>Figure</u>		<u>Page</u>
32	Experimental phase function data for a particle from Run 1180 for $\lambda = 514.5$ nm compared with Mie theory for $\alpha = 9.30$ and $m = 1.709 - i0.026$	52
33	Computed phase functions based on mean values of α and m for particles from Runs 57 (*), 60 (#) and 60 (+)	53
34	Computed phase functions based on mean values of α and m for particles from Runs 69 (*), 104 (#) and 107 (+) ...	54
35	Computed phase functions based on mean values of α and m for particles from Runs 108 (*), 136 (#) and 138 (+) ..	55
36	Computed phase functions for a Sphere for $\alpha = 10$, $m_1 = 16$ and $m_2 = 0.0$ (*), 0.025 (#) and 0.05 (+)	57
A1	Experimental phase function data for a particle from Run 57 for $\lambda = 457.9$ nm compared with Mie theory for $\alpha = 12.6$ and $m = 1.551 - i0.003$	64
A2	Experimental phase function data for a particle from Run 57 for $\lambda = 488.0$ nm compared with Mie theory for $\alpha = 12.8$ and $m = 1.525 - i0.004$	65
A3	Experimental phase function data for a particle from Run 57 for $\lambda = 514.5$ nm compared with Mie theory for $\alpha = 12.9$ and $m = 1.508 - i0.005$	66
A4	Experimental phase function data for a particle from Run 57 for $\lambda = 457.9$ nm	67
A5	Experimental phase function data for a particle from Run 57 for $\lambda = 488.0$ nm	68
A6	Experimental phase function data for a particle from Run 57 for $\lambda = 514.5$ nm	69
A7	Experimental phase function data for a particle from Run 60 for $\lambda = 457.9$ nm compared with Mie theory for $\alpha = 4.60$ and $m = 1.626 - i0.036$	70
A8	Experimental phase function data for a particle from Run 60 for $\lambda = 488.0$ nm compared with Mie theory for $\alpha = 4.84$ and $m = 1.600 - i0.030$	71
A9	Experimental phase function data for a particle from Run 60 for $\lambda = 514.5$ nm compared with Mie theory for $\alpha = 4.62$ and $m = 1.633 - i0.026$	72
A10	Experimental phase function data for a particle from Run 69 for $\lambda = 457.9$ nm compared with Mie theory for $\alpha = 12.5$ and $m = 1.562 - i0.003$	73

LIST OF ILLUSTRATIONS

<u>Figure</u>		<u>Page</u>
A11	Experimental phase function data for a particle from Run 69 for $\lambda = 488.0$ nm compared with Mie theory for $\alpha = 11.8$ and $m = 1.557 - i0.005$	74
A12	Experimental phase function data for a particle from Run 69 for $\lambda = 514.5$ nm compared with Mie theory for $\alpha = 11.4$ and $m = 1.490 - i0.012$	75
A13	Experimental phase function data for a particle from Run 69 for $\lambda = 457.9$ nm	76
A14	Experimental phase function data for a particle from Run 69 for $\lambda = 488.0$ nm	77
A15	Experimental phase function data for a particle from Run 69 for $\lambda = 514.5$ nm	78
A16	Experimental phase function data for a particle from Run 104 for $\lambda = 457.9$ nm compared with Mie theory for $\alpha = 12.2$ and $m = 1.601 - i0.024$	79
A17	Experimental phase function data for a particle from Run 104 for $\lambda = 488.0$ nm compared with Mie theory for $\alpha = 12.2$ and $m = 1.593 - i0.007$	80
A18	Experimental phase function data for a particle from Run 104 for $\lambda = 514.5$ nm compared with Mie theory for $\alpha = 12.4$ and $m = 1.573 - i0.008$	81
A19	Experimental phase function data for a particle from Run 107 for $\lambda = 488.0$ nm compared with Mie theory for $\alpha = 12.4$ and $m = 1.574 - i0.007$	82
A20	Experimental phase function data for a particle from Run 107 for $\lambda = 514.5$ nm compared with Mie theory for $\alpha = 12.5$ and $m = 1.559 - i0.005$	83
A21	Experimental phase function data for a particle from Run 108 for $\lambda = 457.9$ nm compared with Mie theory for $\alpha = 12.8$ and $m = 1.529 - i0.005$	84
A22	Experimental phase function data for a particle from Run 108 for $\lambda = 488.0$ nm compared with Mie theory for $\alpha = 12.9$ and $m = 1.510 - i0.005$	85
A23	Experimental phase function data for a particle from Run 108 for $\lambda = 514.5$ nm compared with Mie theory for $\alpha = 13.1$ and $m = 1.481 - i0.007$	86
A24	Experimental phase function data for a particle from Run 136 for $\lambda = 488.0$ nm compared with Mie theory for $\alpha = 12.4$ and $m = 1.582 - i0.002$	87

LIST OF ILLUSTRATIONS

<u>Figure</u>		<u>Page</u>
A25	Experimental phase function data for a particle from Run 136 for $\lambda = 457.9$ nm	88
A26	Experimental phase function data for a particle from Run 136 for $\lambda = 488.0$ nm	89
A27	Experimental phase function data for a particle from Run 136 for $\lambda = 514.5$ nm	90
A28	Experimental phase function data for a particle from Run 136 for $\lambda = 457.9$ nm	91
A29	Experimental phase function data for a particle from Run 136 for $\lambda = 488.0$ nm	92
A30	Experimental phase function data for a particle from Run 136 for $\lambda = 514.5$ nm	93
A31	Experimental phase function data for a particle from Run 138 for $\lambda = 457.9$ nm compared with Mie theory for $\alpha = 14.1$ and $m = 1.723 - i0.007$	94
A32	Experimental phase function data for a particle from Run 138 for $\lambda = 488.0$ nm compared with Mie theory for $\alpha = 14.6$ and $m = 1.674 - i0.010$	95
A33	Experimental phase function data for a particle from Run 138 for $\lambda = 514.5$ nm compared with Mie theory for $\alpha = 15.6$ and $m = 1.613 - i0.0$	96
A34	Experimental phase function data for a particle from Run 138 for $\lambda = 457.9$ nm	97
A35	Experimental phase function data for a particle from Run 138 for $\lambda = 488.0$ nm	98
A36	Experimental phase function data for a particle from Run 138 for $\lambda = 514.5$ nm	99
A37	Experimental phase function data for a particle from Run 138 for $\lambda = 457.9$ nm	100
A38	Experimental phase function data for a particle from Run 138 for $\lambda = 488.0$ nm	101
A39	Experimental phase function data for a particle from Run 138 for $\lambda = 514.5$ nm	102
A40	Experimental phase function data for a particle from Run 147 for $\lambda = 457.9$ nm	103
A41	Experimental phase function data for a particle from Run 147 for $\lambda = 488.0$ nm	104
A42	Experimental phase function data for a particle from Run 147 for $\lambda = 514.5$ nm	105

LIST OF TABLES

<u>Table</u>		<u>Page</u>
1	Identification of Samples Studied	25
2	Elemental Analysis of Various Samples	44
3	Results for dust particles for three wavelengths	58
4	Refractive indices of minerals	61

SECTION 1

OBJECTIVES

The research objectives were to measure the light-scattering properties of dust particles generated thermally in solar furnace experiments performed by Science Applications Inc., and to determine the effects of particle size and shape and soil sample on the optical properties. The properties determined are:

1. Phase function (intensity vs scattering angle) for dust particles in the wavelength range $3500 \text{ \AA} - 7000 \text{ \AA}$.
2. Complex refractive index.
3. Particle albedo (or absorption and extinction) for various wavelengths.

1.1 BACKGROUND

1.1.1 Light Scattering Theory

The optical properties of the blow-off particulates were determined from light scattering data using Mie theory to interpret the data. From Mie theory the intensity of the scattered light is established as a function of sphere radius, a , wavelength, λ , complex refractive index, $m = m_1 - im_2$, and scattering angle, θ . The dimensionless size of the sphere, α , is defined by $\alpha = 2\pi a/\lambda$. If α and m are known, the scattered intensity, I_s , as a function of angle θ for light polarized with the electric vector normal to the plane of scattering (the TM mode) are calculated from the equation,

$$I_s = \left| \sum_{n=1}^{\infty} \frac{2n+1}{n(n+1)} [a_n \pi_n(\cos \theta) + b_n \tau_n(\cos \theta)] \right|^2, \quad (1)$$

where $\pi_n(\cos \theta) = P_n^{(1)}(\cos \theta)/\sin \theta$ (2)

$$\tau_n(\cos \theta) = \frac{d}{d\theta} P_n^{(1)}(\cos \theta) \quad (3)$$

$$a_n = \frac{D_n(\beta) - m D_n(\alpha) j_n(\alpha)}{D_n(\beta) - m G_n(\alpha) h_n(\alpha)} \quad (4)$$

$$b_n = \frac{m D_n(\beta) - D_n(\alpha) j_n(\alpha)}{m D_n(\beta) - G_n(\alpha) h_n(\alpha)}, \quad (5)$$

where $h_n(\alpha) = j_n(\alpha) + i N_n(\alpha)$ (6)

$$D_n(z) = (z j_n)' / z j_n \quad (7)$$

$$G_n(z) = (z h_n)' / z h_n \quad (8)$$

In the above equations h_n is the Hankel function, j_n is the spherical Bessel function, N_n is the Neumann function, $P_n^{(1)}$ is the Legendre function, and $\beta = m\alpha$.

Figures 1 and 2 show results of Mie theory calculations as three dimensional plots of the intensity ratio I_s/I_0 (where I_0 is the incident beam intensity)

as functions of the other parameters. Figure 1 demonstrates the effects of particle size and angle on I_s for a real refractive index $m_1 = 1.696$ ($m_2 = 0$ for Fig. 1), and Fig. 2 shows the effects of the imaginary component, m_2 , and angle for $m_1 = 1.550$ and $\alpha = 10$. Figure 1 indicates that as α increases the number and intensity of the peaks in the angle range shown increase. Furthermore, the angular positions of the peaks and troughs depend on α (and m). This is what makes it possible to determine the size and refractive index from light-scattering data on I_s versus θ .

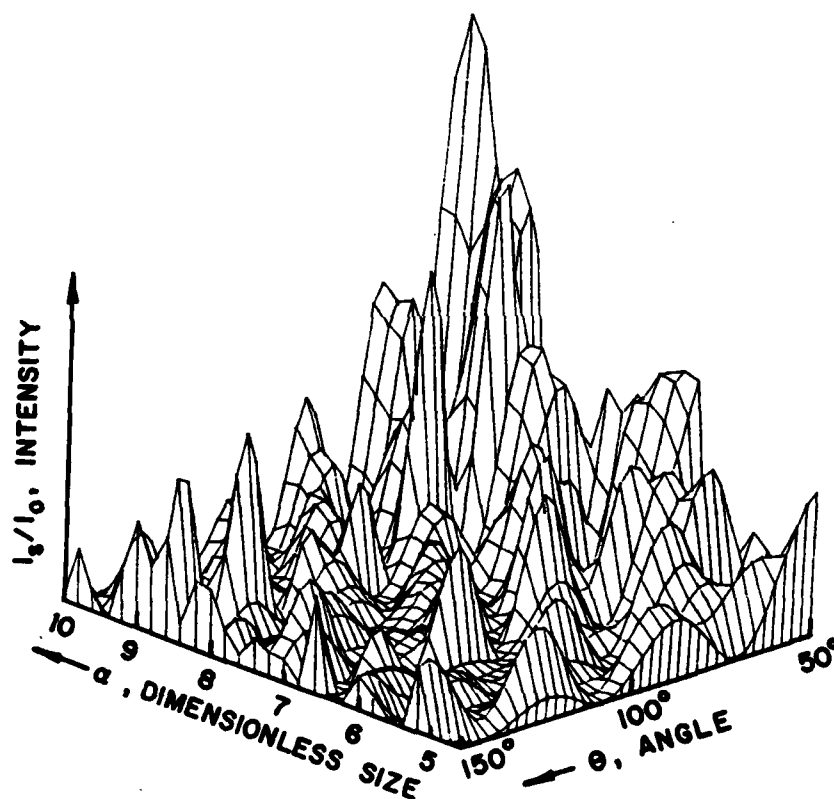


Figure 1. The dependence of scattered intensity I_s , on optical size α and angle θ for a refractive index $m = 1.696 - i0$.

Figure 2 illustrates an important consideration in the evaluation of m_2 . As

m_2 increases from zero (no energy absorption), the intensity profile becomes nearly independent of m_2 , and it becomes difficult to determine m_2 (and, hence, the albedo) for $m_2 > 0.05$ from light-scattering data.

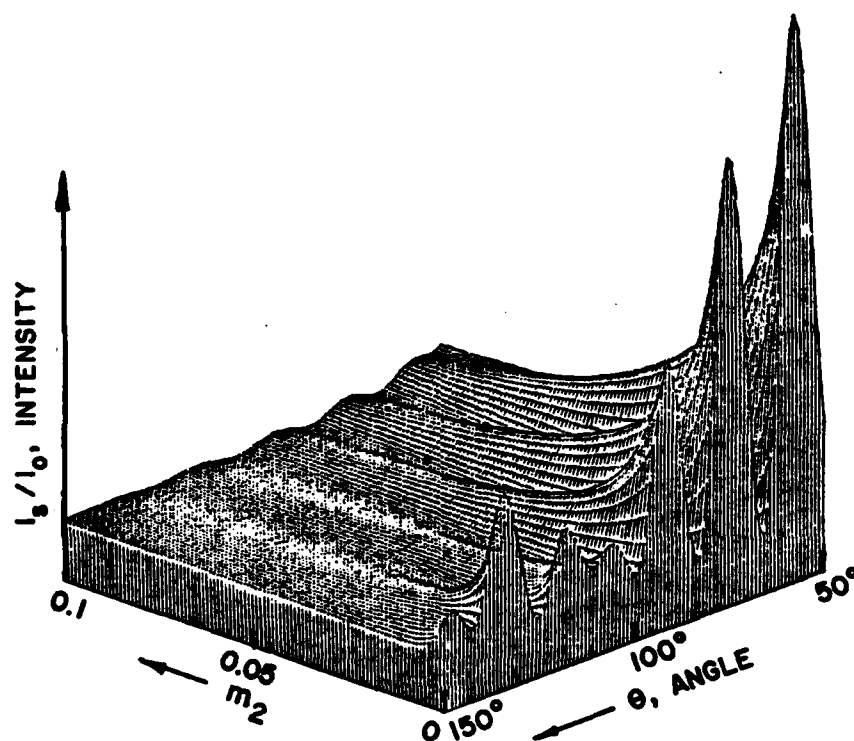


Figure 2. The effects of scattering angle θ and m_2 on the scattering intensity for $m_1 = 1.55$ and $\alpha = 10$.

The complicated topology shown in Figures 1 and 2 must be taken into

account in the analysis and interpretation of the data, for since α and m are initially unknown, the Mie theory equations must be used in an iterative scheme to determine them from the measured scattering function $I_s(\theta)$. The data analysis procedure is outlined below.

1.1.2 Principles of the Electrodynamic Balance

The scattering intensity profile, $I_s(\theta)$, has been measured by suspending a single, charged dust particle in an electrodynamic balance/light-scattering photometer developed by Davis and Ray¹. A cross section of the electrodynamic balance is shown in Figure 3, and an exploded view of the device is shown in Figure 4. The endcap electrodes have geometries described by the equation

$$z^2 - \frac{r^2}{2} = z_0^2 \quad (9)$$

where $2z_0$ is the minimum distance between the endcap and the ring electrode geometry satisfies the equation

$$z^2 - \frac{r^2}{2} = -z_0^2 \quad (10)$$

The ring electrode was connected to an ac power supply (usually a 60 hz transformer) to focus the charged particulate on the centerline (vertical axis) of the balance. With no dc field applied the particle oscillates about a point below the midplane of the balance. When a dc field is applied to offset the gravitational force on the particle it remains stationary at the midplane ($z=0$) between the endcaps.

¹ Davis, E.J. and Ray, A.K., "Single Aerosol Particle Size and Mass Measurements Using an Electrodynamic Balance," J. Colloid and Interface Sci., 75(2), 566-576, 1980.

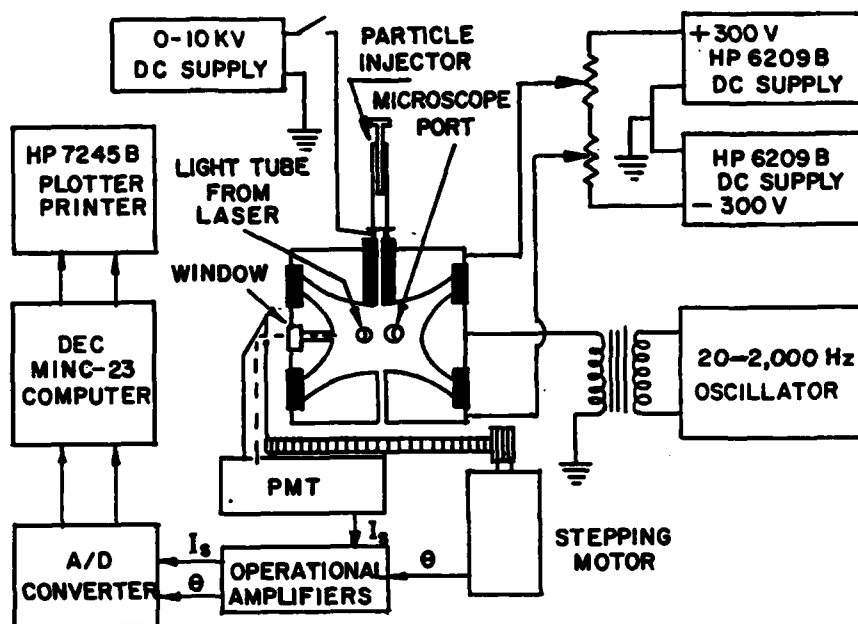


Figure 3. The electrodynamic balance/light scattering photometer and peripheral equipment.

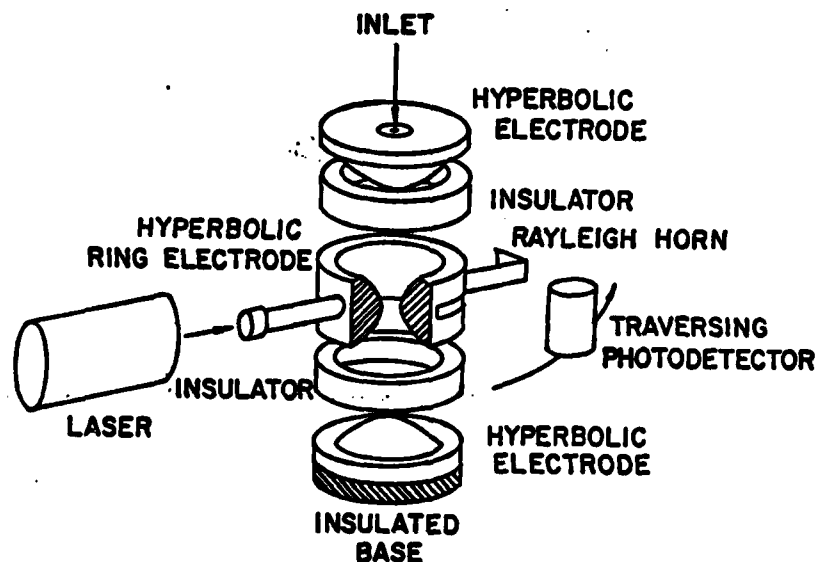


Figure 4. An exploded view of the electrodynamic balance

If, for a negatively charged particle, a dc voltage, $+V_{dc}$ is applied to the upper electrode and $-V_{dc}$ is applied to the lower endcap, the electric field near the null point (midplane) of the balance is given by

$$E_{dc,z} = C \frac{V_{dc}}{z_0}, \quad (11)$$

where C is a geometrical constant which takes into account the shape of the electrodes and the edge effects.

For a particle of mass, m_p , and charge, q , the particle is balanced when the following force balance is satisfied

$$qE_{dc,z} - m_p g = 0, \quad (12)$$

where g is the gravitational acceleration constant. The dc voltage required to balance the particle is given by

$$V_{dc} = \frac{m_p g z_0}{qC} \quad (13)$$

As indicated in Figure 4, a laser beam was aligned to pass through the center of the chamber, and a window and slit in the ring electrode permitted detection of the scattered light by means of a transversing photomultiplier tube. The photodetector was driven by a stepping motor, and the signals from the photodetector (intensity) and the stepping motor (angle) were digitized and recorded using a Digital Equipment Corporation MINC-23 computer. Additional details of the experimental system are provided in the next section.

SECTION 2

THE EXPERIMENTAL APPARATUS AND DATA ANALYSIS

2.1 THE EXPERIMENTAL SYSTEM

The components of the experimental system are indicated in Figure 5. The dc power supplies were matched and connected to a dual potentiometer to permit precise balancing of the charged particulate, observed through a low-power microscope attached to the balance frame. Dust particles were washed from the filters or wall-wiping material to form a dilute suspension in water, and the suspension was drawn into a microliter syringe. The needle of the syringe was connected to a high voltage dc supply to facilitate charging.

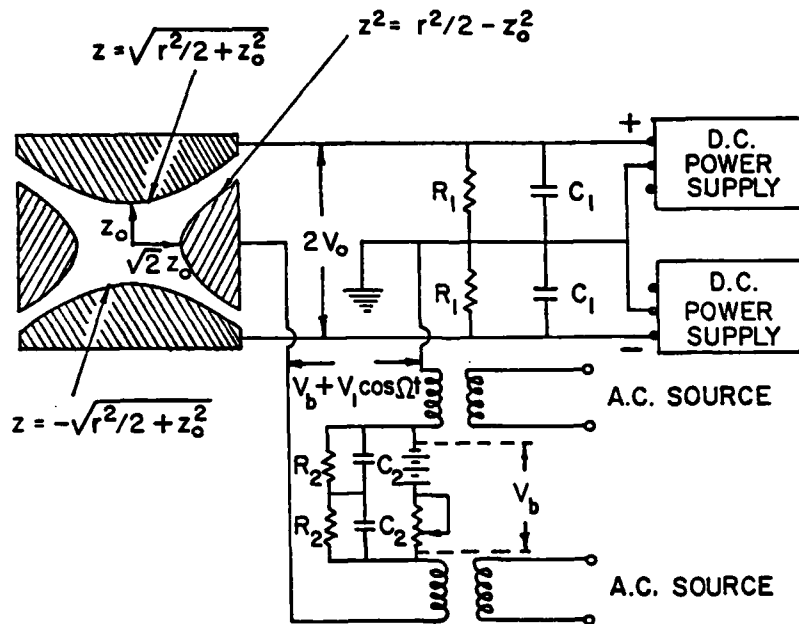


Figure 5. The electrical circuitry for the picobalance.

Injection of a dust particle into the balance was accomplished by forming a

small droplet at the top of the needle, switching on the high voltage, and adjusting the ac voltage to "catch" the droplet. The water surrounding the particulate quickly evaporated, leaving the charge on the particle. The dc voltage was then applied to the endcaps to stabilize the particle at the center of the balance. Usually a dust particle was suspended for more than one hour prior to obtaining a light-scattering data to insure that the water was removed.

After no mass change could be detected, the laser intensity and voltage input to the photomultiplier tube were adjusted to give a favorable signal-to-noise ratio, indicated by recording the scattered intensity as a function of angle on an X-Y recorder. Next the computerized data acquisition was carried out.

The laser light sources provided vertically polarized (TM mode) light at any of several discrete wavelengths. Two sources were available: (i) a 10 mW Spectra Physics helium-neon laser (632.8 nm) and (ii) a Coherent Innova 90-5 5W argon-ion laser. A tunable dye laser was available, but was not used for the results reported here because the argon-ion laser had a sufficient range of wavelengths in the visible. The wavelengths used were 457.9, 488.0 and 514.5 nm.

For data acquisition the signals from the photomultiplier tube and the stepping motor were conditioned to be in the voltage range 0-5 V by means of operational amplifiers, and these signals were digitized and recorded using a DEC MINC-23 computer system. The computer data acquisition was activated by triggering the computer clock with a signal from the stepping motor, and the sampling rate was selected to obtain about 500 data points during a forward scan (from about 6° to 174°) and the same number during a reverse scan. Data-taking stopped after the completion of one forward-reverse scan cycle.

Figure 6 shows typical raw data for a forward scan, plotted on the HP 7245 B Printer/Plotter as intensity (PMT output voltage) versus angle

(Stepping motor voltage). Two sharp troughs should be noted at about 1.35 volts and 3.78 volts. These minima in the scattered intensity were caused by the blockage of the light by two pegs installed to provide calibration of the voltage signal from the stepping motor. The raw data (PMT output voltage versus stepping motor voltage) were examined, using appropriate computer software, to determine the voltages at which the sharp troughs occurred. These stepping motor voltages, then, corresponded to the angles 16.2° and 163.8° .

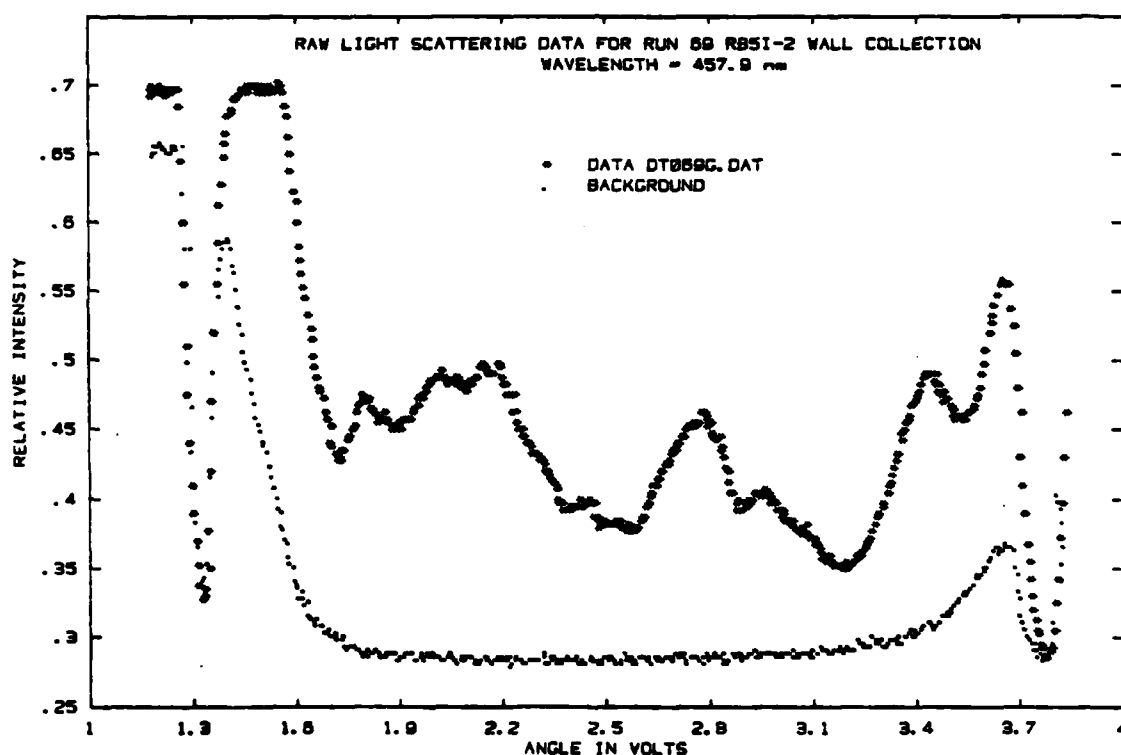


Figure 6. Raw light scattering data from a dust particle, $\lambda = 457.9 \text{ nm}$

After a scan cycle was completed the wavelength of the laser was changed, and the experiment repeated. At the end of a sequence of experiments on a particular dust particle the particle was expelled from the balance, and the

background signal was measured and recorded at each wavelength. Figure 6 shows both the data obtained with a dust particle suspended in the beam and the background. The data used in further analysis was the difference between the two signals.

2.2 INTERPRETATION OF THE DATA

To determine the particle size and refractive index from data of the type shown in Figure 5 Mie theory was applied. Forty data points uniformly spaced on the angle axis were selected, usually in the range $30^\circ - 130^\circ$, and the intensities, I_t predicted from Mie theory for these angles were calculated. The voltages from the photodetector circuit were converted to normalized intensities using the relation

$$I_e(\theta_i) = \sigma[V(\theta_i) - V_b(\theta_i)], \quad (14)$$

where σ is a scale factor, $V(\theta_i)$ is the signal at the i^{th} angular position, $V_b(\theta_i)$ is the background signal (no particle present) at that position and $I_e(\theta_i)$ is the experimental intensity at θ_i . The scale factor, σ , can be determined in a number of different ways. One method is to use the maximum (highest peak in the light scattering profile) and minimum (lowest trough in the profile) detector signals to normalize $I_e(\theta_i)$, that is, define σ by

$$\sigma = \frac{1}{(V_{\max} - V_{\min})} \quad (15)$$

This method places too much emphasis on only two points of the light scattering profile, for if there is excessive noise in the signal, significant

error is introduced in the normalization. A better approach is to consider σ a parameter in the optimization procedure used to compare the experimental intensities with those computed from Mie theory.

To interpret the experimental data we determined values of α , m ($m = m_1 - im_2$) and σ that minimize the function

$$F(\alpha, m, \sigma) = \sum_{i=1}^N w_i \left| f_i \right|^2, \quad (16)$$

where f_i is the i^{th} residual defined by

$$f_i = I_e(\theta_i) - I_t(\theta_i), \quad (17)$$

and w_i is the weighting factor. For these studies N was usually 40, and the most suitable weighting factor was found to be $w_i = \sin^2 \theta_i$.

To minimize the objective function, $F(\alpha, m, \sigma)$ we applied the Levenberg-Marquardt algorithm (Marquardt²), which performs an optimum interpolation between the Taylor series and gradient (steepest descent) methods. The Gauss-Newton method of optimization depends upon reduction of the residual, f_i , to linear form by first order Taylor approximations taken about an initial or trial solution for the parameters. This method frequently fails because of divergence of successive iterations, so various modifications of the method of steepest descent have been introduced to avoid such divergence, but the method of steepest descent can give agonizingly slow convergence after the first few

² Marquardt, D.W., "An Algorithm for Least-Squares Estimation of Nonlinear Parameters," J. of the Society of Industrial Applied Mathematics, 11(2), 431-441, 1963.

iterations. The Levenberg-Marquardt algorithm avoids the worst features of the older methods.

After the optimal values of the parameters were obtained, the theoretical intensities computed were graphed together with the experimental data, and the results are displayed in the next section.

SECTION 3

RESULTS

3.1 SAMPLE IDENTIFICATION

To identify the dust samples in this report we shall use the run numbers used by Science Applications, Inc. [Trip Reports, March 1980 and September 1980, DNA Soil Test Program at the CNRS 1000 KW Solar Furnace, Odeillo, France, November 24, 1980]. Table 1 lists the run numbers, soil type codes and description for each of the samples studied herein.

The samples described above as wall wipings were particulates washed from towelling used to remove dust from the furnace walls. Very little dust was found in filter samples, and it was difficult to wash dust out of the filter matrix.

3.2 ELECTRON MICROSCOPY

A scanning electron microscope equipped for elemental analysis by energy dispersion x-ray spectrometry (EDAX) was used to examine the sizes, shapes and elemental analyses of dust particles in the samples. Figures 7 and 8 are scanning electron micrographs (SEM) of loose thermal dust collected from the solar furnace and wall wipings, respectively, for Run 57, and they illustrate the range of sizes (note the 100 μm bars at the bottom of each picture) and the shapes encountered. Approximately half of the particulates shown in these figures are spherical or near-spherical, indicating that the temperatures reached were sufficient to melt many of the chemical species present.

Table 1. Identification of samples studied

<u>SAI Run No.</u>	<u>Soil Type Code</u>	<u>Description</u>
57	Silt P-14	Wall wipings and Bottom filter
60	Clay P-13	Wall wipings
69	RB5I-2	Wall wipings and Bottom filter
101		Wall wipings
104	RC5Y-2	Wall wipings
107	RC4U-2	Wall wipings
108	RD5I-2	Wall wipings
136	Soil RBU2#15	Wall wipings
138	Gray tile	Wall wipings
147	Local vegetation	Wall wipings and Bottom filter
1180	5F	Wall wipings

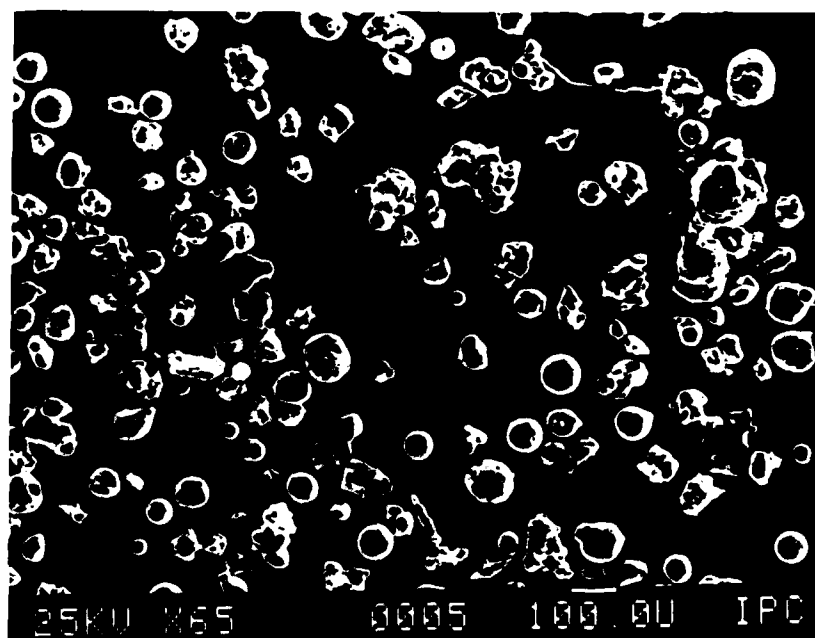


Figure 7. An SEM of loose dust from Run 57

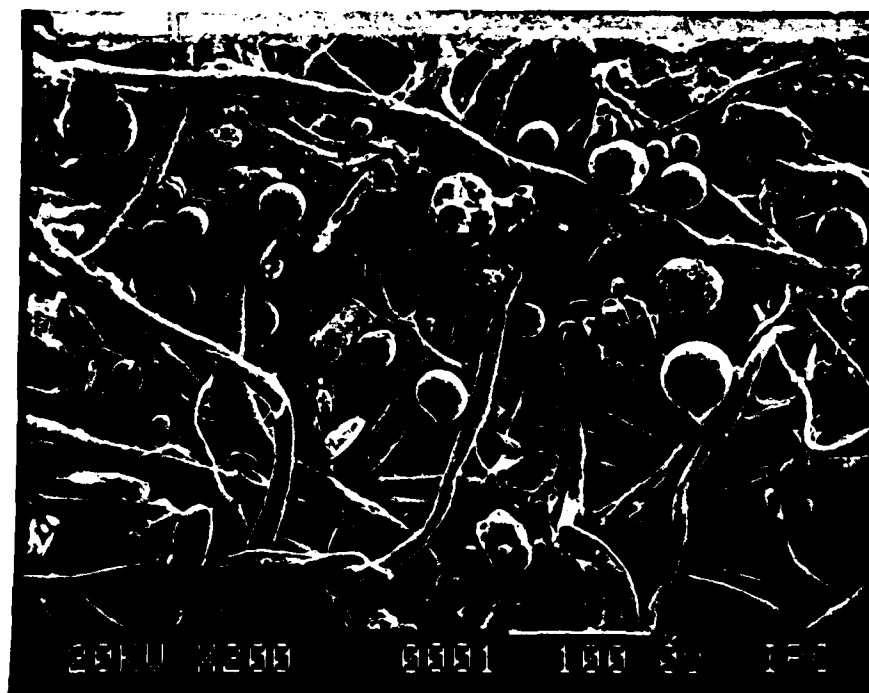


Figure 8. An SEM of wall wipings from Run 57.

Figures 9 and 10, on the otherhand, show many particles of irregular shape and relatively large size (dimensions $> 100 \mu\text{m}$) for loose material from Runs 69 and 1180, respectively. Such large particles would be expected to have fairly rapid settling rates and were not found in the filters. It is clear from Figure 7-10 that the range of particle sizes is very great, and Figure 11-13 for Run 136 show that wide ranges of sizes and shapes are encountered in a single run. The three figures were obtained by increasing the magnification from X200 to X2400. At a magnification of X200 many agglomerated particulates can be seen (Figure 11), and at the higher magnifications a very large number of irregularly shaped particles are seen.

A set of SEM and the corresponding EDAX analyses are shown in Figure 14 through 26 for the runs listed in Table 1. Several of the EDAX analyses show large peaks corresponding to gold (Au) and palladium (Pd), for these elements were used to shade the particulates for some of the SEM. The SEM selected are for various magnifications; some show relatively large regions of a sample, and others focus on specific particulates. Table 2 summarizes the main elements detected in the samples.

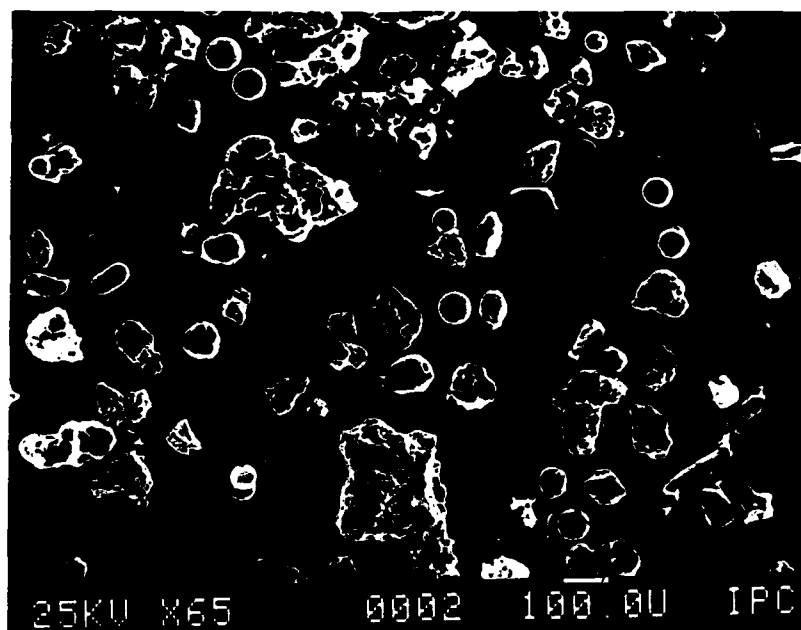


Figure 9. An SEM of loose dust from Run 69.

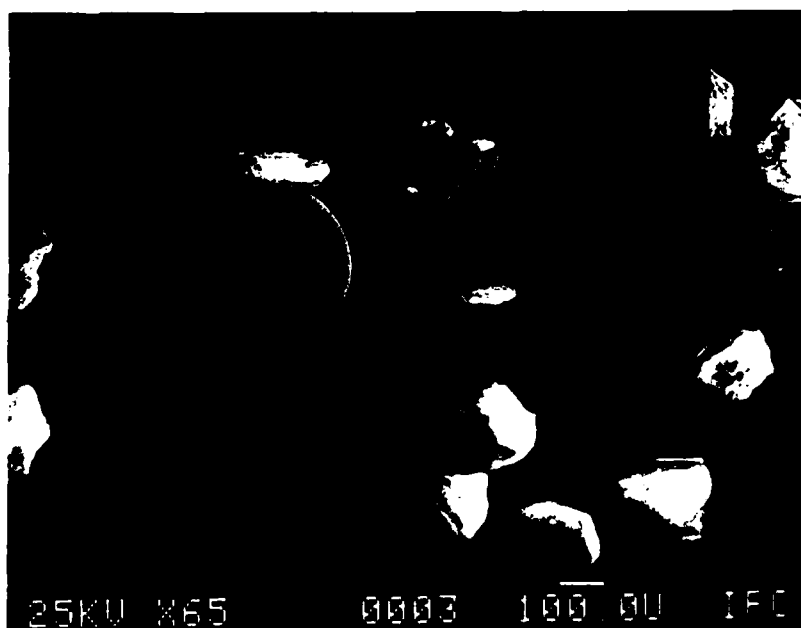


Figure 10. An SEM of loose dust from Run 1180.

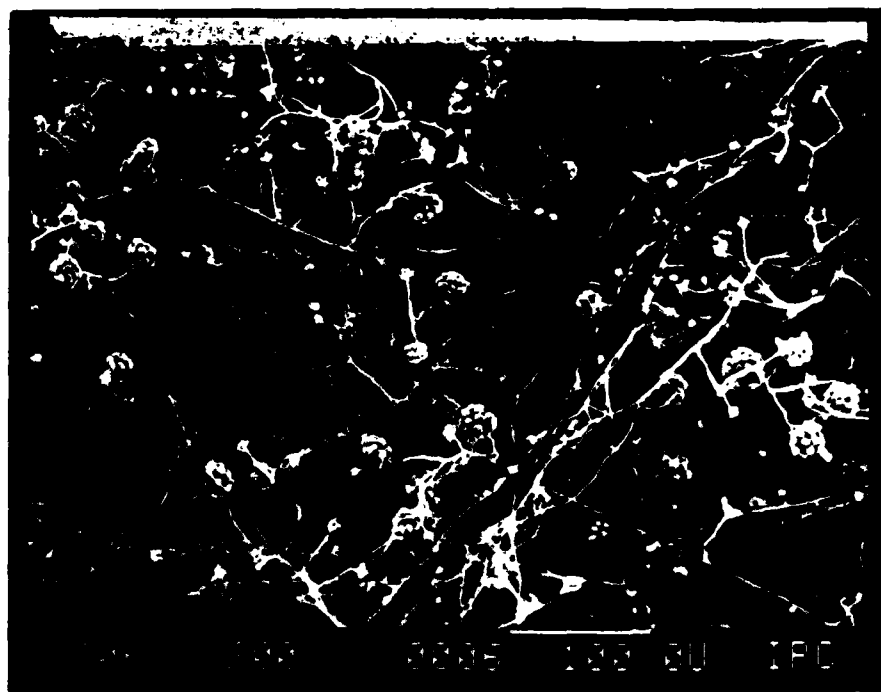


Figure 11. An SEM of wall wipings from Run 136 at lower magnification (X200).

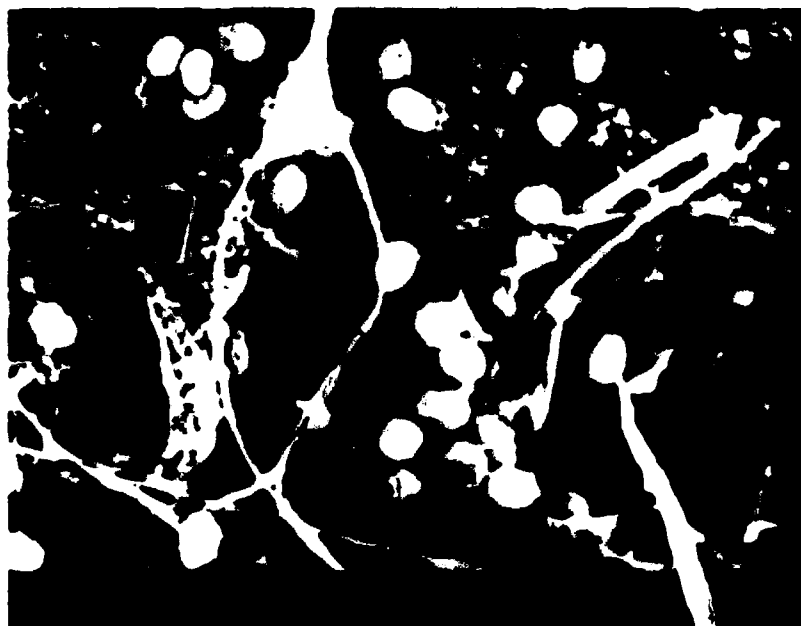


Figure 12. An SEM of wall wipings from Run 136 for a magnification X1000

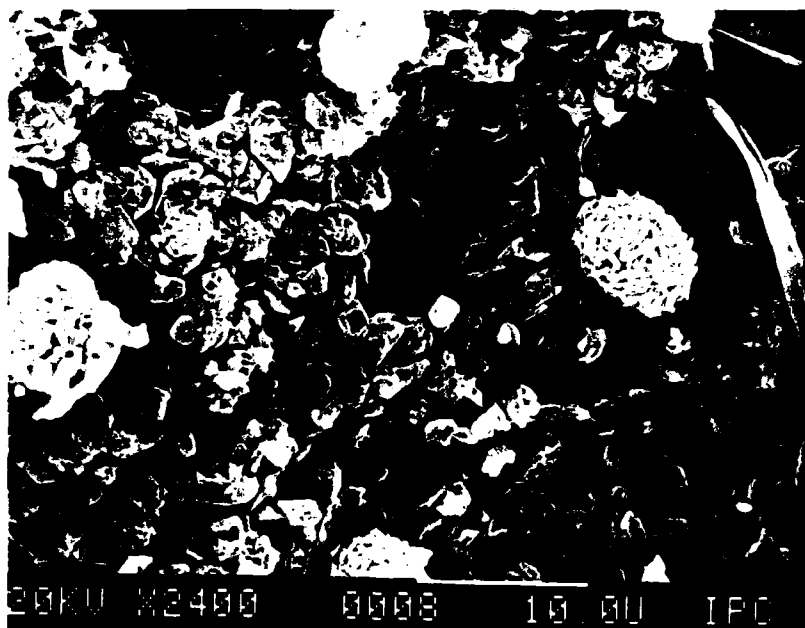


Figure 13. An SEM of wall wipings from Run 136 at high magnification (X2400).

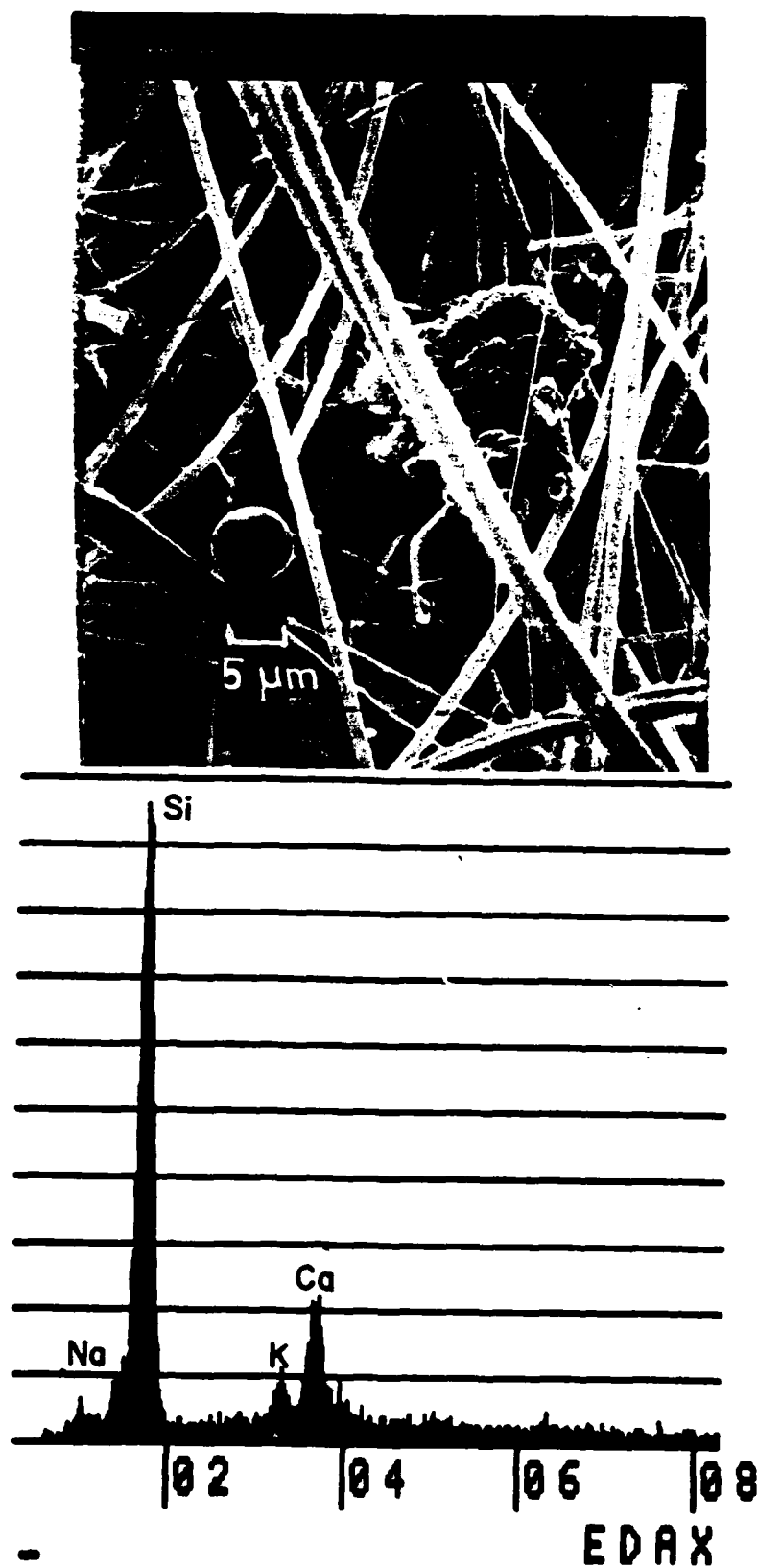


Figure 14 a,b. An SEM and elemental analysis (EDAX) for a bottom filter from Run 57.

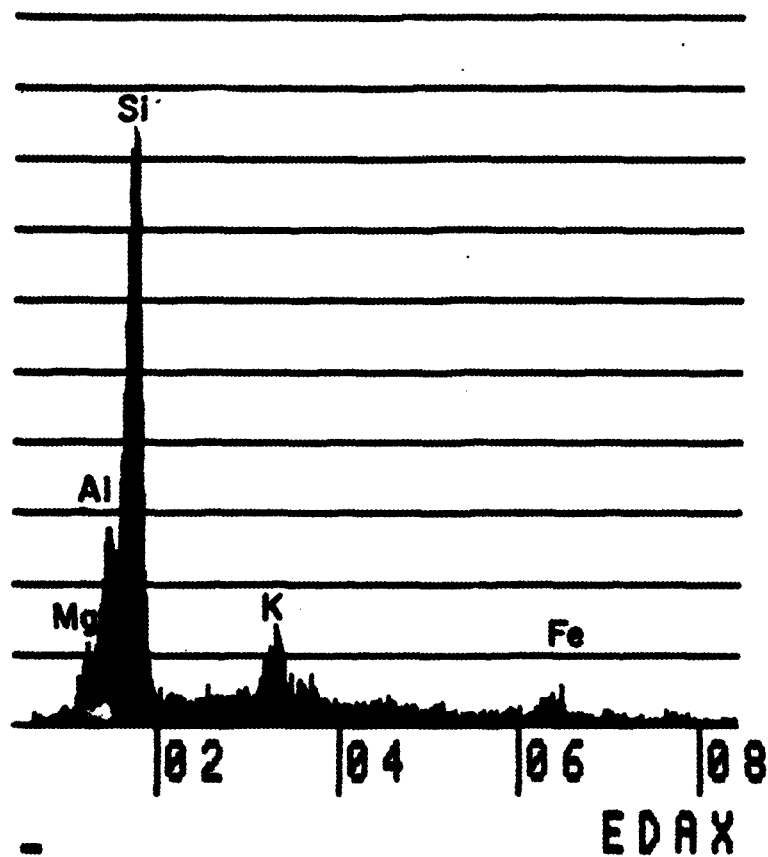
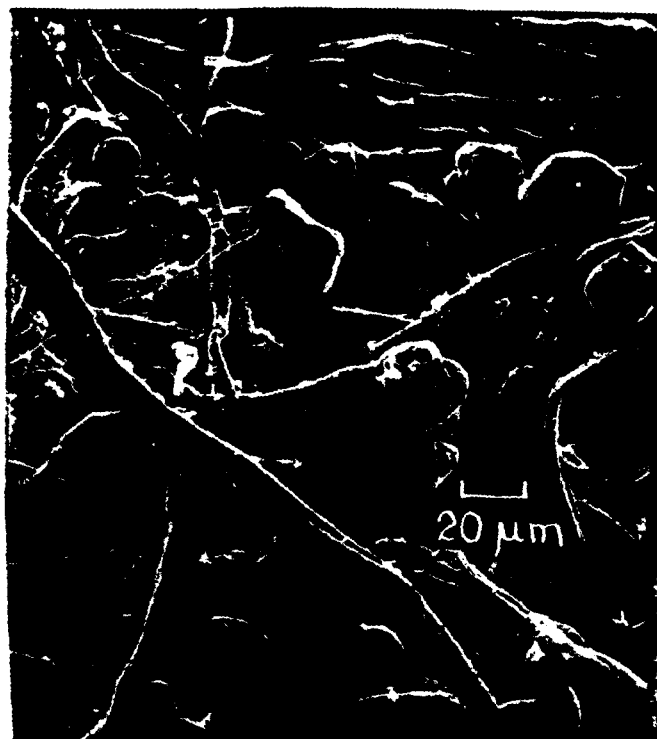


Figure 15 a,b. An SEM elemental analysis for a wall wiping from Run 57.

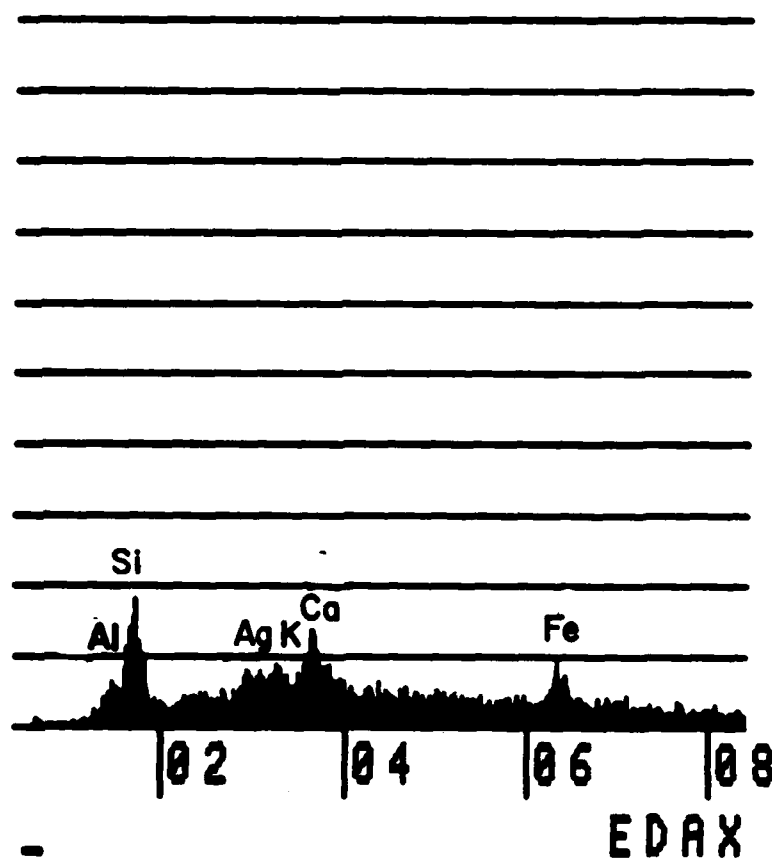


Figure 16 a,b. An SEM and elemental analysis for a wall wiping from Run 60.

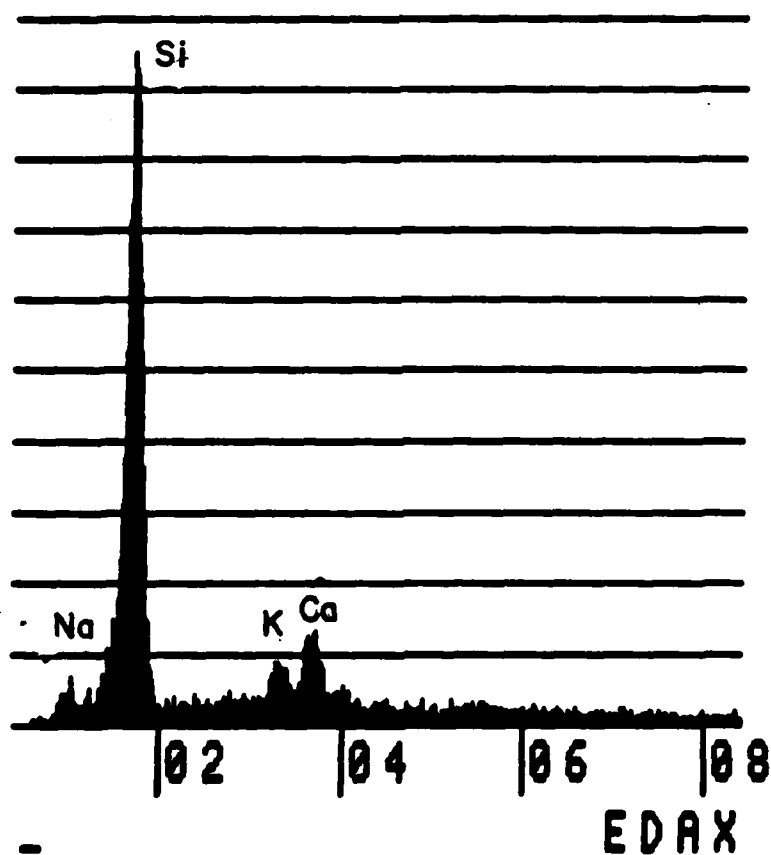
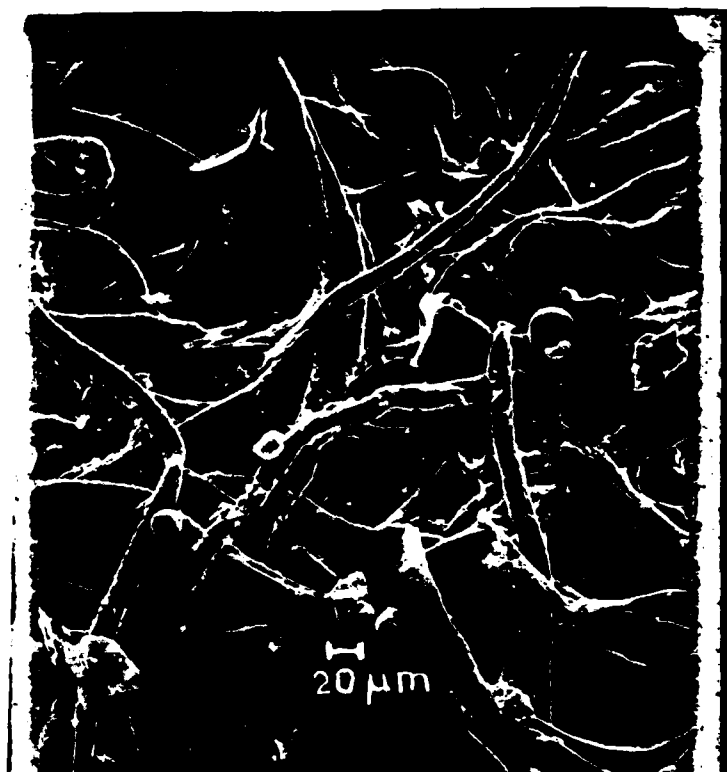


Figure 17 a,b. An SEM and elemental analysis for a wall wiping from Run 69.

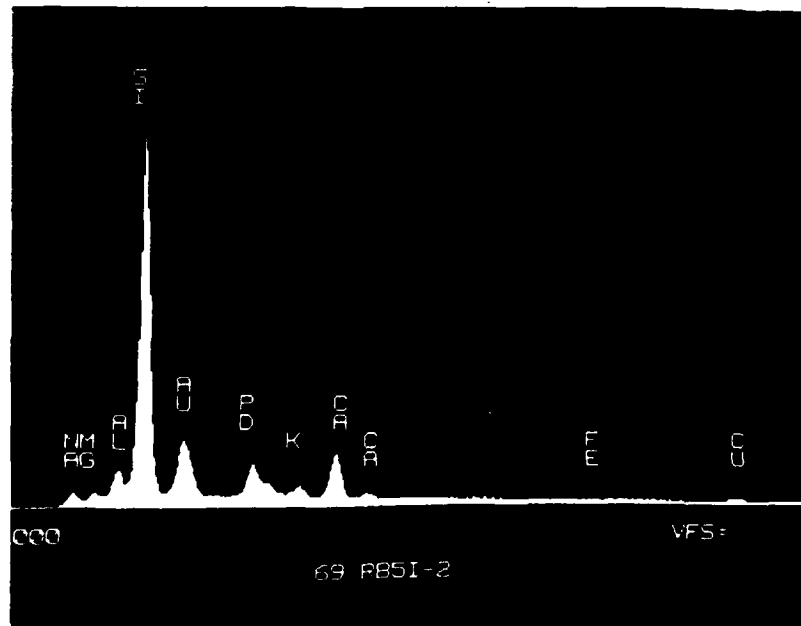
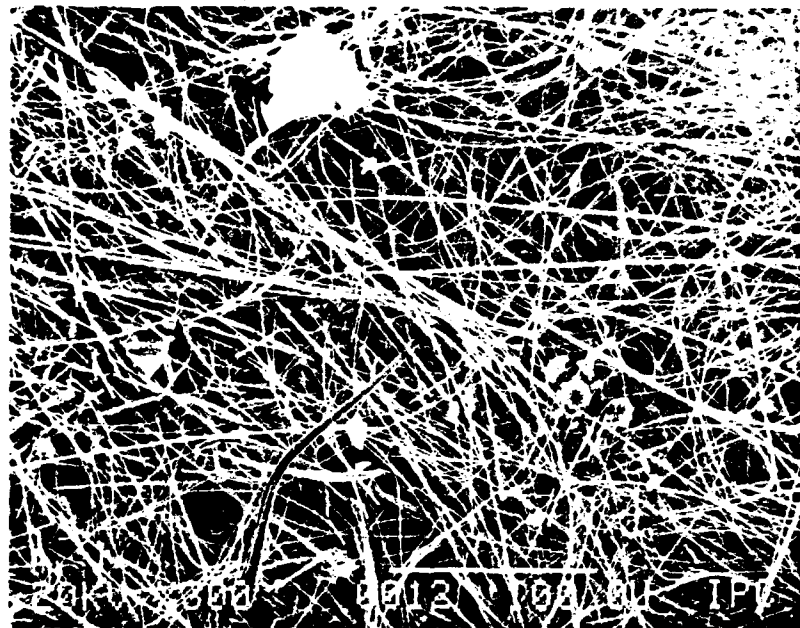


Figure 18. An SEM elemental analysis for a bottom filter from Run 69.

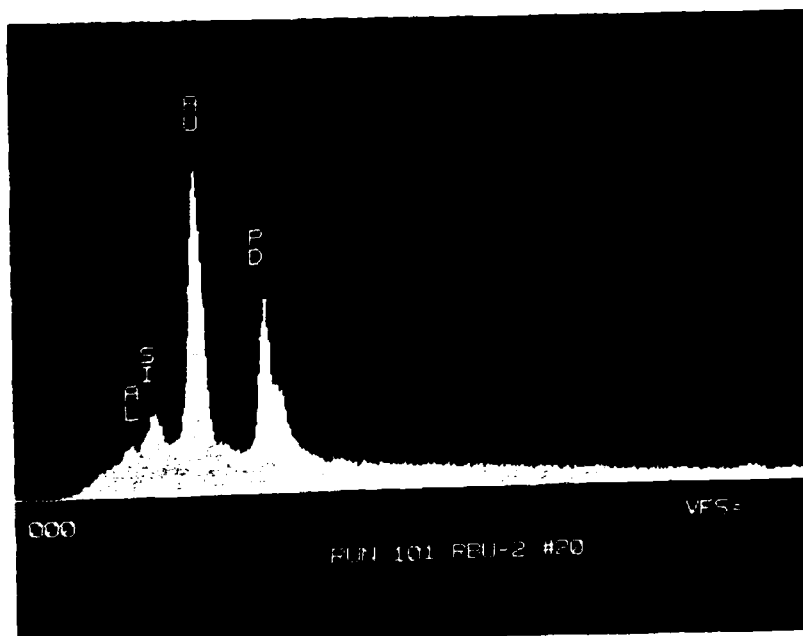


Figure 19 a,b. An SEM and elemental analysis for a wall wiping from Run 101.

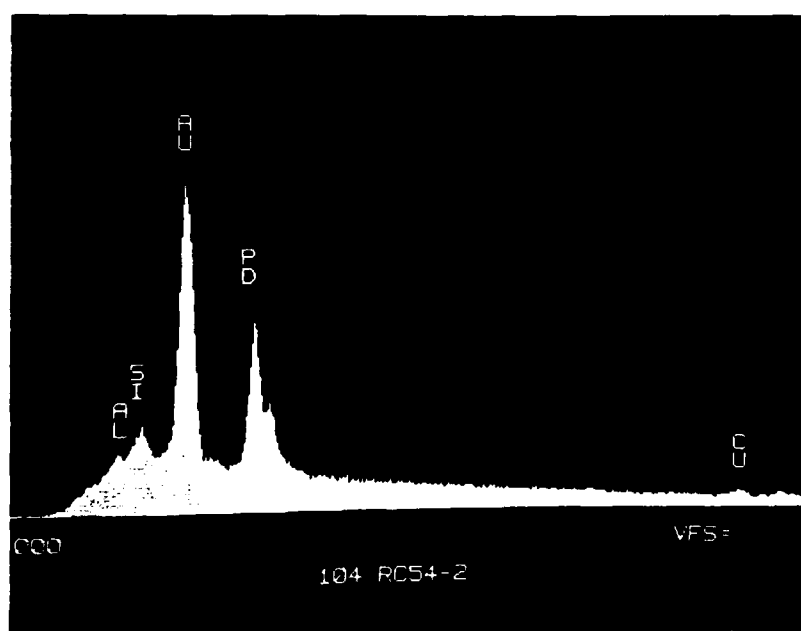


Figure 20 a,b. An SEM and elemental analysis for a wall wiping from Run 104.

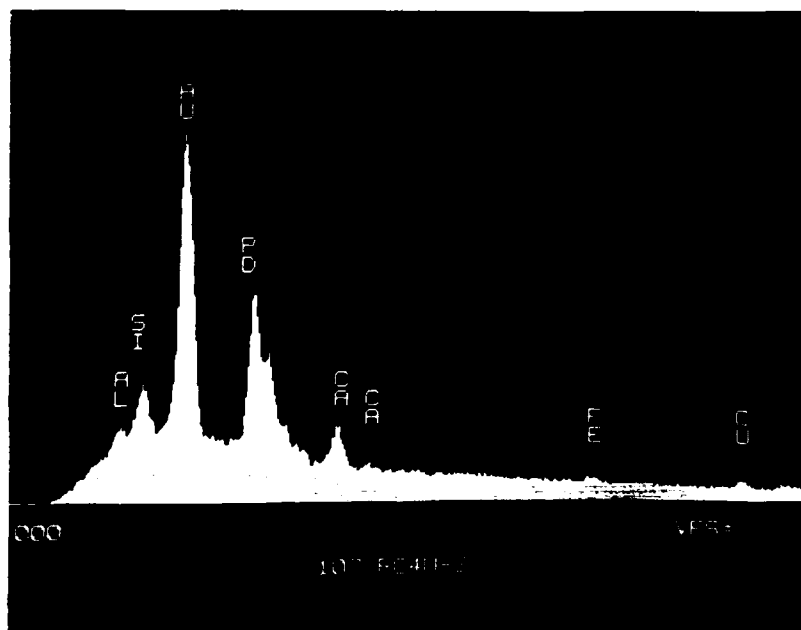
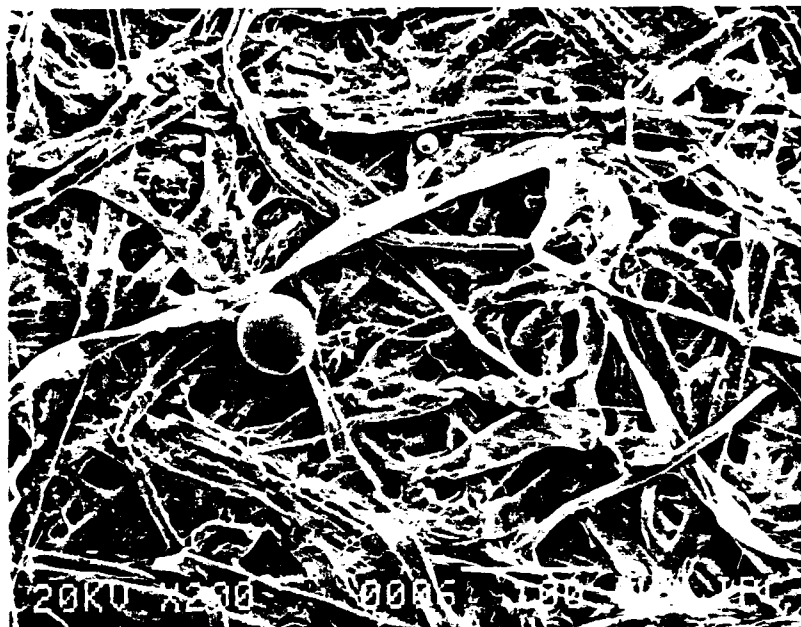


Figure 21 a,b. An SEM and elemental analysis for a wall wiping from Run 107.

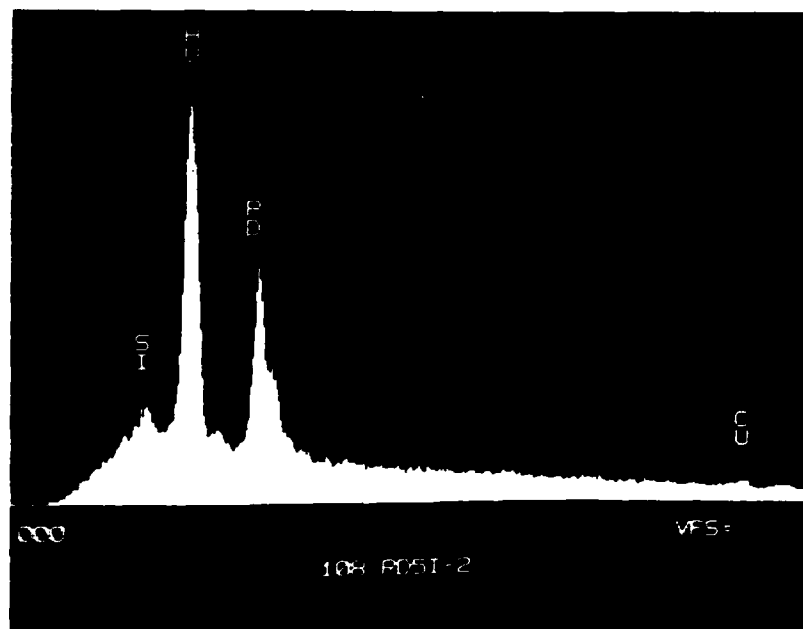


Figure 22 a,b. An SEM and elemental analysis for a wall wiping from Run 108.

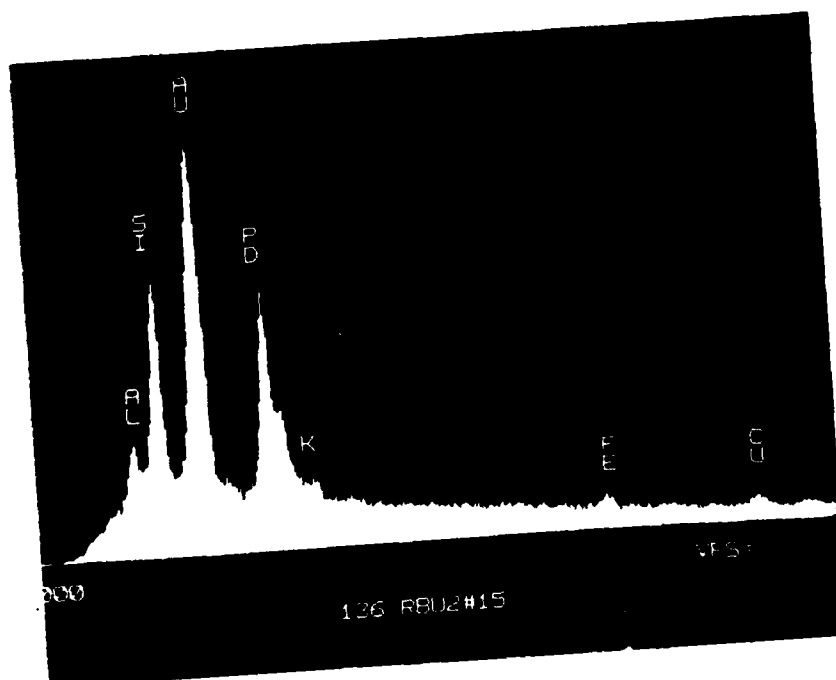


Figure 23 a,b. An SEM and elemental analysis for a wall wiping from Run 136.

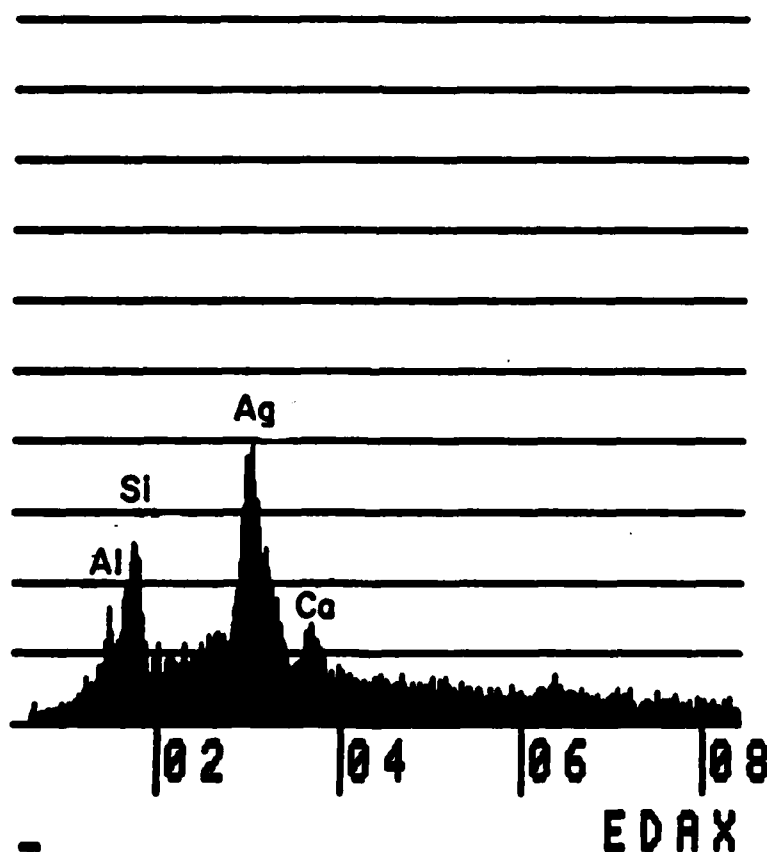
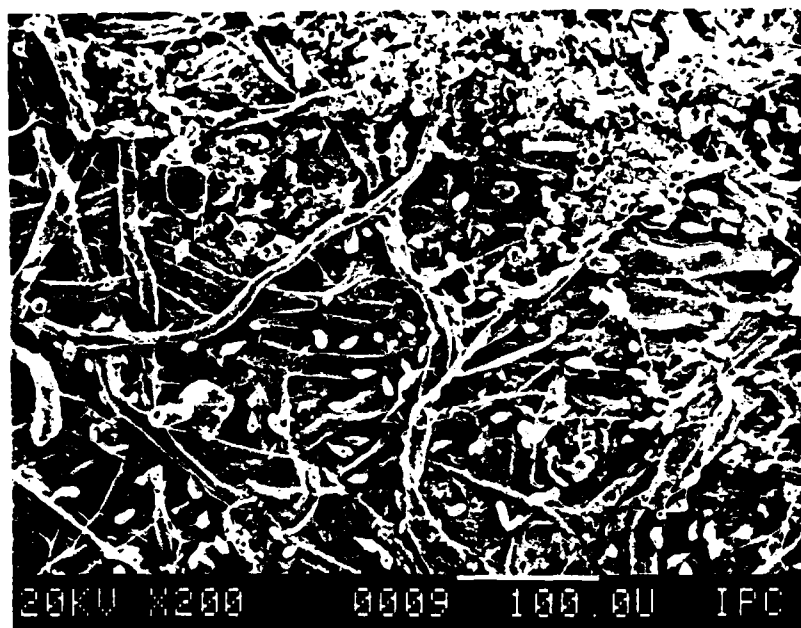


Figure 24 a,b. An SEM and elemental analysis for a wall wiping from Run 138.

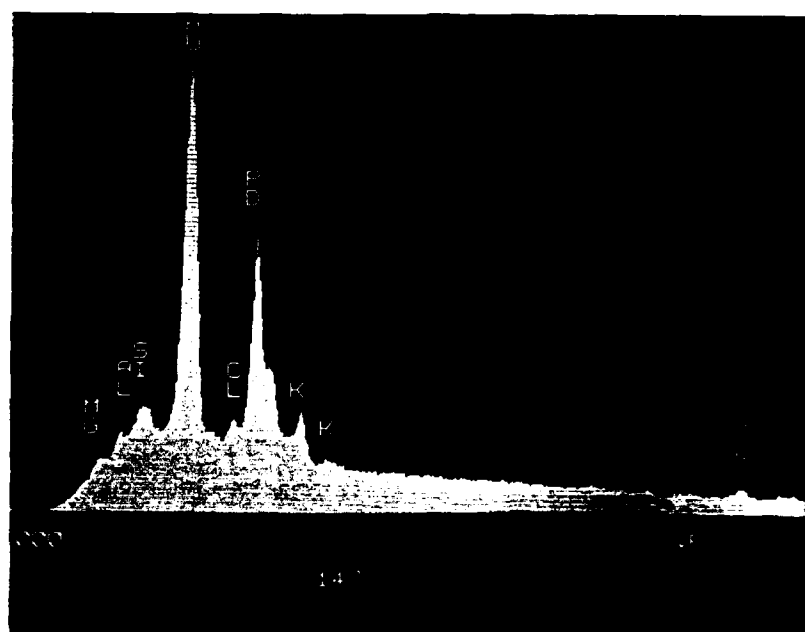


Figure 25 a,b. An SEM and elemental analysis for a wall wiping from Run 147.

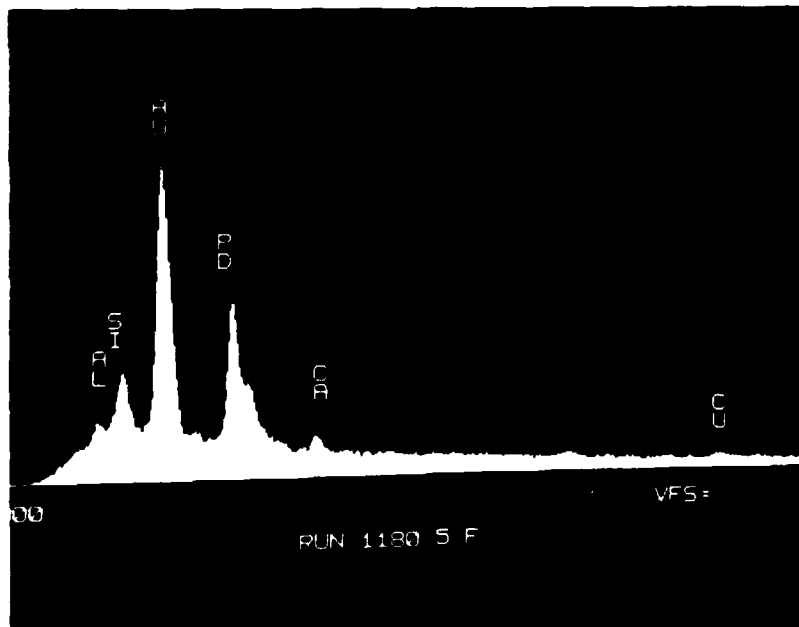
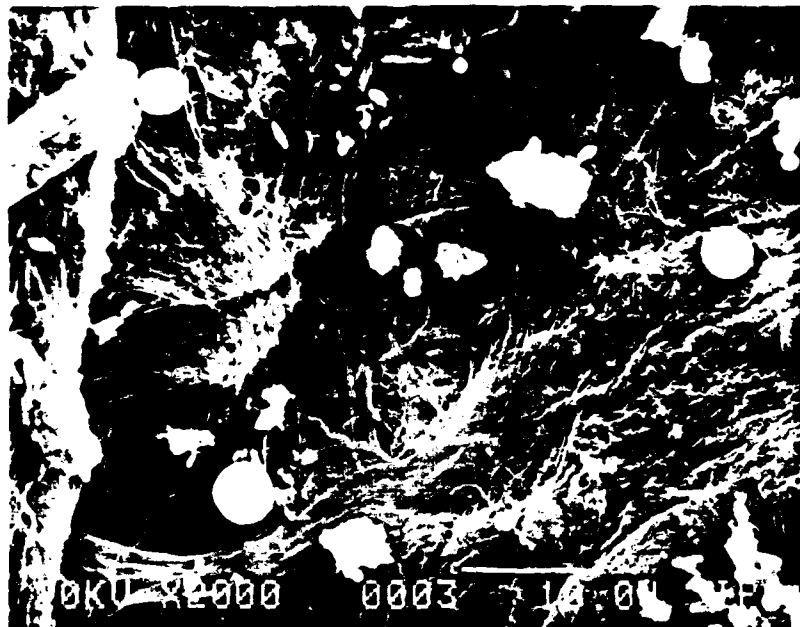


Figure 26 a,b. An SEM and elemental analysis for a wall wiping from Run 1180.

Table 2. Elemental analysis of various samples

<u>Run No.</u>	<u>Main Elements</u>	<u>Trace Elements</u>
57	Al,Ca,K,Na,Si	Fe
60	Al,Ca,Fe,K,Si	Ag
69	Al,Ca,K,Na,Si	Ag,Fe,Cu
101	Al,Si	
104	Al,Si	Cu
107	Al,Ca,Si	Cu,Fe
108	Si	Cu
136	Al,Ca,Fe,K	Cu
138	Ag,Al,Ca,Si	Fe
147	Al,Cl,K,Mg,Si	Cu
1180	Al,Ca,Si	Cu

Most of the samples consisted of mixed silicates of aluminum, calcium and potassium, and samples from Runs 57 and 69 contained sodium compounds. Iron was found in significant amounts in samples from Runs 60 and 136, and iron and copper were present in trace amounts in most samples. The iron and copper might have been in the form of oxides, but quantitative analysis and information on the chemical species encountered were not possible with the techniques used.

Samples from Run 147 were found to be different from the others in that magnesium and chlorine were detected in these samples which came from local vegetation. Run 136 has some unique features, for Figure 11-13 show agglomerated particles and particles that might be of biological origin (e.g., spores).

Because spherical particulates are not seen (see Figure 13 and 23a) it appears that the temperatures encountered in Run 136 were too low to melt silicates.

3.3 LIGHT SCATTERING PHASE FUNCTIONS

Figure 27-32 are representative plots of scattered intensity versus angle for various samples at various wavelengths, and a complete set of raw data are given in Appendix A. The figures shown in this section correspond to data for which the optimization program converged to yield values of size $\alpha = \pi D_p / \lambda$ and refractive index $m = m_1 - im_2$. For many experiments no satisfactory match between the measured phase functions and Mie theory was achieved, so for experiments only raw data are given in the appendix.

For many runs only the angle range from about 20° to 100° was examined, but with the redesign of the viewing window more recent data cover the range from about 20° to 160°. The pegs used to calibrate the stepping motor voltage prevented the collection of data beyond this range.

Figures 27-29 show a set of data for a thermal dust particle from Run 60 obtained at three different wavelengths. The agreement between experimental and calculated phase functions is fairly good here, considering that the data are "noisy", but there is a rather larger scatter in the values of particle diameter, D_p , calculated from the values of α obtained from the data analysis. The calculated particle diameters are 0.730 μm , 0.763 μm and 0.881 μm with a mean of 0.791 μm . The scatter about the mean is about $\pm 10\%$. There is also scatter in the values of m_1 , and m_2 from the data, but the refractive index can be expected to vary with wavelength, and more will be said on that point below.

A second set of three runs, which cover a different range of angles, is presented as Figures 30-32 for Run 1180. Note that there is backscatter shown in

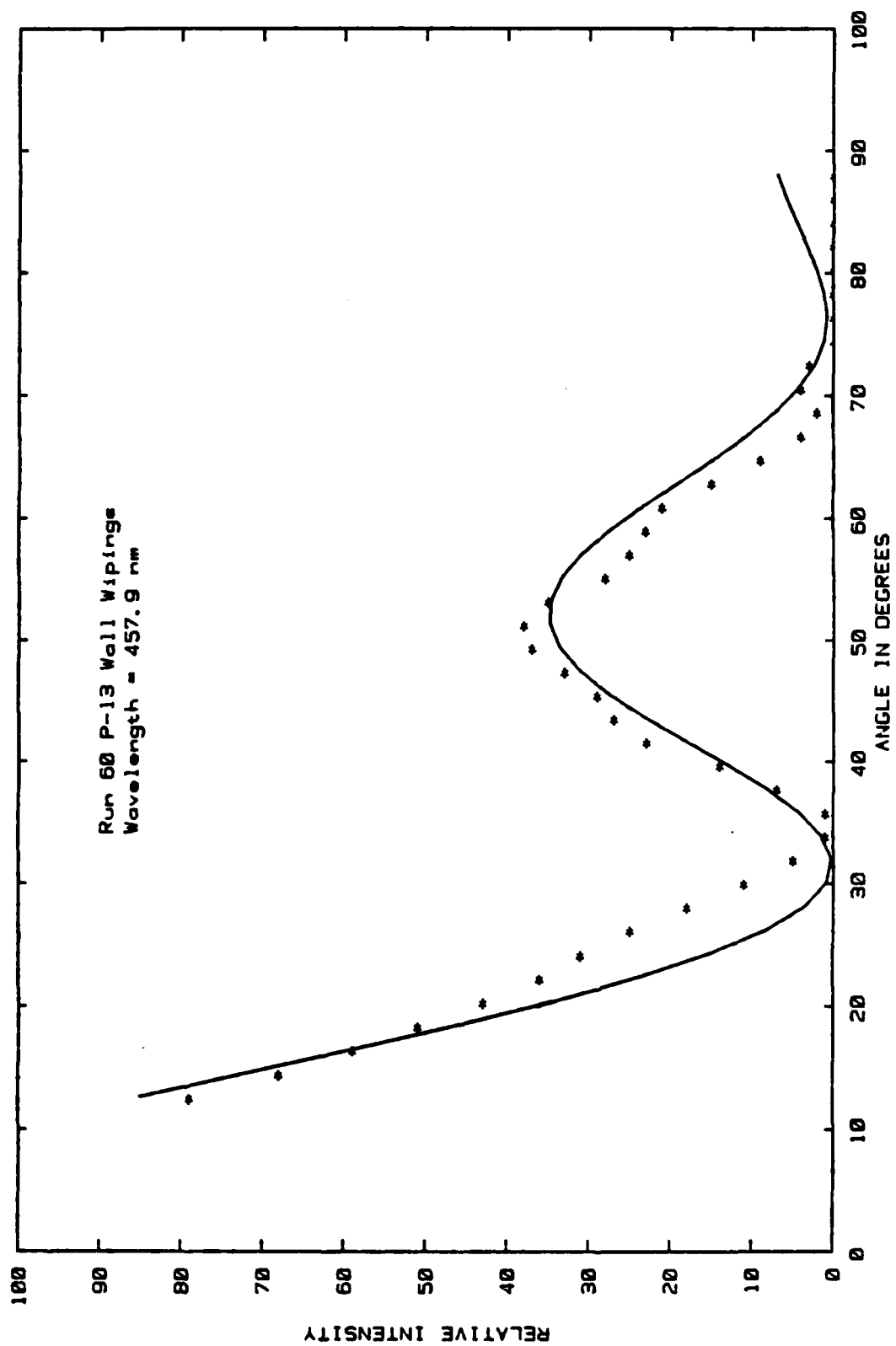


Figure 27. Experimental phase function data (*) for a particle from Run 60 for $\lambda = 457.9$ nm compared with Mie theory (—) for $\alpha = 5.01$ and $m = 1.705 - i0.054$.

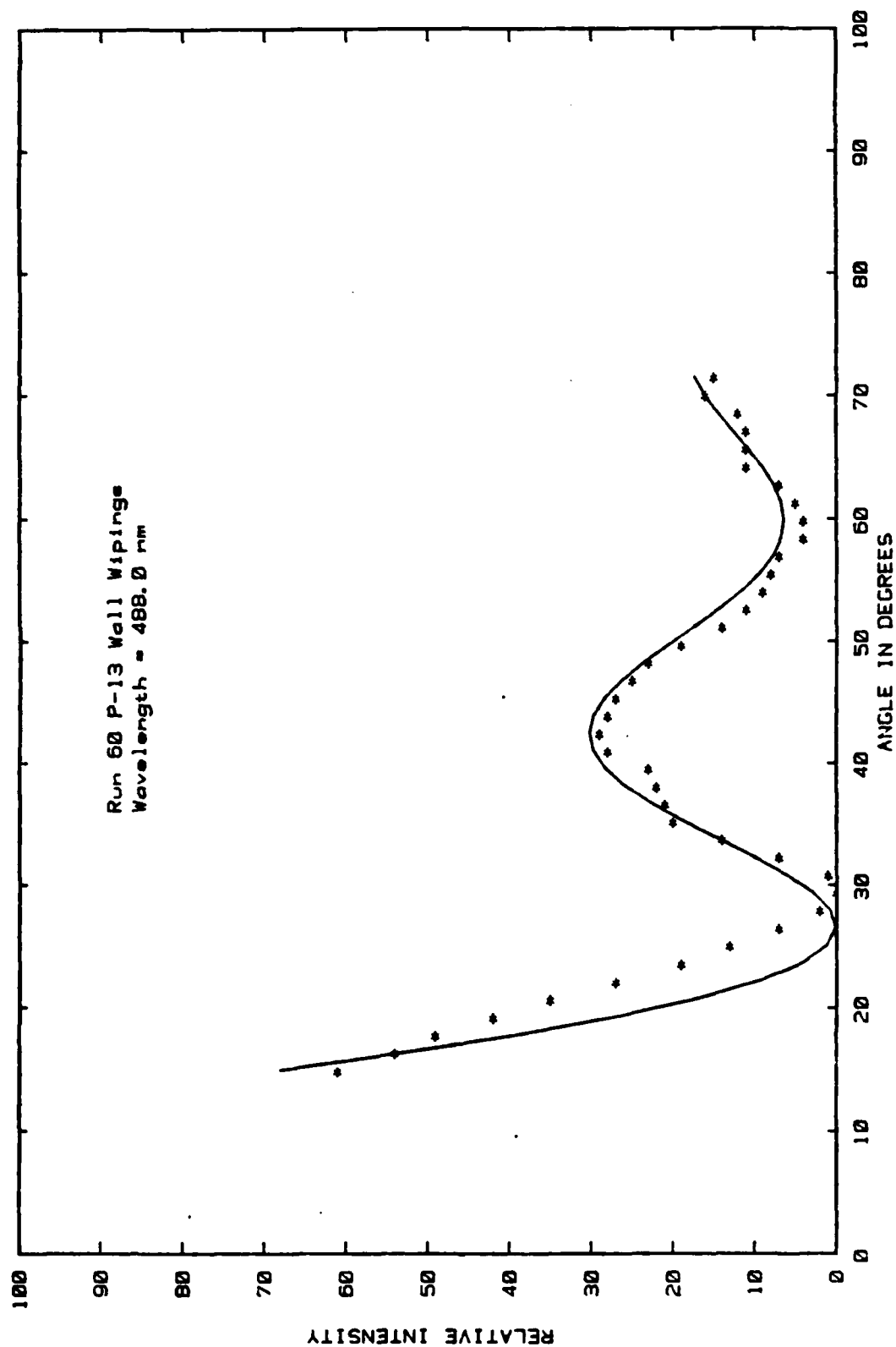


Figure 28. Experimental phase function data (*) for a particle from Run 60 for $\lambda = 488.0$ nm compared with Mie theory (—) for $a = 4.91$ and $m = 1.590 - i0.049$.

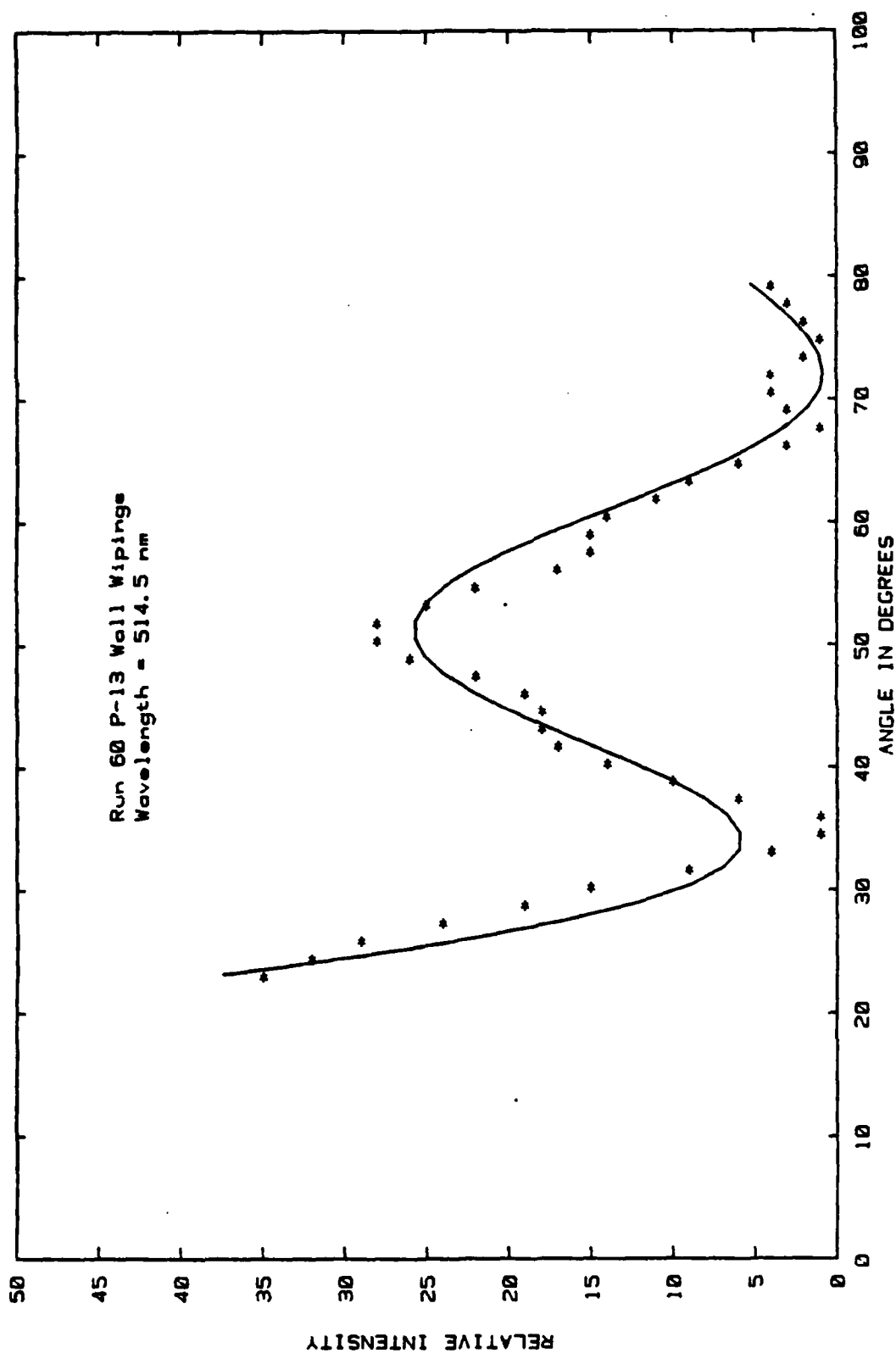


Figure 29. Experimental phase function data (*) for a particle from Run 60 for $\lambda = 514.5$ nm compared with Mie theory (—) for $a = 5.38$ and $m = 1.571 - i0.018$.

these figures. The particle diameters calculated for this particle from the three experiments are 1.401 μm , 1.429 μm and 1.523 μm with a mean of 1.451 μm . the scatter is only about $\pm 5\%$ for this set. There is rather little variation in refractive index for these three runs, as shown in Table 3, which summarizes the results for the runs for which convergence of the matching procedure occurred. Also given in the table are the calculated albedos for each run and the average values of α , m_1 , m_2 for each particle measured at more than one wavelength. Average values of the parameters permit us to compute more comprehensive phase function plots, and Figures 33-35 show composite phase functions for particles from several runs. These figures are based on the mean values of α , m_1 and m_2 reported in Table 3 for each set of data on a particular dust particle.

Additional comparisons between measured phase functions and Mie theory results are given in the appendix, and many of the comparisons show poor agreement with the detailed structure of the intensity profile but broad agreement with the positions of peaks, troughs and general structure. This might be expected of particulates that are not perfect spheres but have blemishes due to outgassing or other phenomena that occurred during solidification after the particle melted.

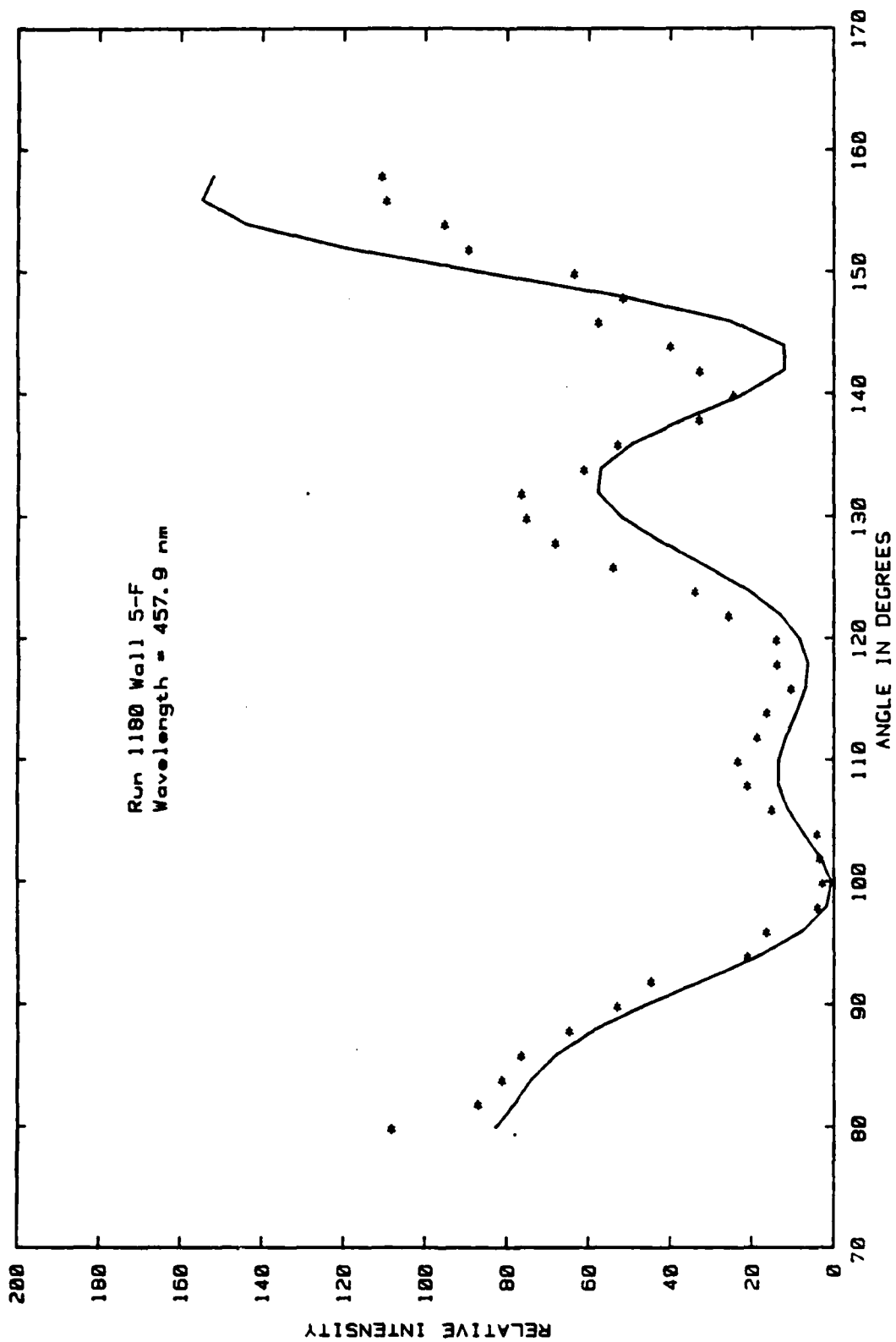


Figure 30. Experimental phase function data (*) for a particle from Run 1180 for $\lambda = 457.9$ nm compared with Mie theory (—) for $\alpha = 9.61$ and $m = 1.719 - i 0.029$.

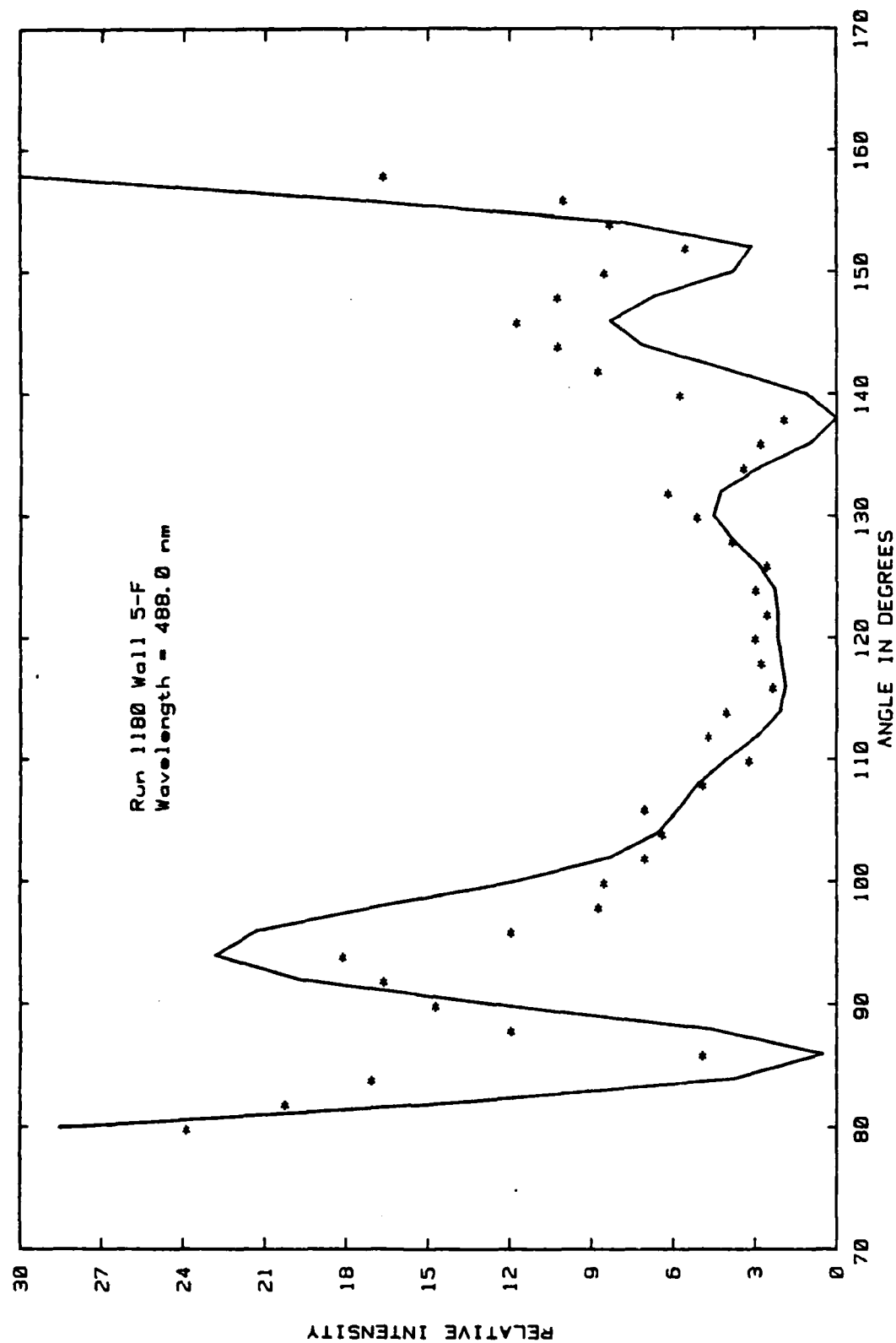


Figure 31. Experimental phase function data (*) for a particle from Run 1180 for $\lambda = 488.0$ nm compared with Mie theory (—) for $\alpha = 9.20$ and $m = 1.716 - i0.001$.

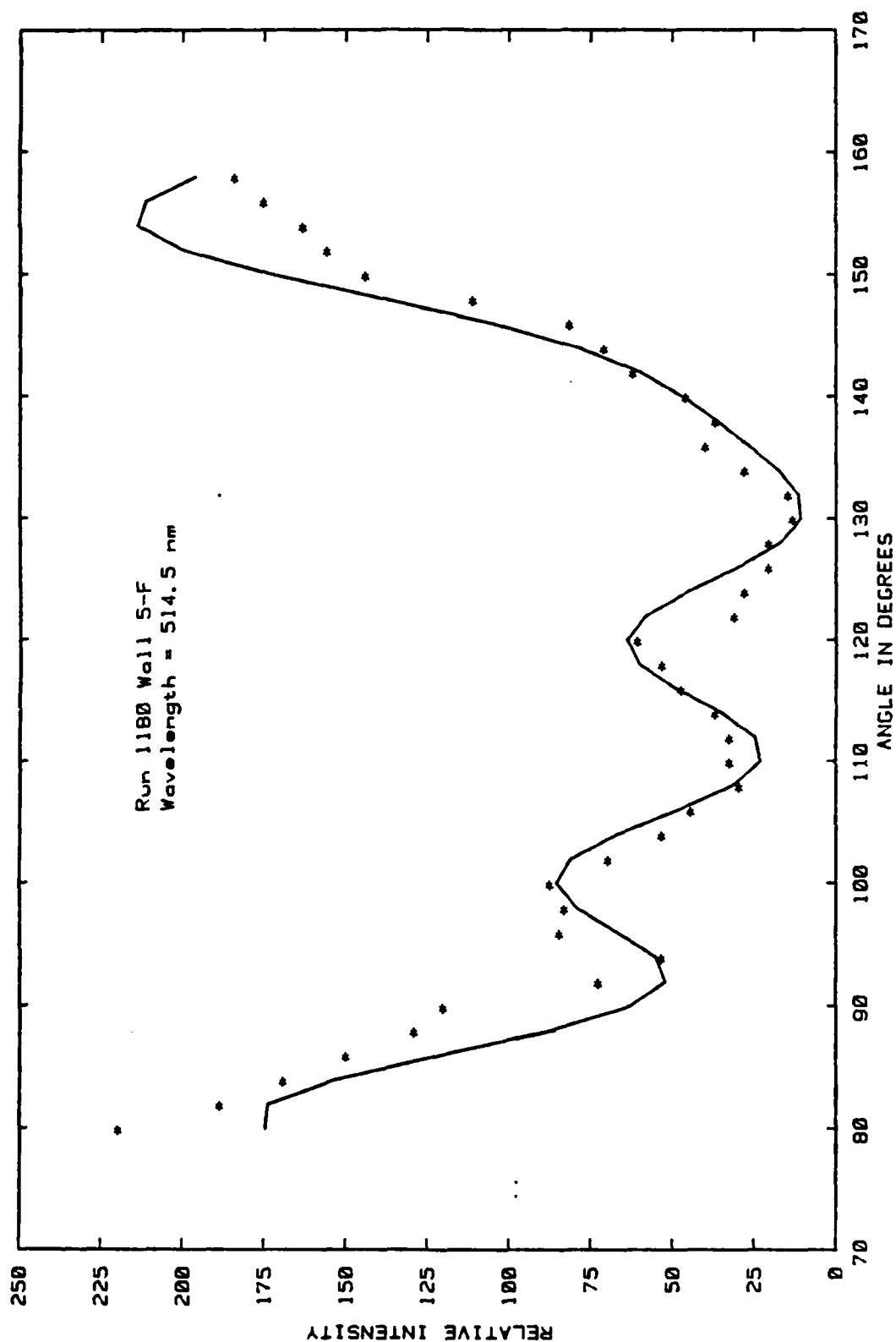


Figure 32. Experimental phase function data (*) for a particle from Run 1180 for $\lambda = 514.5$ nm compared with Mie theory (—) for $\alpha = 9.30$ and $m = 1.709 - i 0.026$.

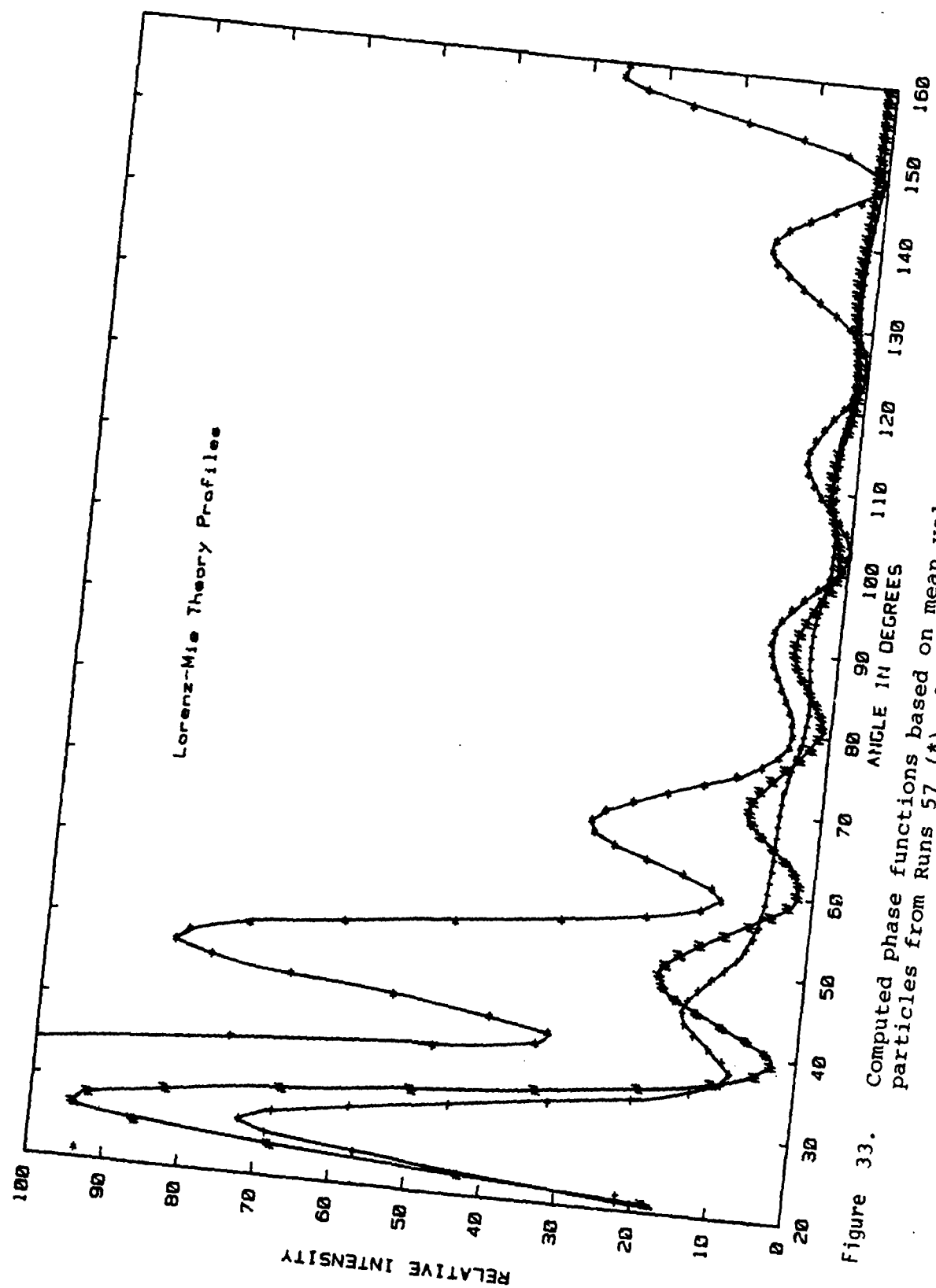


Figure 33. Computed phase functions based on mean values of α and m for particles from Runs 57 (*), 60 (#) and 60(+).

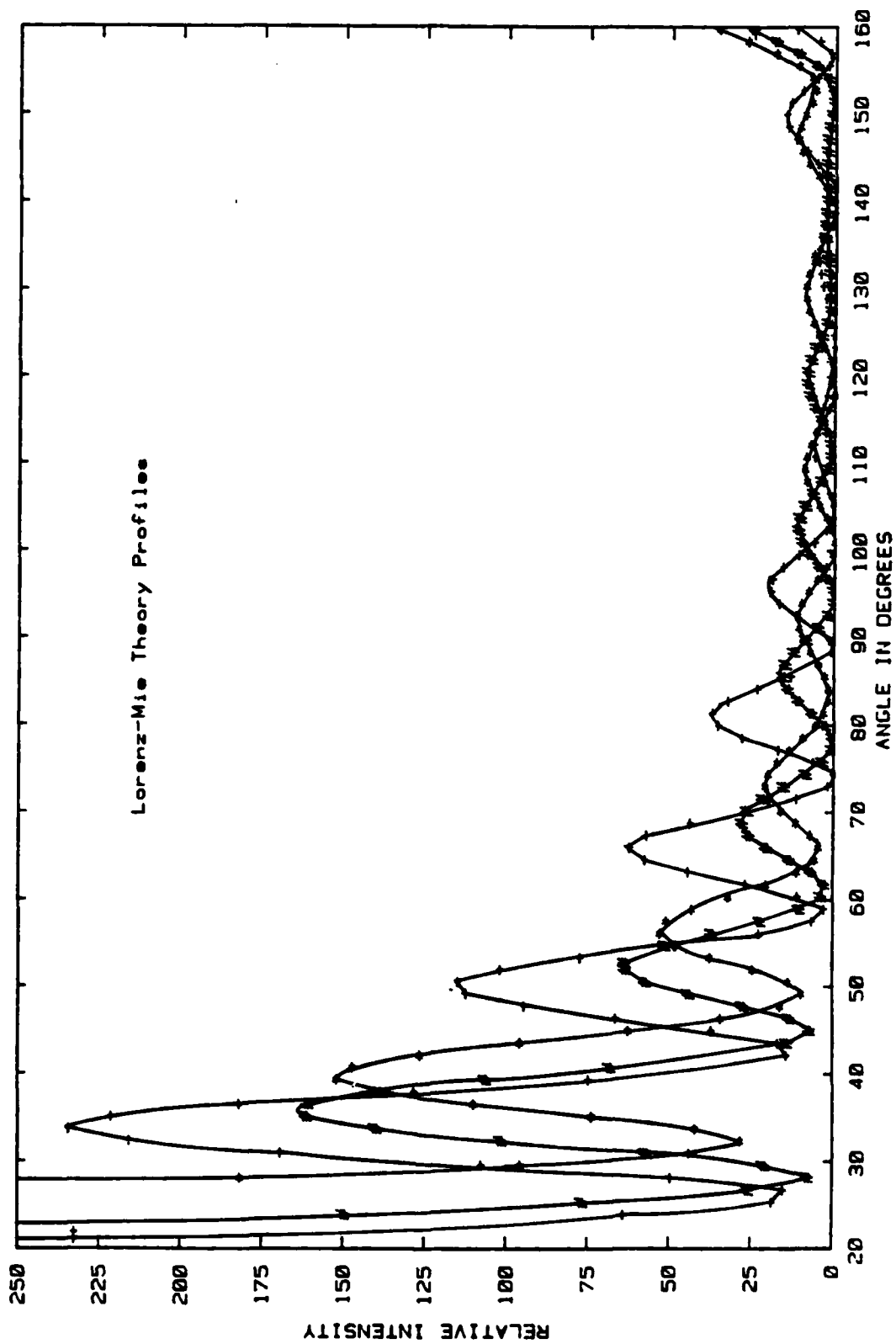


Figure 34. Computed phase functions based on mean values of α and m for particles from Runs 69 (*), 104 (#) and 107 (+).

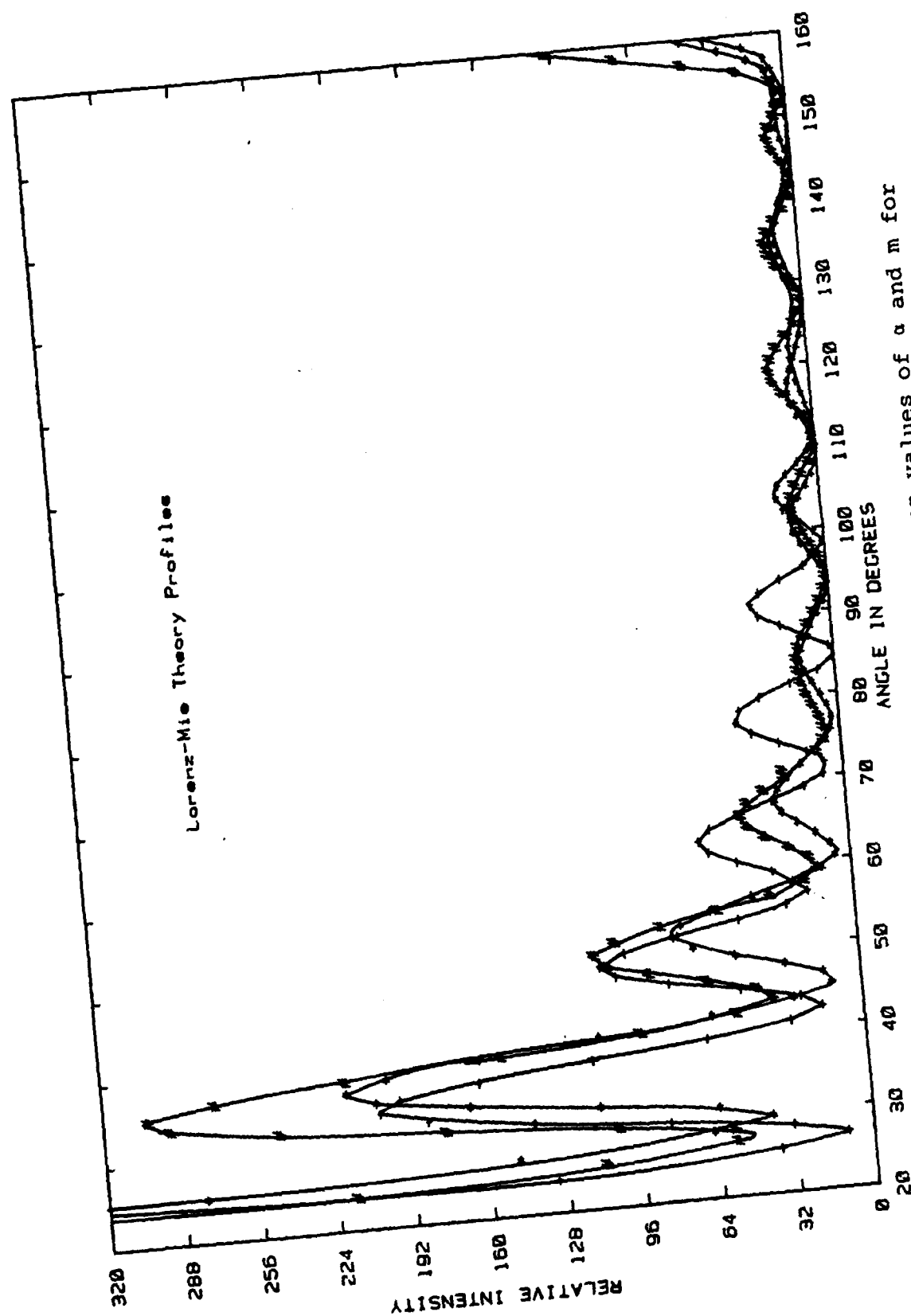


Figure 35. Computed phase functions based on mean values of a and m for particles from Runs 108 (*), 136 (#) and 138 (+).

SECTION 4

DISCUSSION OF RESULTS

Table 3 shows that the values of m_2 determined by comparing phase function data with Mie theory are relatively small (compared with strongly absorbing particulates such as carbon or soot particles for which $m_2 > 0.6$) and scattered. Since m_2 strongly affects the computed albedo, the latter is also scattered. For the small values of m_2 encountered here it is difficult to determine m_2 from noisy phase function data for the reasons suggested by Figure 36, which shows calculated phase functions for a sphere with $\alpha = 10$, $m_1 = 1.600$ and various values of m_2 . The primary effect of increasing m_2 is to decrease the intensity of the scattered light without appreciably shifting the angular positions of peaks and troughs. Thus, it is difficult to extract accurate values of m_2 by inverting the phase function information. The values of m_2 reported here should be construed to be only order of magnitude estimates.

The range of dust particle sizes studied with the electrodynamic balance is considerably smaller than the range of particles shown in the scanning electron micrographs. There are two likely reasons for this discrepancy (i) the number density of micron-size particulates is very much greater than that of larger particulates (say, $D_p > 20 \mu\text{m}$), and (ii) larger particulates injected into the electrodynamic balance have much larger settling velocities than small ones, so the latter are preferentially captured. Efforts were made to randomize the sampling, but few large particulates were encountered in the light-scattering studies.

More than one-half of the particulates studied in the electrodynamic balance could not be compared with Mie theory, for they were not spherical. One indication of asymmetry of a particulate was that when observed through the

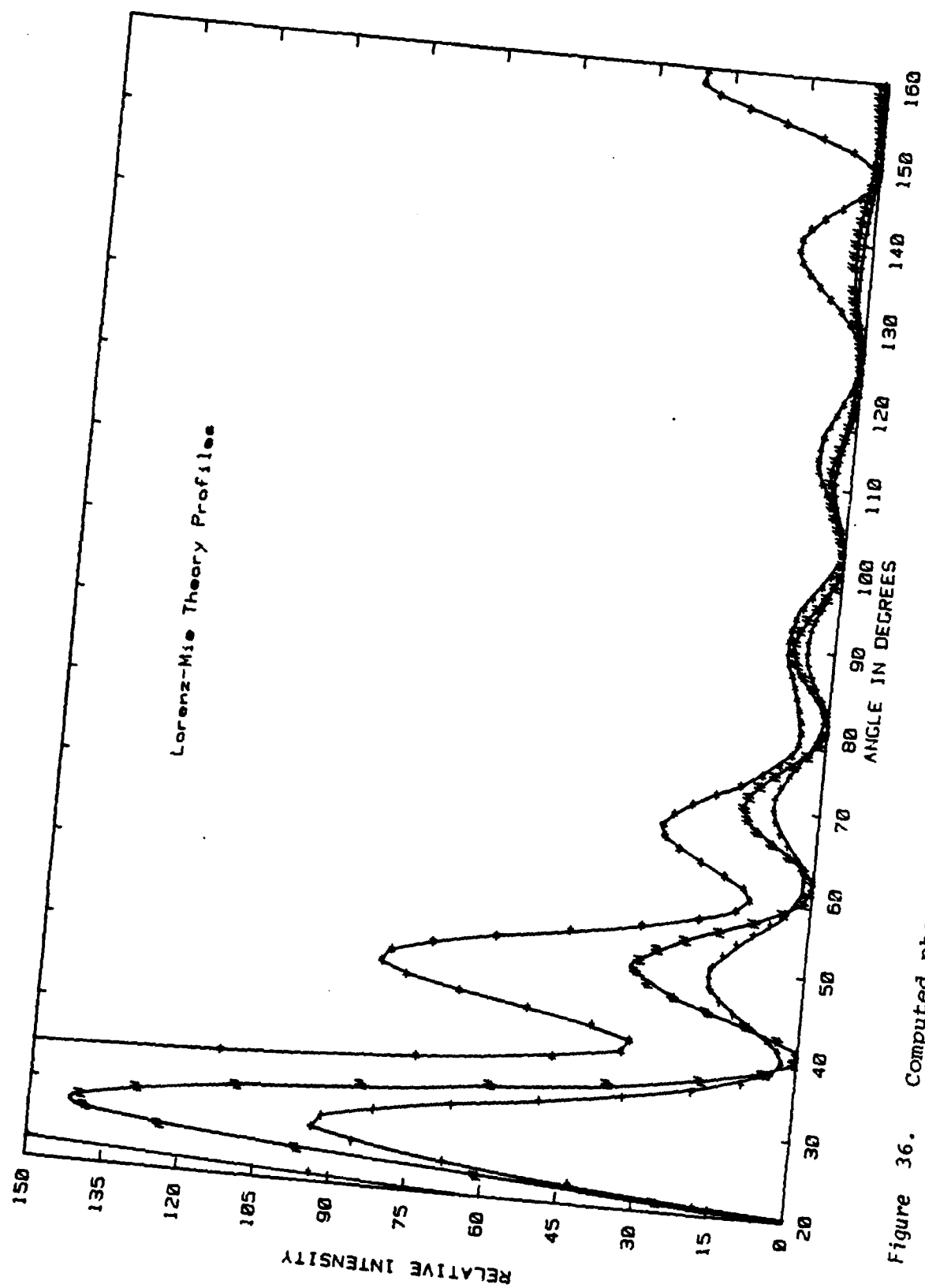


Figure 36. Computed phase functions for a sphere for $\alpha = 1.6$, $m_1 = 1.6$ and $m_2 = 0.0$ (*), 0.025 (#) and 0.05 (+).

Table 3. Results for dust particles for three wavelengths

RUN	λ, nm	α	m_1	m_2	Albedo	$a, \mu\text{m}$
Run 57 P-14 Wall wipings	457.9	12.60	1.551	0.003	0.8385	0.9183
$V_{ac} = 768.0$	488.0	12.77	1.525	0.004	0.8199	0.9921
$V_{dc} = 0.0$	514.5	12.89	1.508	0.005	0.8022	1.056
AVERAGE		12.75	1.528	0.004	0.8202	0.9888
Run 60 P-13 Wall wipings	457.9	5.008	1.705	0.054	0.4917	0.365
$V_{ac} = 1176.0$	488.0	4.910	1.590	0.049	0.6216	0.3814
$V_{dc} = 112.0$	514.5	5.378	1.571	0.018	0.7578	0.4404
AVERAGE		5.099	1.622	0.040	0.6237	0.3956
Run 60 P-13 Wall wipings	457.9	4.604	1.626	0.036	0.6688	0.3355
$V_{ac} = 768.0$	488.0	4.841	1.600	0.030	0.7054	0.376
$V_{dc} = 33.1$	514.5	4.618	1.633	0.026	0.7213	0.3782
AVERAGE		4.688	1.620	0.031	0.6985	0.3632
Run 69 RB5I-2 Wall wipings	457.9	12.53	1.562	0.003	0.8501	0.9130
$V_{ac} = 600.0$	488.0	11.84	1.557	0.005	0.8164	0.9194
$V_{dc} = 0.466$	514.5	11.44	1.490	0.012	0.7502	0.9370
AVERAGE		11.94	1.536	0.006	0.8056	0.9231

Table 3. Results for dust particles for three wavelengths (Continued)

RUN	λ, nm	α	m_1	m_2	Albedo	$a, \mu\text{m}$
Run 104 RC5Y-2 Wall wipings	457.9	12.23	1.601	0.024	0.5589	0.8915
$V_{ac} = 888.0$	488.0	12.18	1.593	0.007	0.7619	0.9463
$V_{dc} = 0.906$	514.5	12.38	1.573	0.008	0.7243	1.014
AVERAGE		12.26	1.589	0.013	0.6817	0.9506
Run 107 P-14 Wall wiper sample RC4U-3	457.9	13.65*	1.594*	0.006*	0.8028*	0.9948*
$V_{ac} = 768.0$	488.0	12.40	1.574	0.007	0.7417	0.9631
$V_{dc} = 0.792$	514.5	12.53	1.559	0.005	0.7816	1.026
AVERAGE		12.86	1.576	0.006	0.7754	0.9946
Run 108 Wall wipings	457.9	12.75	1.529	0.005	0.8013	0.9291
$V_{ac} = 744.0$	488.0	12.88	1.510	0.005	0.796	1.000
$V_{dc} = 0.675$	514.5	13.08	1.481	0.007	0.78	1.0711
AVERAGE		12.90	1.507	0.006	0.7924	1.000
Run 136 RBU2 #15 Wall wipings	457.9	-	-	-	-	-
$V_{ac} = 1032.0$	488.0	12.40	1.582	0.002	0.8861	0.9632
$V_{dc} = 0.695$	514.5	-	-	-	-	-
AVERAGE		12.40	1.582	0.002	0.8861	0.9632

* extrapolated

Table 3. Results for dust particles for three wavelengths (Concluded)

RUN	λ, nm	α	m_1	m_2	Albedo	$a, \mu\text{m}$
Run 138 Black Tile Wall						
wipings	457.9	14.14	1.723	0.007	0.7091	1.0303
$V_{ac} = 768.0$	488.0	14.59	1.674	0.010	0.6716	1.1332
$V_{dc} = 1.27$	514.5	15.06	1.613	0.000	0.9892	1.2333
AVERAGE		14.60	1.670	0.006	0.79	1.1323
Run 1180 Wall 5-F						
	457.9	9.61	1.719	0.029	0.5531	0.7004
$V_{ac} = 1824.0$	488.0	9.20	1.716	0.001	0.9369	0.7145
$V_{dc} = 62.0$	514.5	9.30	1.709	0.026	0.5768	0.7615
AVERAGE		9.37	1.715	0.019	0.689	0.7255

microscope eyepiece on the picobalance the particle "twinkled" due to irregular scattering as it rotated. Light-scattering data taken with such particles showed no reproducibility during forward and backward scans of the traversing photomultiplier tube, and those data are not included in this report.

The real parts of the refractive indices determined in this research are generally consistent with refractive indices reported for minerals (silicates, clay, mica, etc.). Table 4 lists typical values of m_1 for feldspars, clay, mica and other silicates containing Al, Ca, Mg and Na. The range of values listed in Table 4 is about the same as that determined here for the various soil samples.

There is no clearcut dependence of refractive index on wavelength for the wavelengths studied here and in Phase I of the project (457.9 nm - 632.8 nm), but it is to be expected that in the ultraviolet region of the spectrum m_2 is larger, for the silicates can be expected to absorb in the UV range.

There is also no well-defined variation in optical properties from one soil sample to another, for variations between individual particles in a single sample are large. That is clear from an examination of the SEM data in Section 3, for the particulates vary greatly in size, structure and melting points.

Table 4. Refractive indices of minerals

<u>NAME</u>	<u>FORMULA</u>	<u>REFRACTIVE INDEX, m_1</u>
Andesine	$(\text{CaO}, \text{Na}_2\text{O})\text{Al}_2\text{O}_3 \cdot 4\text{SiO}_2$	1.549
Anorthite	$\text{CaO} \cdot \text{Al}_2\text{O}_3 \cdot 2\text{SiO}_2$	1.5755
Anorthoclase	$(\text{Na}, \text{K})_2\text{O} \cdot \text{Al}_2\text{O}_3 \cdot 6\text{SiO}_2$	1.523
Laboradorite	$\text{NaAlSi}_3\text{O}_8 + \text{CaAl}_2\text{Si}_2\text{O}_8$	1.559
Oligoclase	$\text{NaAlSi}_3\text{O}_8 + \text{CaAl}_2\text{SiO}_8$	1.539
Orthoclase	$\text{K}_2\text{O} \cdot \text{Al}_2\text{O}_3 \cdot 6\text{SiO}_2$	1.518
Wollastonite	CaSiO_3	1.616
Kaolinite (china clay)	$\text{Al}_2\text{O}_3 \cdot 2\text{SiO}_2 \cdot 2\text{H}_2\text{O}$	1.561
Muscovite (white mica)	$\text{K}_2\text{O} \cdot 3\text{Al}_2\text{O}_3 \cdot 6\text{SiO}_2 \cdot 2\text{H}_2\text{O}$	1.561
Analcite	$\text{NaAlSi}_2\text{O}_6 \cdot \text{H}_2\text{O}$	1.479-1.493
Andalusite	Al_2OSiO_4	1.629-1.640
Clinozoisite	$\text{Ca}_2\text{Al}_3\text{Si}_3\text{O}_{12}(\text{OH})$	1.670-1.715
Enstatite	MgSiO_3	1.650-1.662
Forsterite	Mg_2SiO_4	1.635
Gehlenite	$\text{Ca}_2\text{Al}_2\text{SiO}_7$	1.669
Kyanite	Al_2OSiO_4	1.712-1.718

APPENDIX I

EXPERIMENTAL PHASE FUNCTION DIAGRAMS FOR THE DUST PARTICLES

The following phase function diagrams are presented in the same order of increasing run number used for Figures 14-26. In some cases the experimental data are compared with Mie theory, but in others the inversion of the phase function data by means of the iterative optimization procedure discussed in Section 2 did not converge, so the parameters α , m_1 and m_2 could not be determined.

PREVIOUS PAGE
IS BLANK



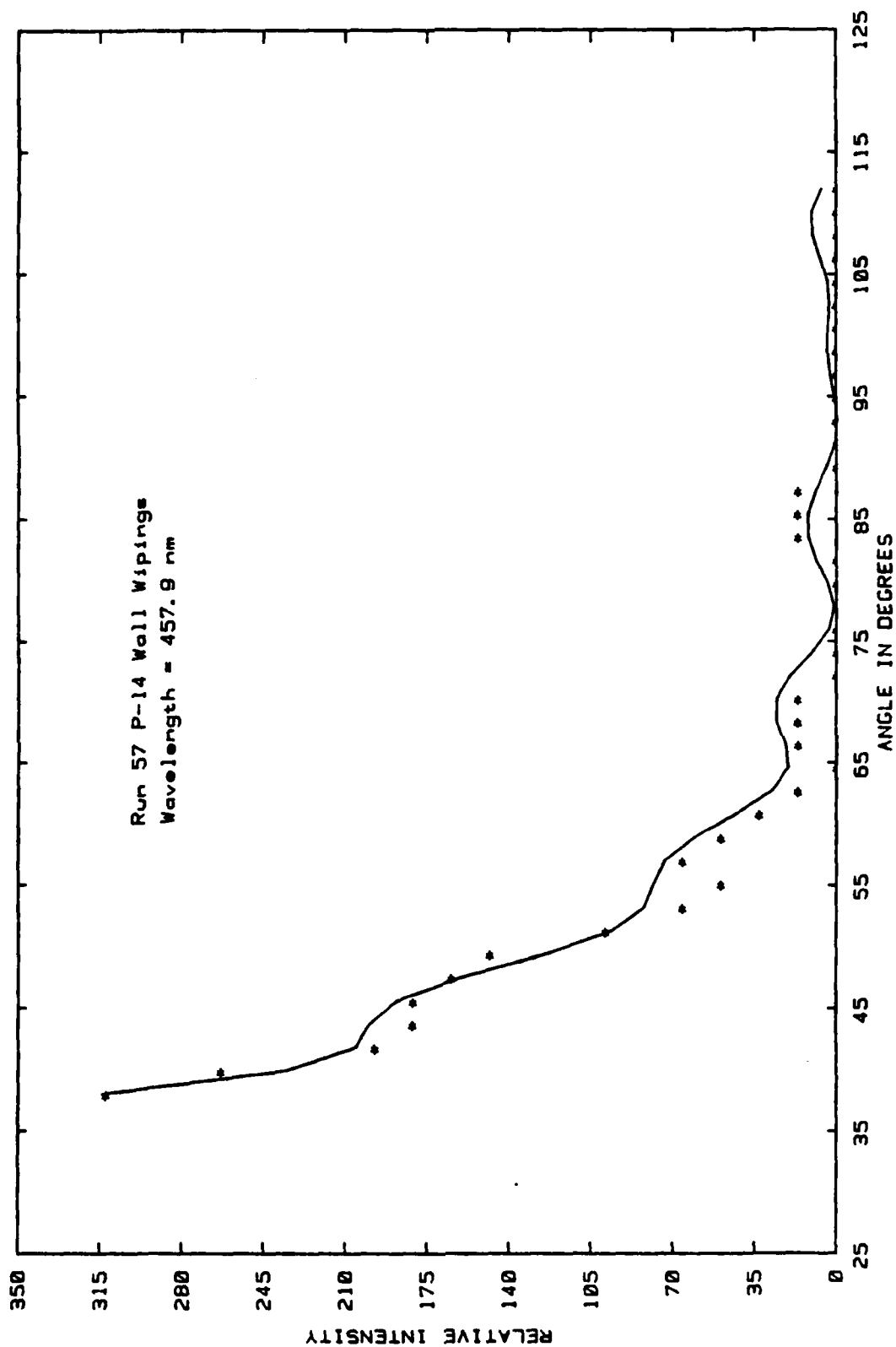


Figure A1. Experimental phase function data (*) for a particle from Run 57 for $\lambda = 457.9$ nm compared with Mie theory (—) for $a = 12.6$ and $m = 1.55 - i0.003$.

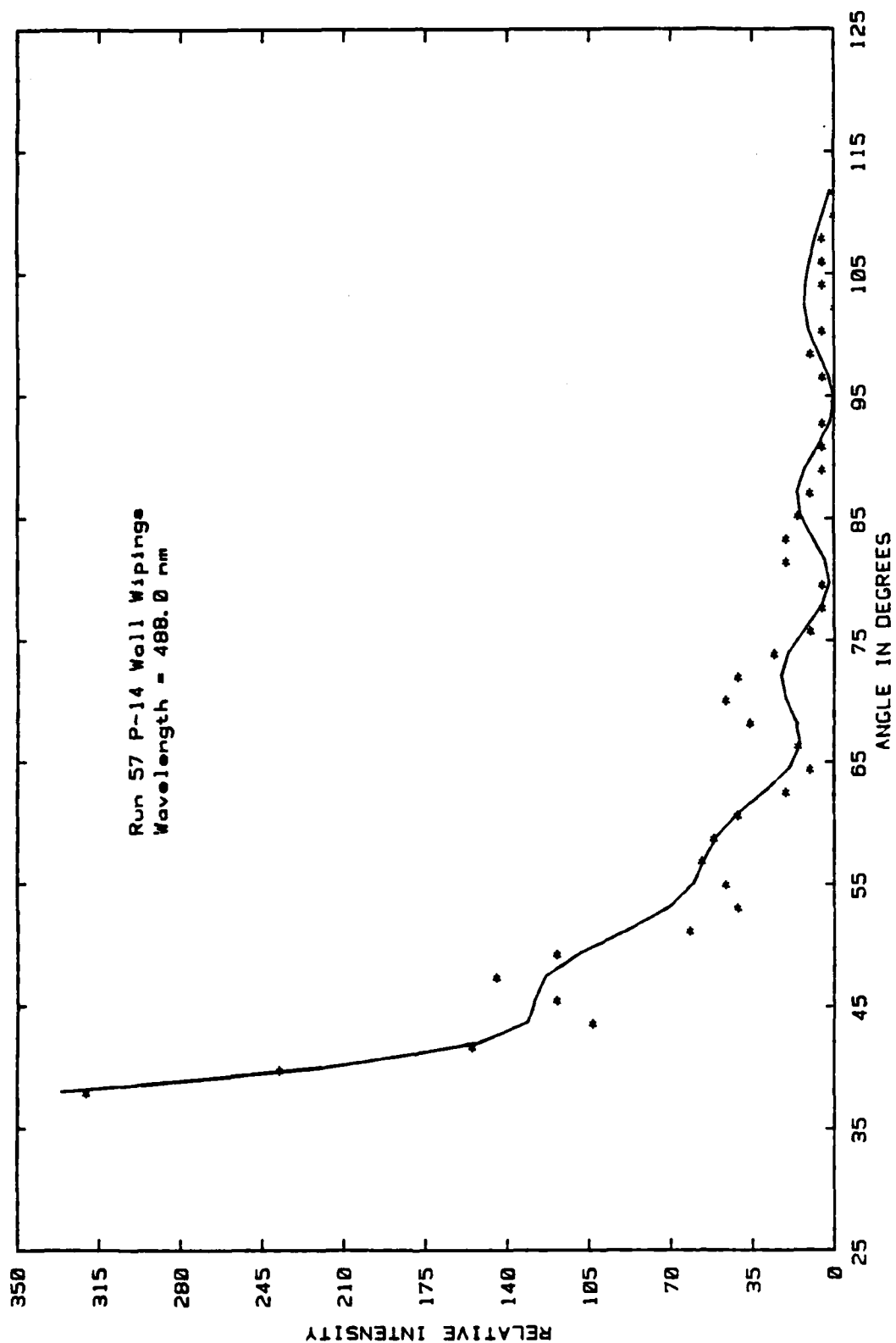


Figure A2. Experimental phase function data (*) for a particle from Run 57 for $\lambda = 488.0$ nm compared with Mie theory (—) for $\alpha = 12.8$ and $m = 1.525 - i0.004$.

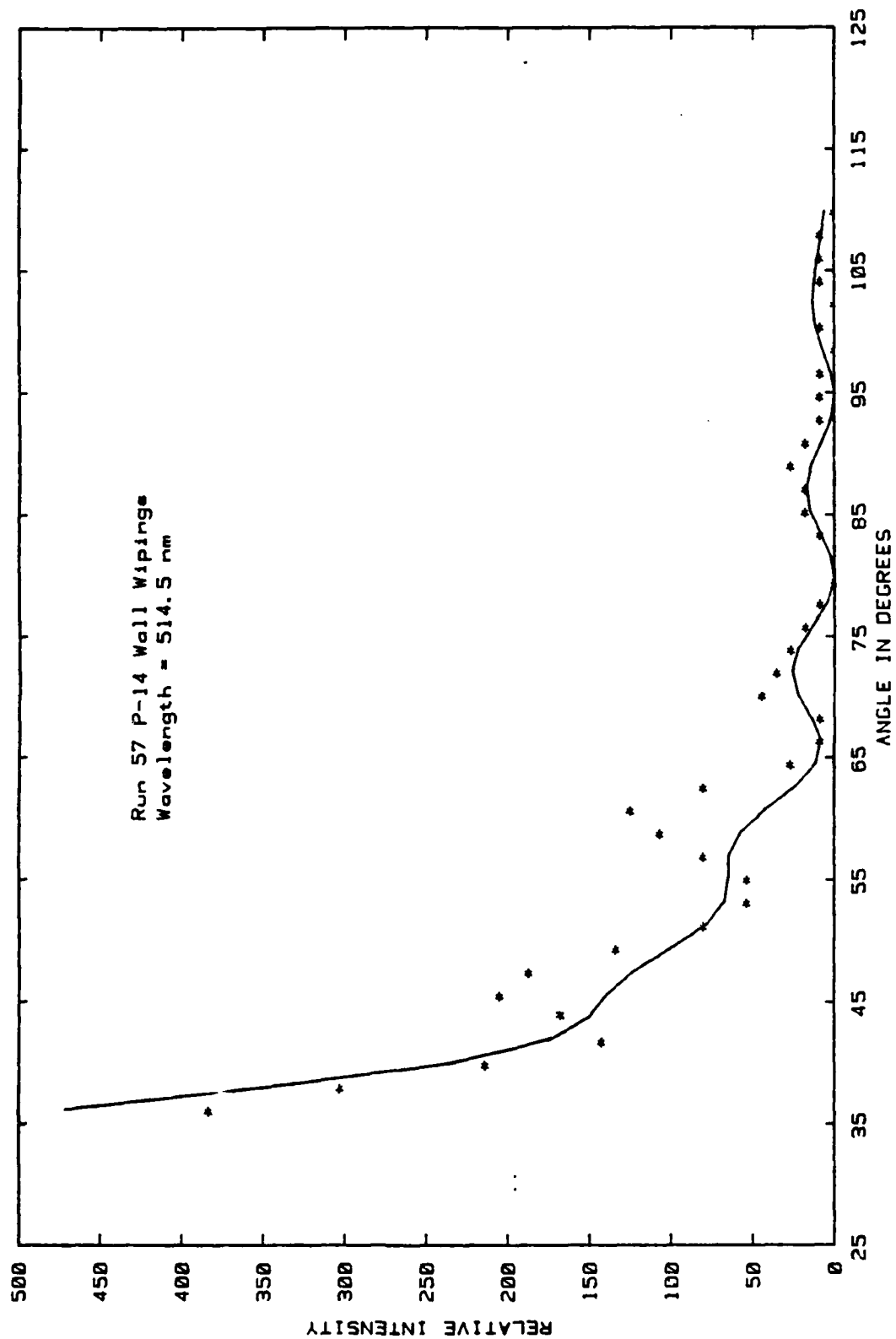


Figure A3. Experimental phase function data (*) for a particle from Run 57 for $\lambda = 514.5$ nm compared with Mie theory (—) for $\alpha = 12.9$ and $m = 1.508 - i0.005$.

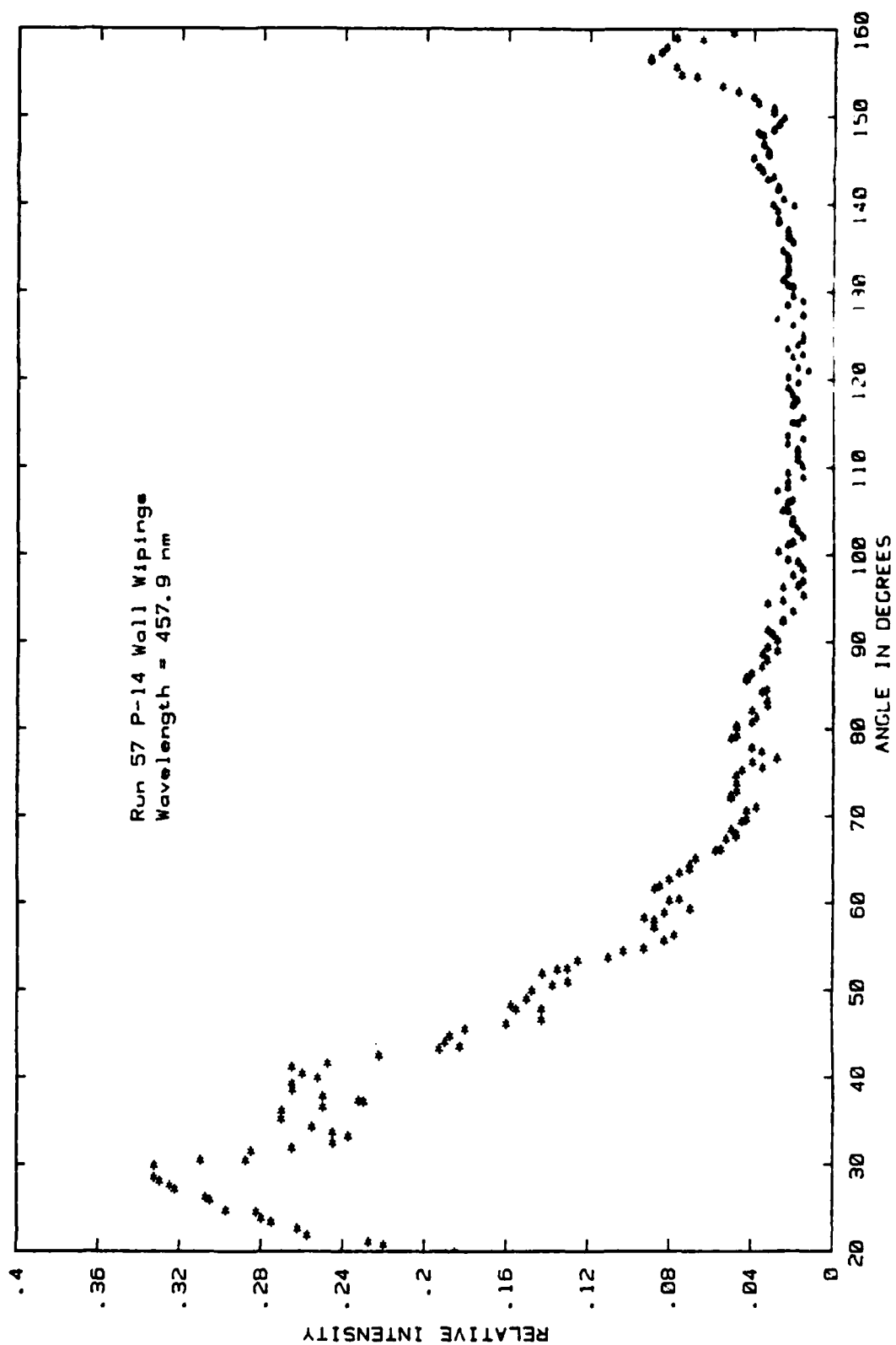


Figure A4. Experimental phase function data (*) for a particle from Run 57 for $\lambda = 457.9$ nm.

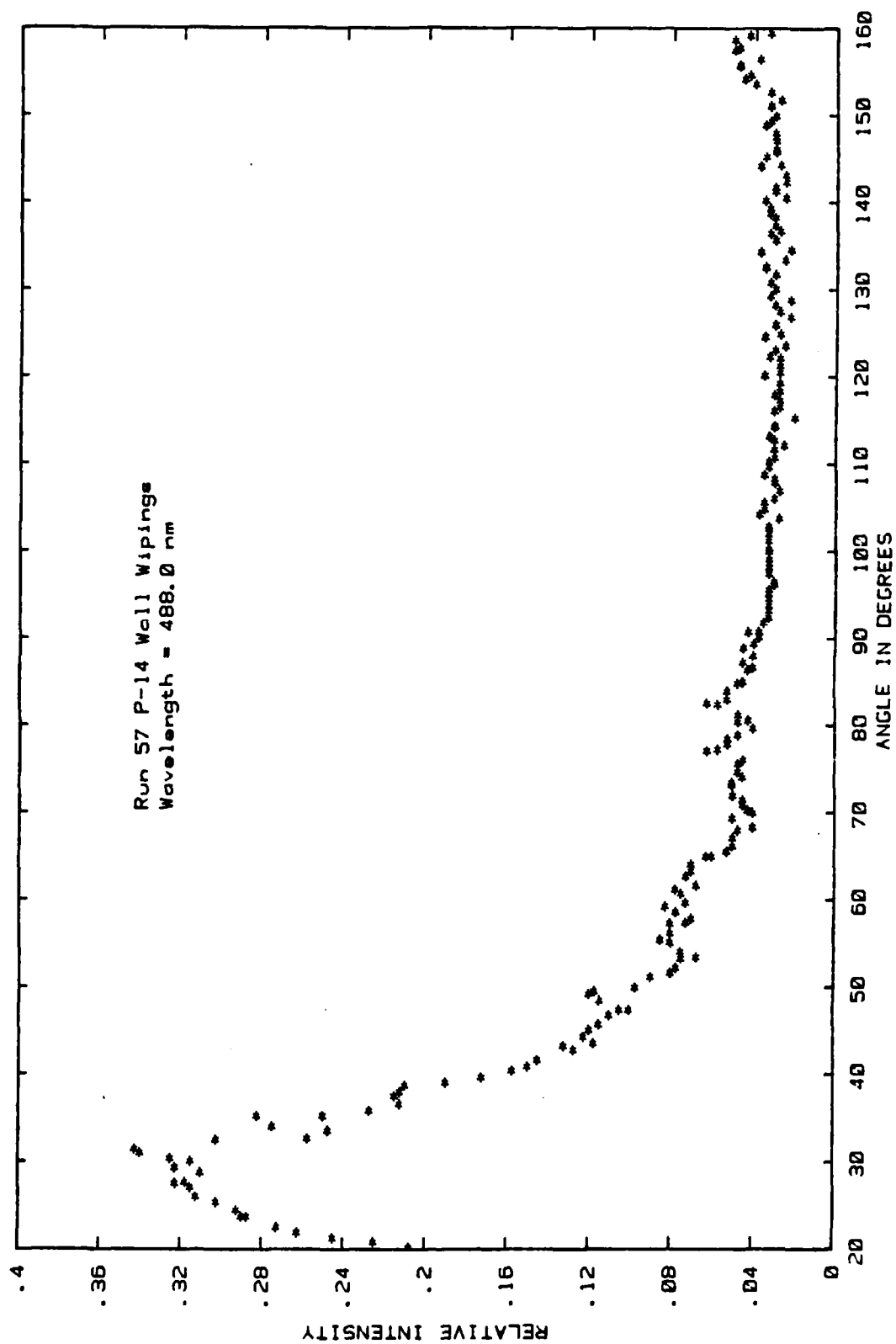


Figure A5. Experimental phase function data (*) for a particle from Run 57 for $\lambda = 488.0$ nm.

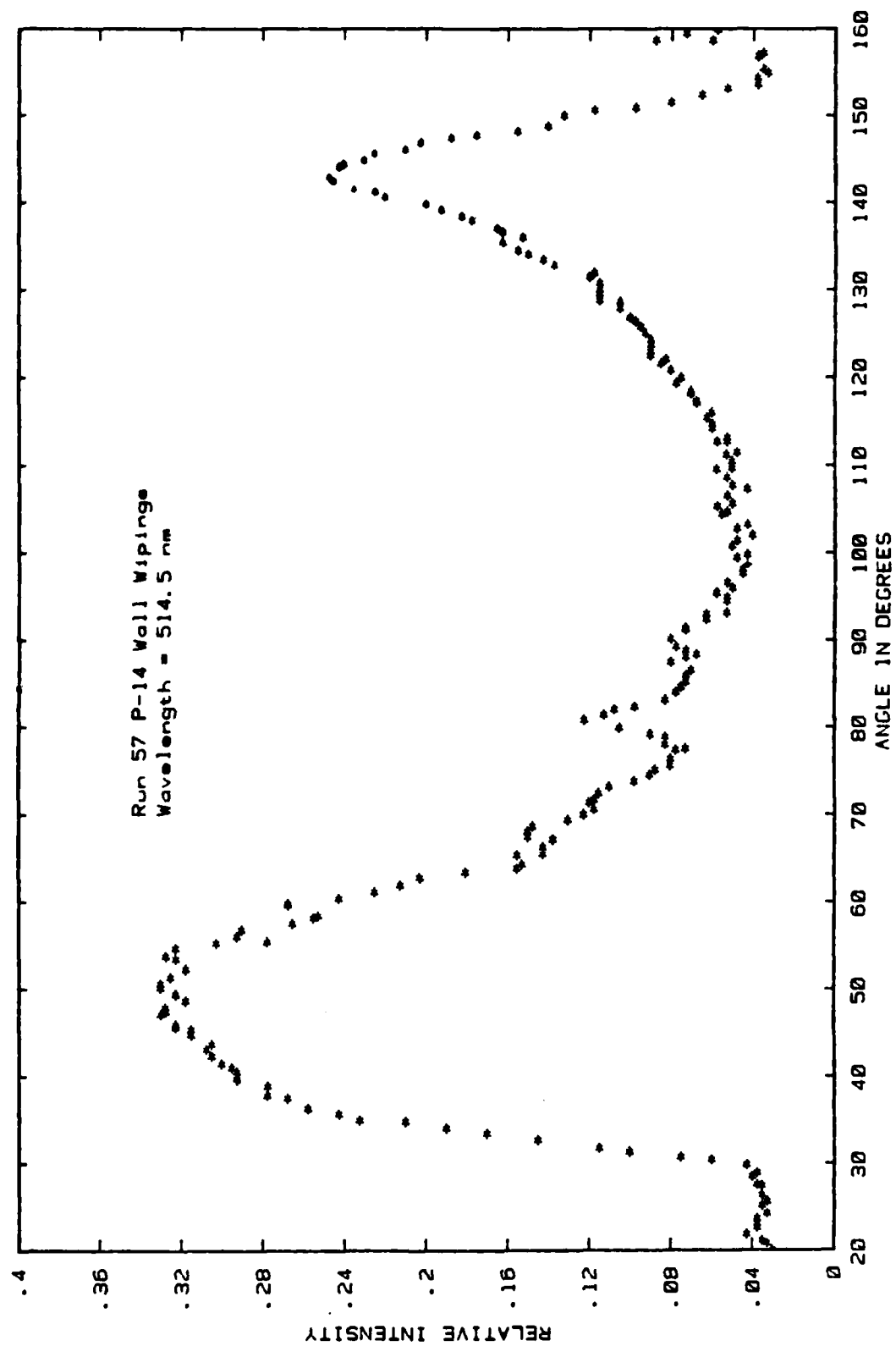


Figure A6. Experimental phase function data (*) for a particle from Run 57 for $\lambda = 514.5$ nm.

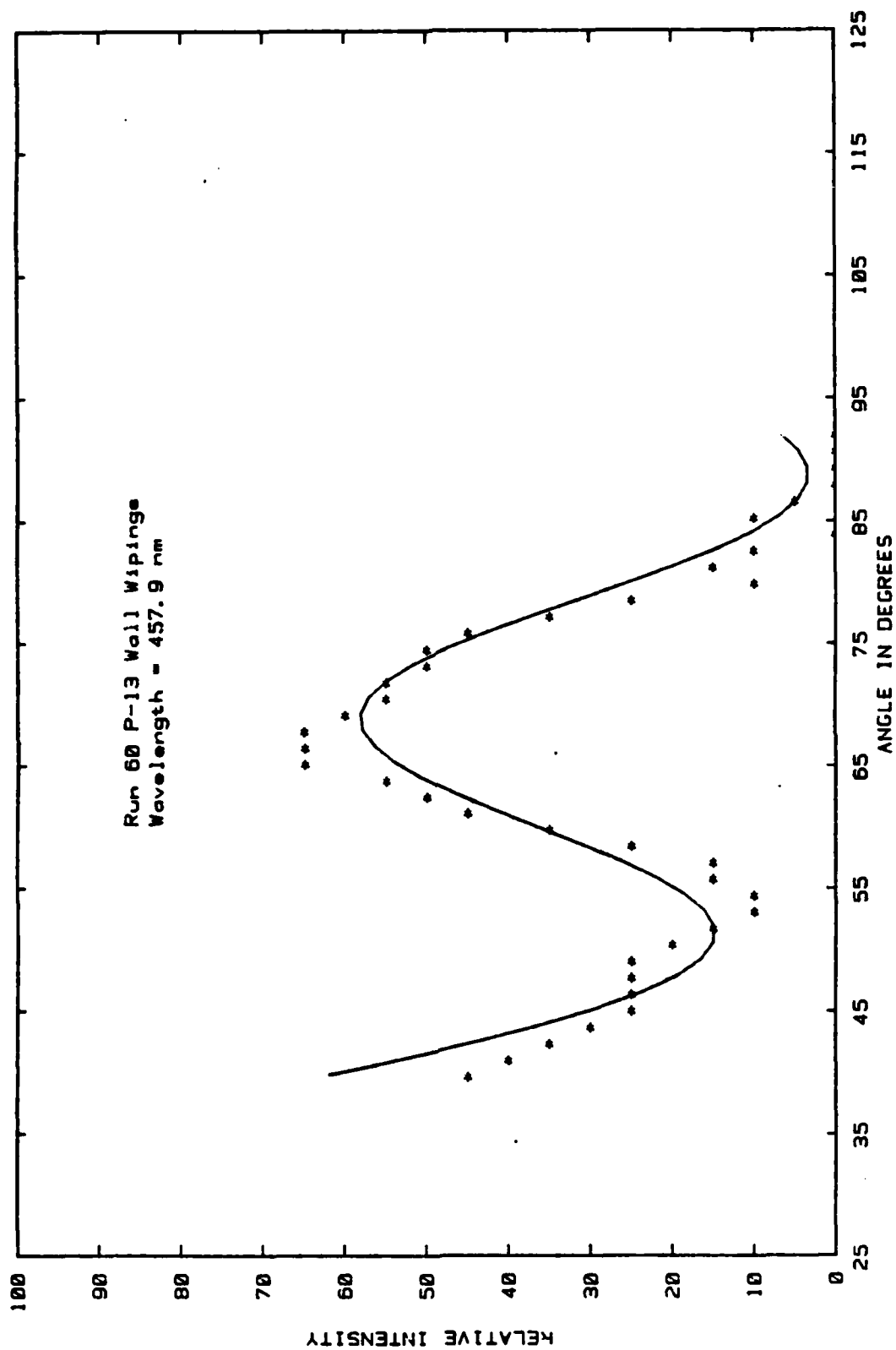


Figure A7. Experimental phase function data (*) for a particle from Run 60 for $\lambda = 457.9$ nm compared with mie theory (—) for $a = 4.60$ and $m = 1.626 - i0.036$.

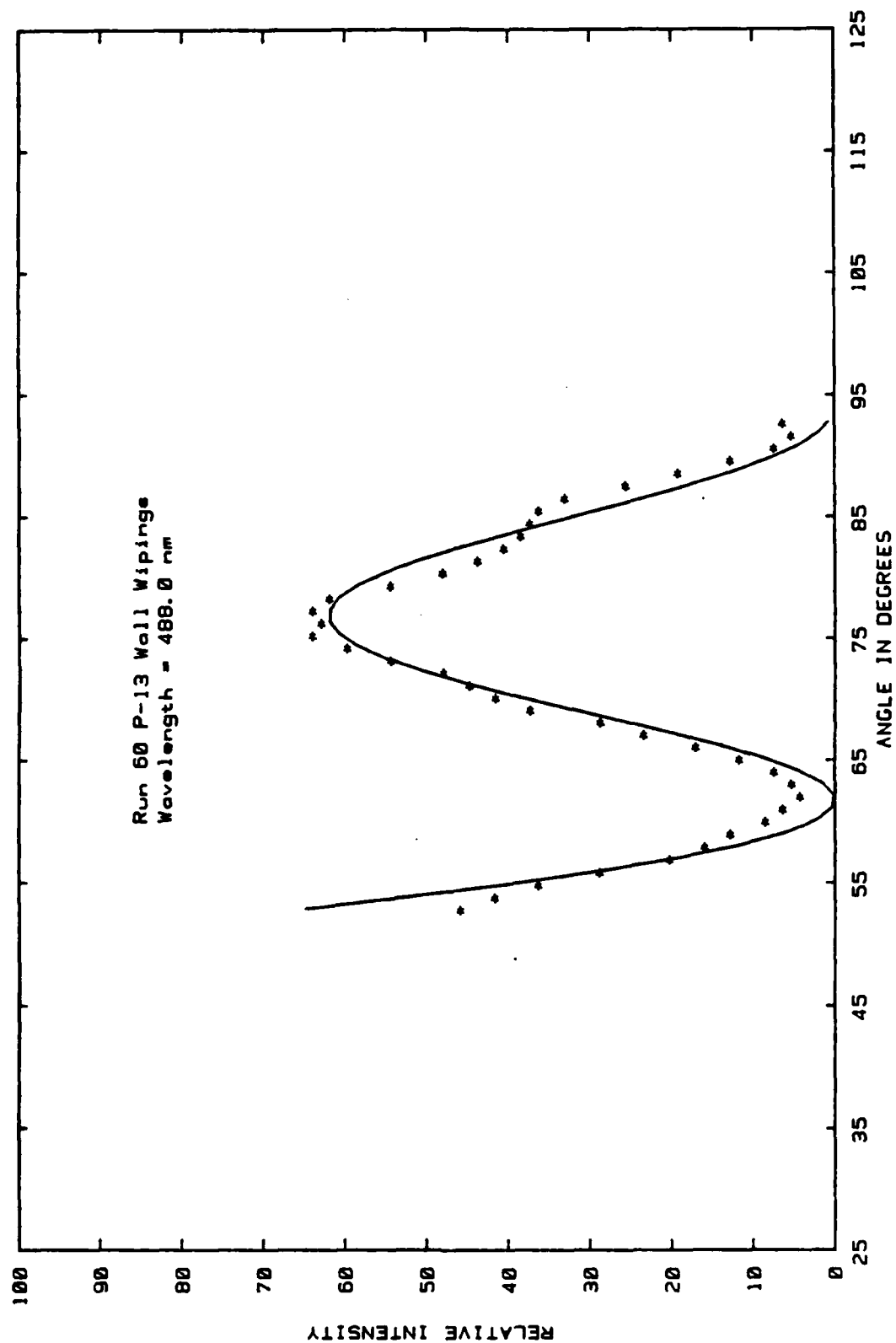


Figure A8. Experimental phase function data (*) for a particle from Run 60 for $\lambda = 488.0$ nm compared with Mie theory (—) for $a = 4.84$ and $m = 1.600 - i0.030$.

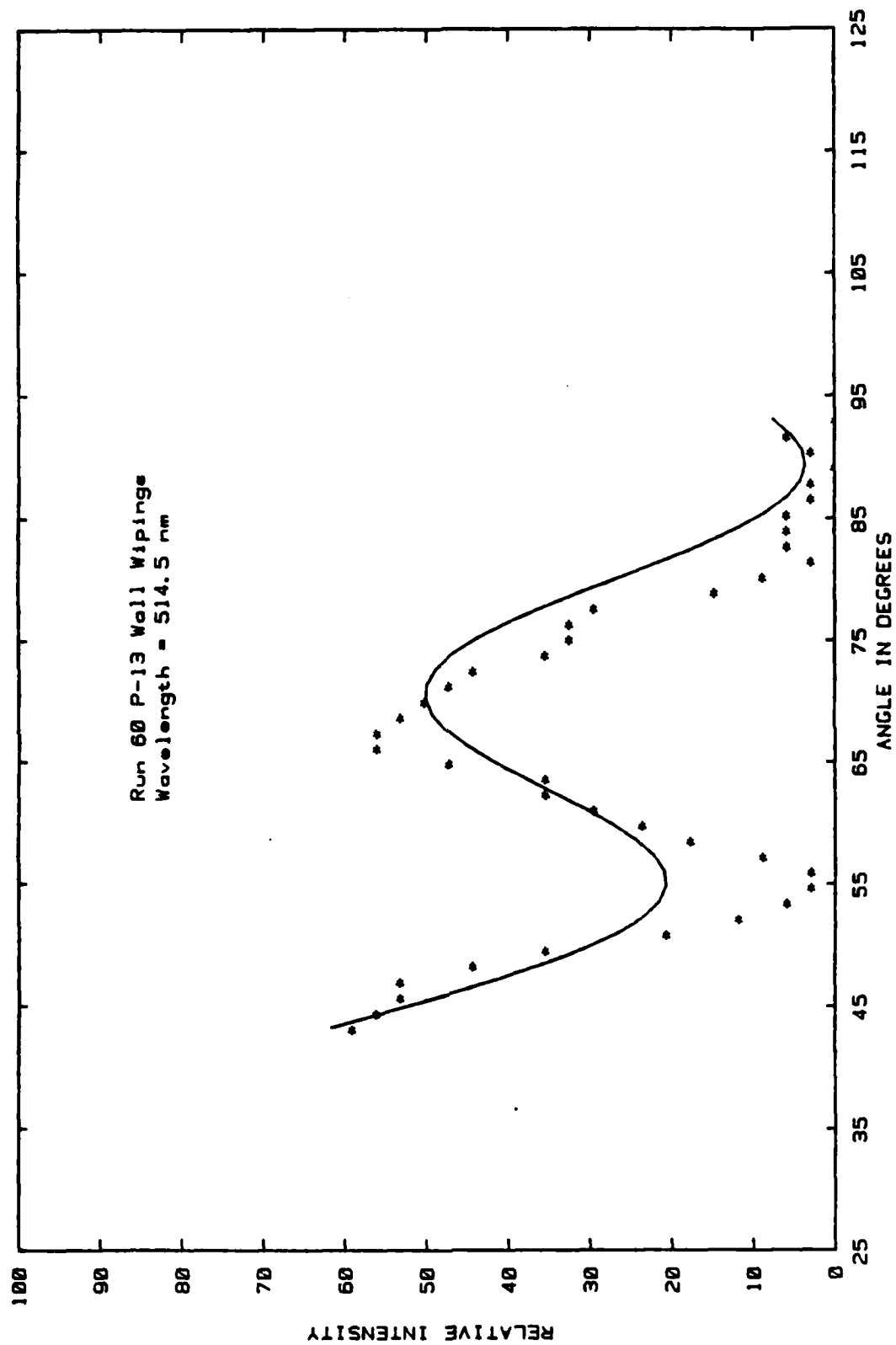


Figure A9. Experimental phase function data (*) for a particle from Run 60 for $\lambda = 514.5$ nm compared with Mie theory (—) for $a = 4.62$ and $m = 1.633 - i0.026$.

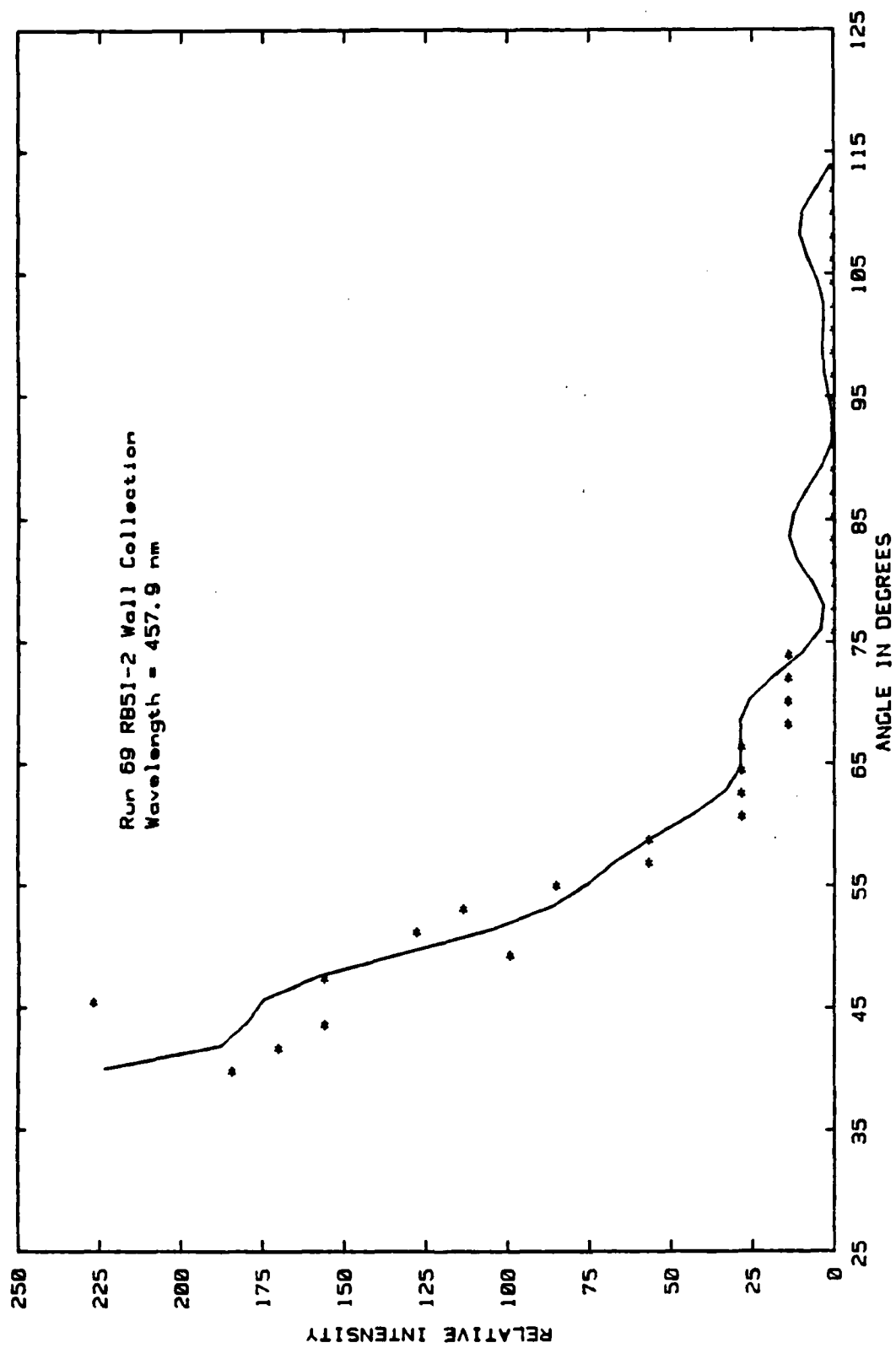


Figure A10. Experimental phase function data (*) for a particle from Run 69 for $\lambda = 457.9$ nm compared with Mie theory (—) for $\alpha = 12.5$ and $m = 1.562 - i0.003$.

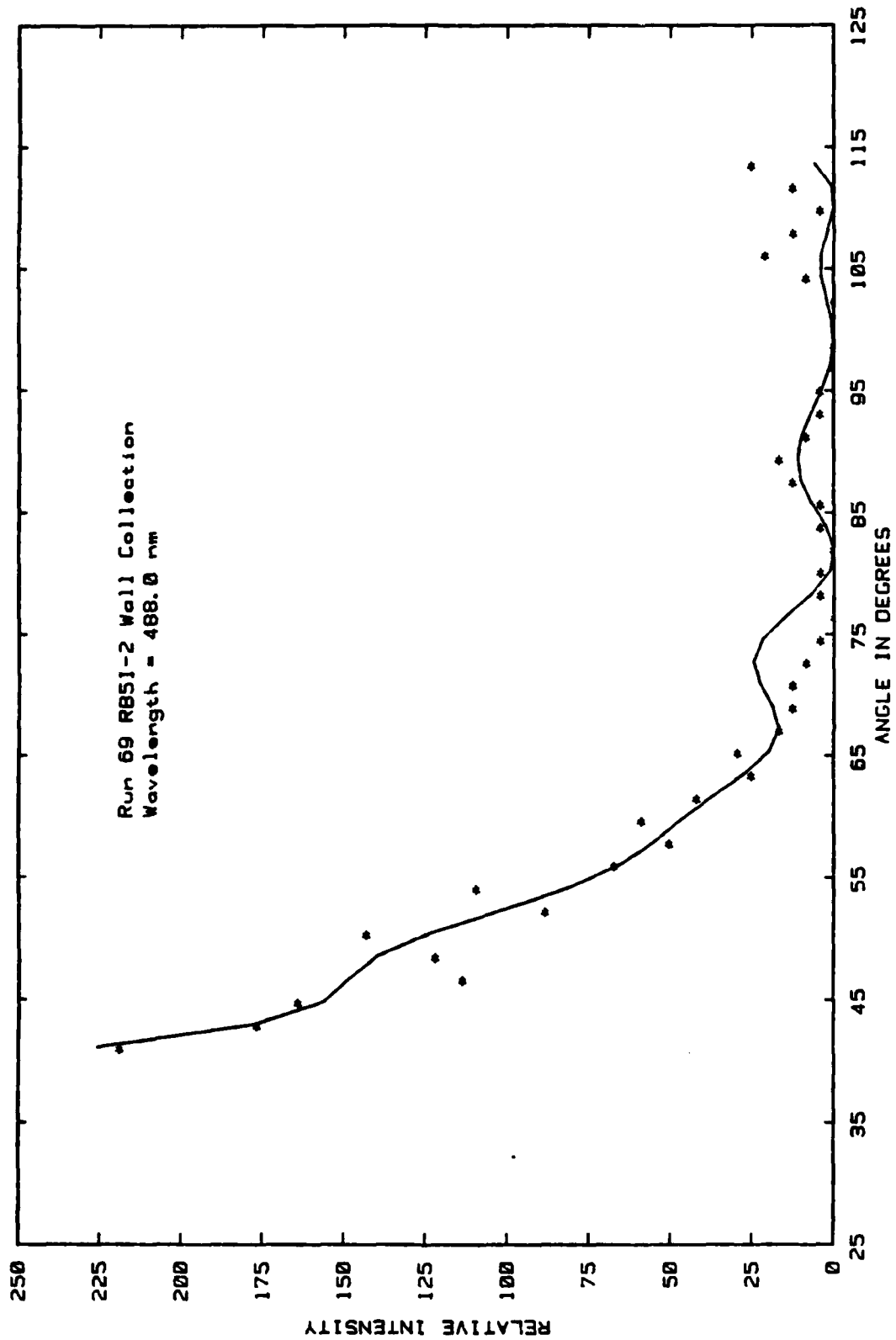


Figure All. Experimental phase function data (*) for a particle from Run 69 for $\lambda = 488.0$ nm compared with Mie theory (—) for $a = 11.8$ and $m = 1.557 - i0.005$.

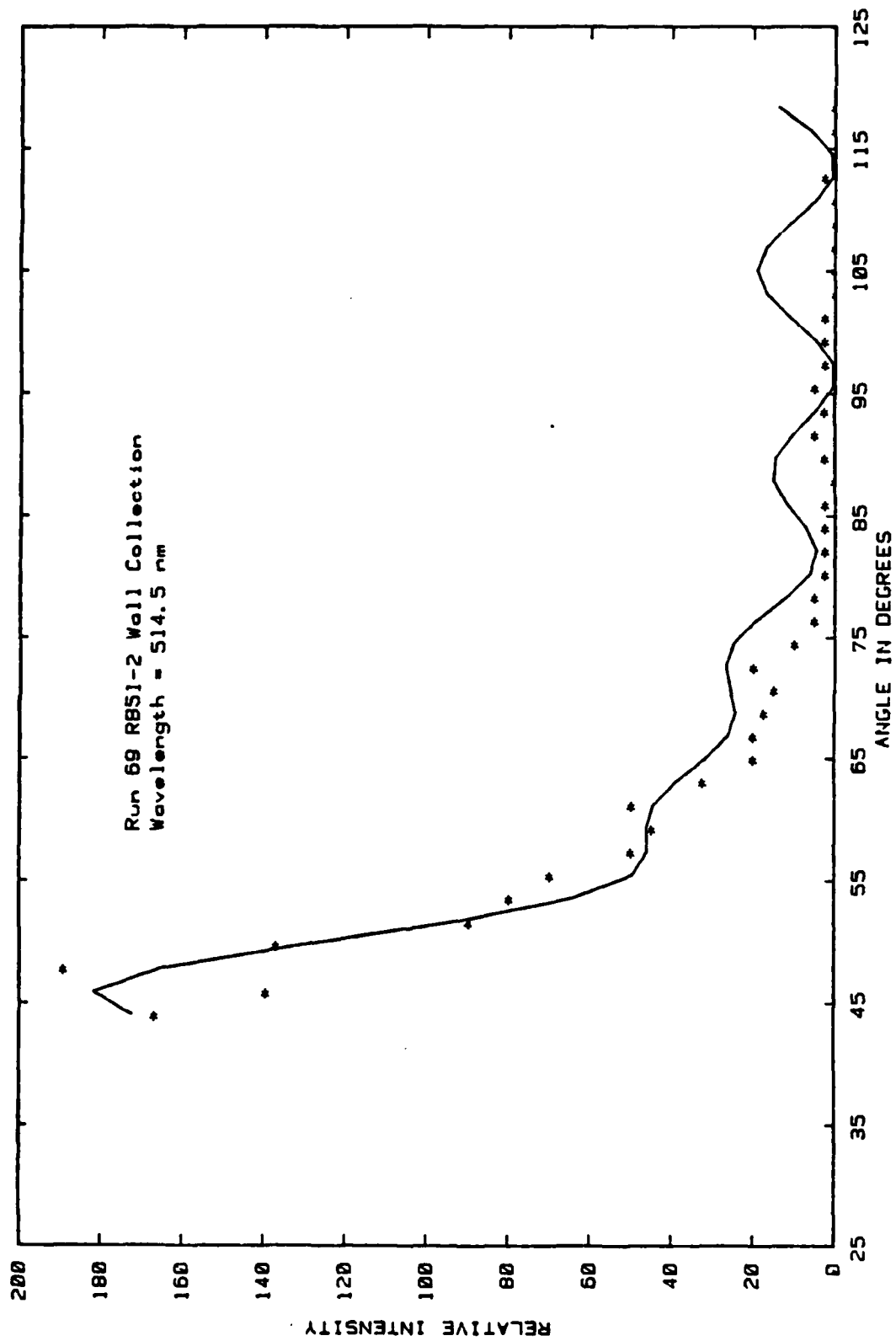


Figure A12. Experimental phase function data (*) for a particle from Run 69 for $\lambda = 514.5$ nm compared with Mie theory (—) for $\alpha = 11.4$ and $m = 1.490 - i0.012$.

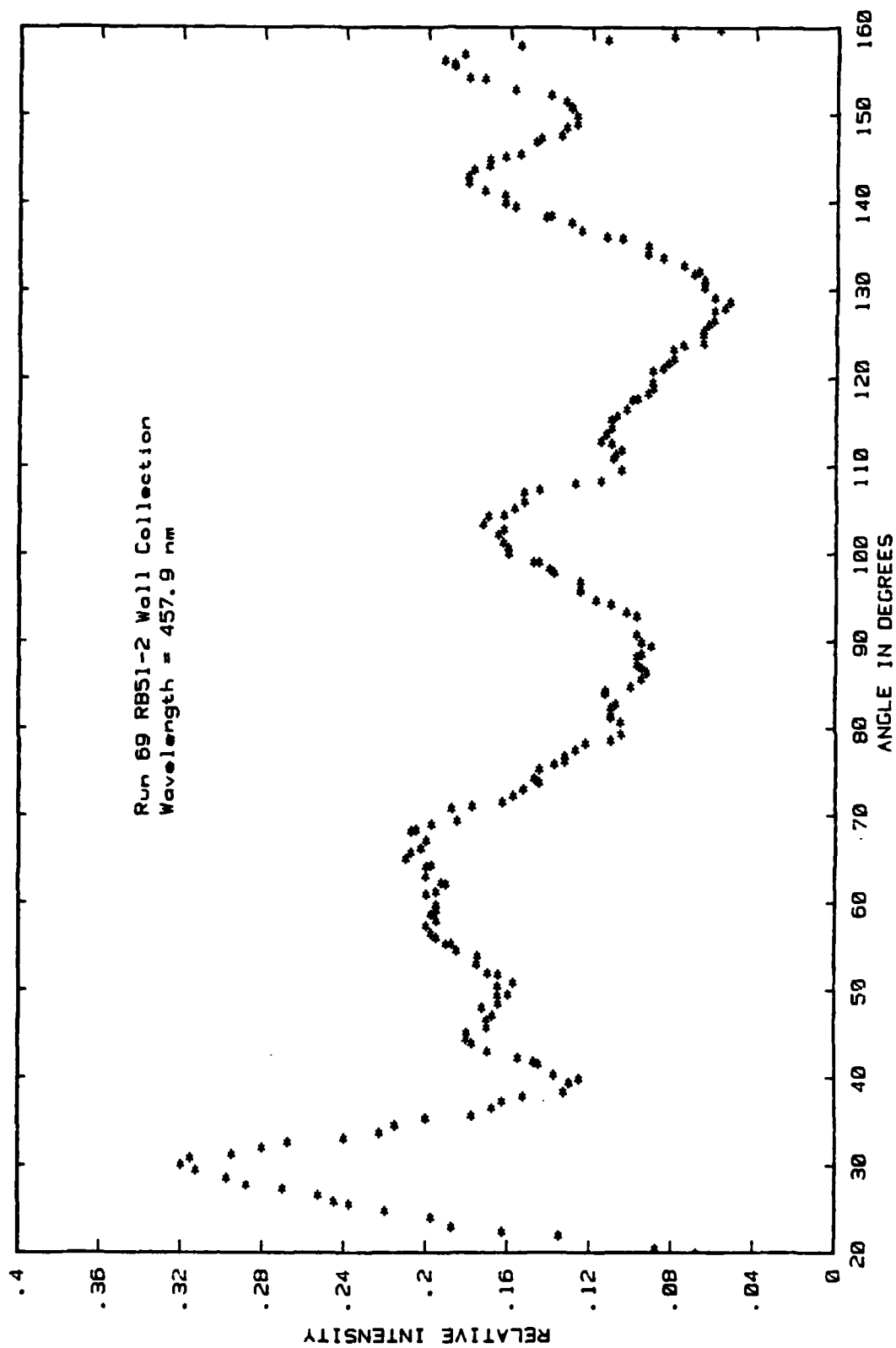


Figure A13. Experimental phase function data (*) for a particle from Run 69 for $\lambda = 457.9$ nm.

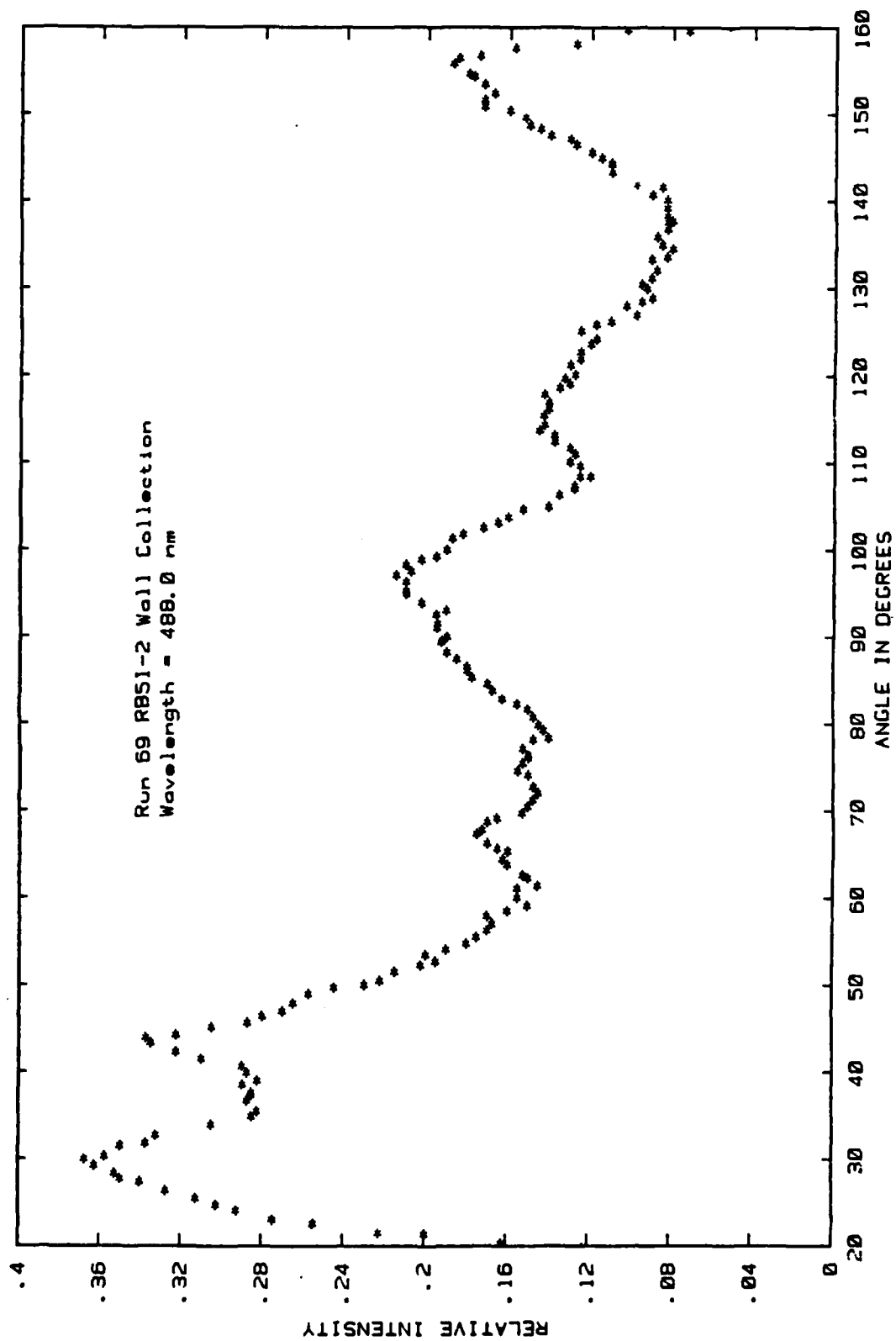


Figure A 14. Experimental phase function data (*) for a particle from Run 69 for $\lambda = 488.0$ nm.

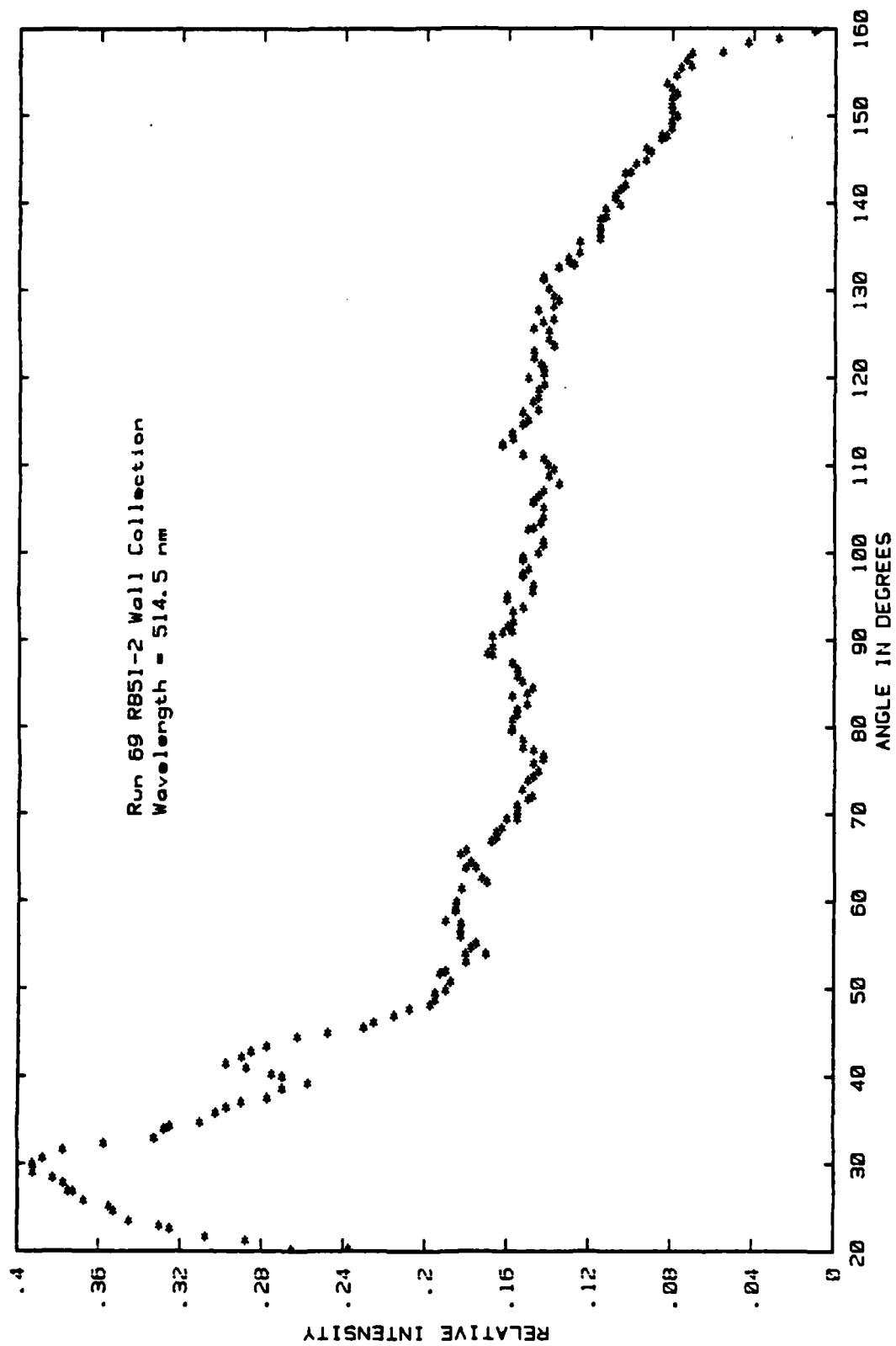


Figure A15. Experimental phase function data (*) for a particle from Run 69 for $\lambda = 514.5$ nm.

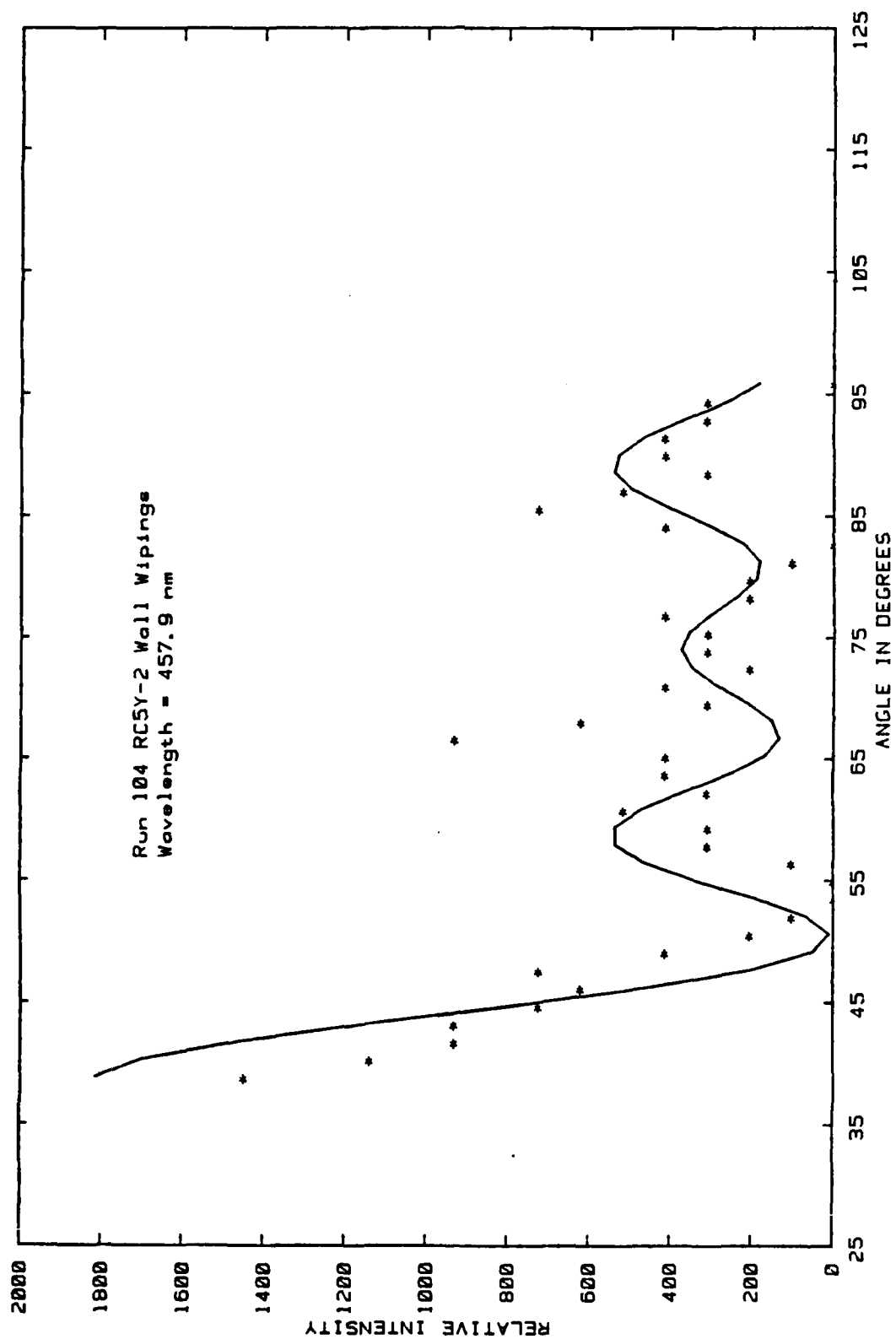


Figure A16. Experimental phase function data (*) for a particle from Run 104 for $\lambda = 457.9$ nm compared with Mie theory (—) for $\alpha = 12.2$ and $m = 1.601 - i0.024$.

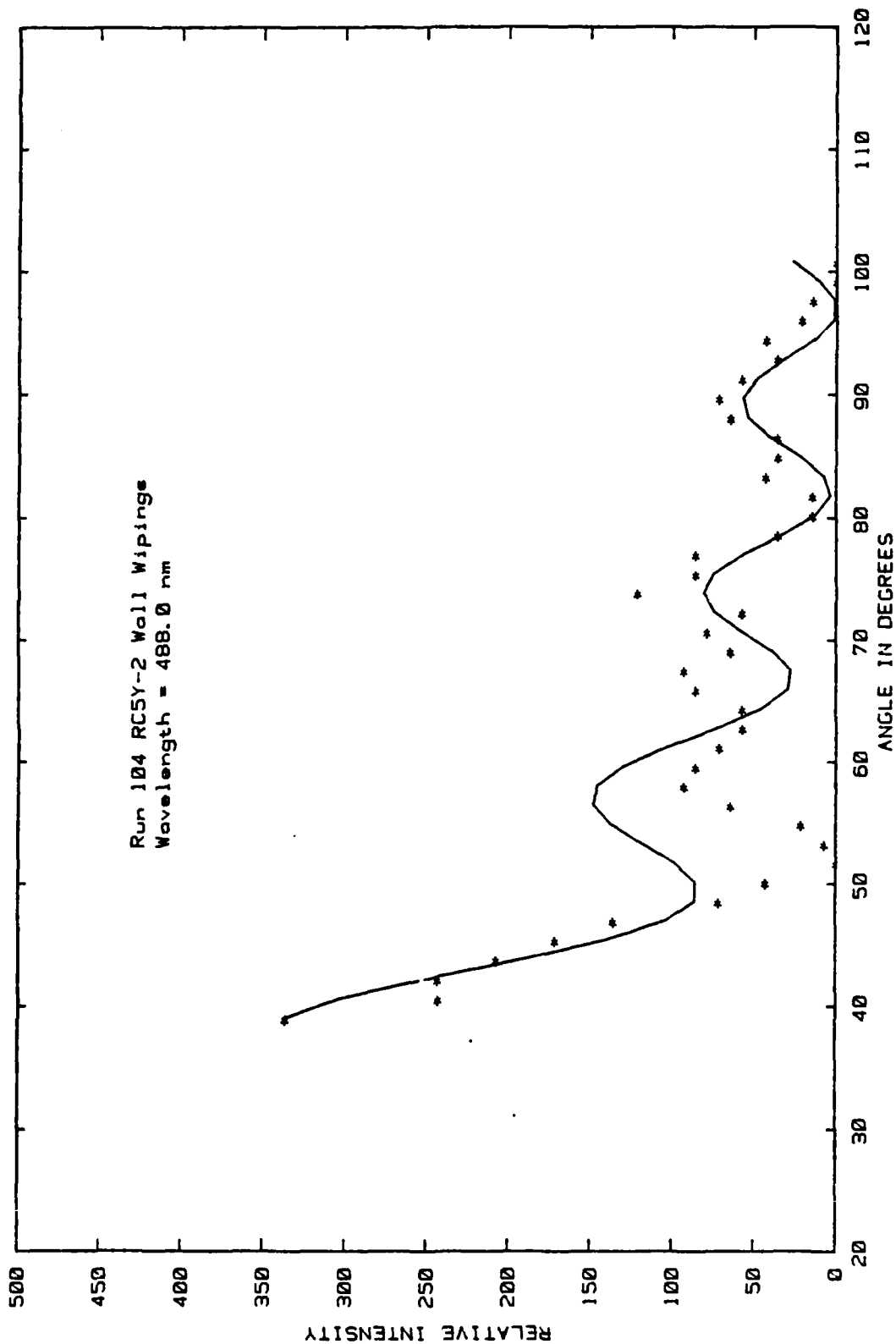


Figure A17. Experimental phase function data (*) for a particle from Run 104 for $\lambda = 488.0$ nm compared with Mie theory (—) for $a = 12.2$ and $m = 1.593 - i0.007$.

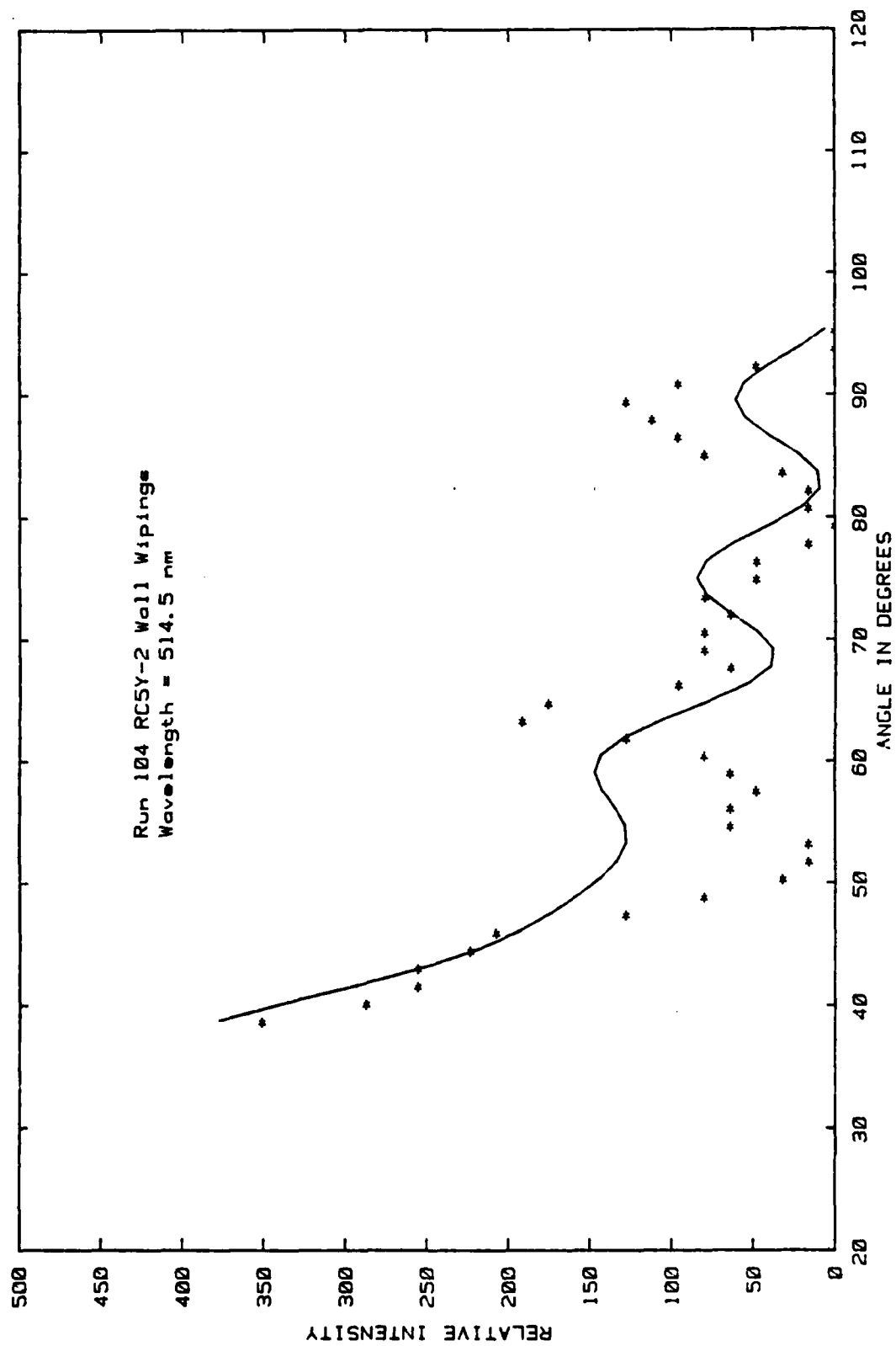


Figure A18. Experimental phase function data (*) for a particle from Run 104 for $\lambda = 514.5$ nm compared with Mie theory (—) for $a = 12.4$ and $m = 1.573 - i0.008$.

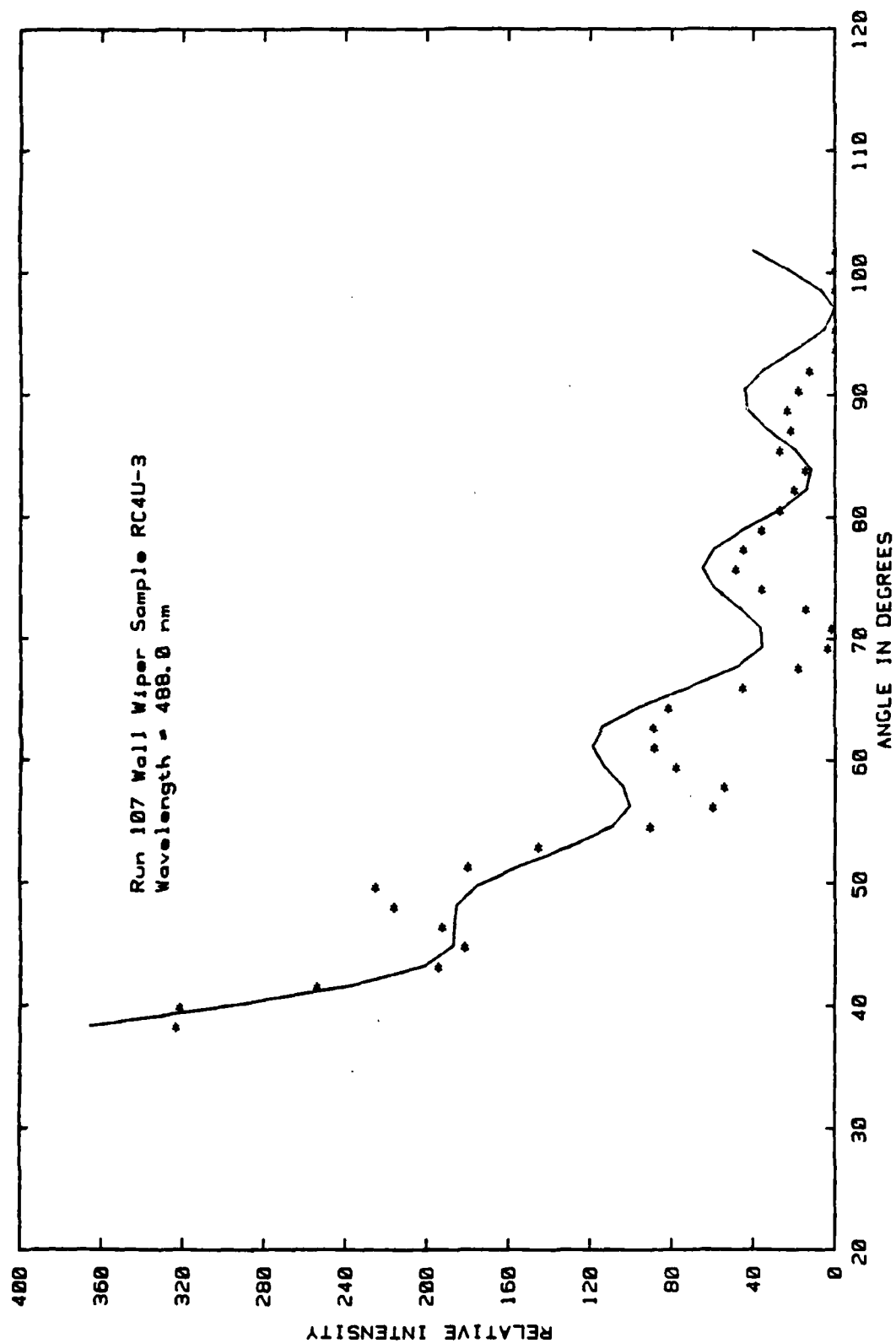


Figure A19. Experimental phase function data (*) for a particle from Run 107 for $\lambda = 488.0$ nm compared with Mie theory (—) for $a = 12.4$ and $m = 1.574 - i0.007$.

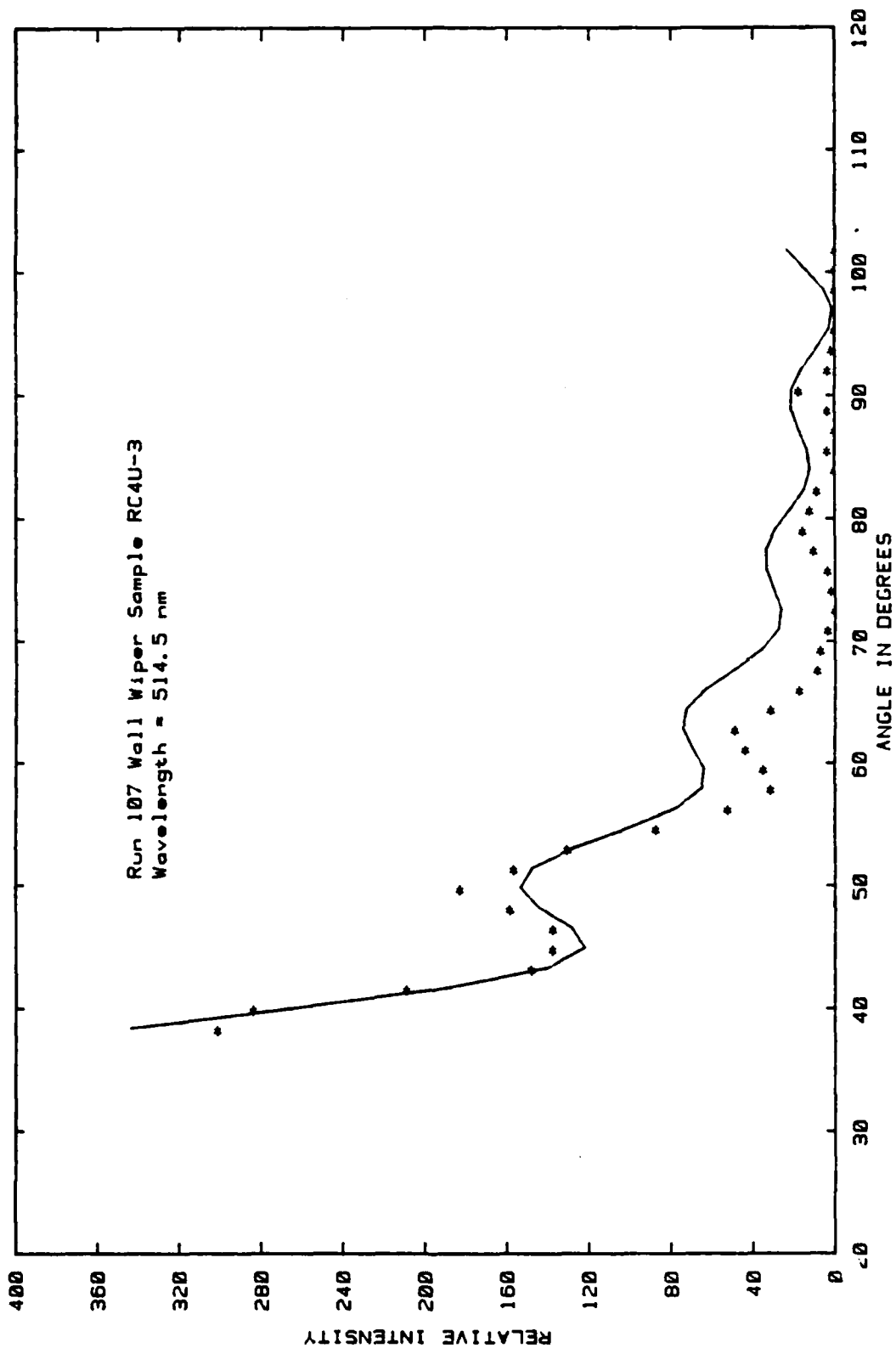


Figure A20. Experimental phase function data (*) for a particle from Run 107 for $\lambda = 514.5$ nm compared with Mie theory (—) for $a = 12.5$ and $m = 1.559 - i0.005$.

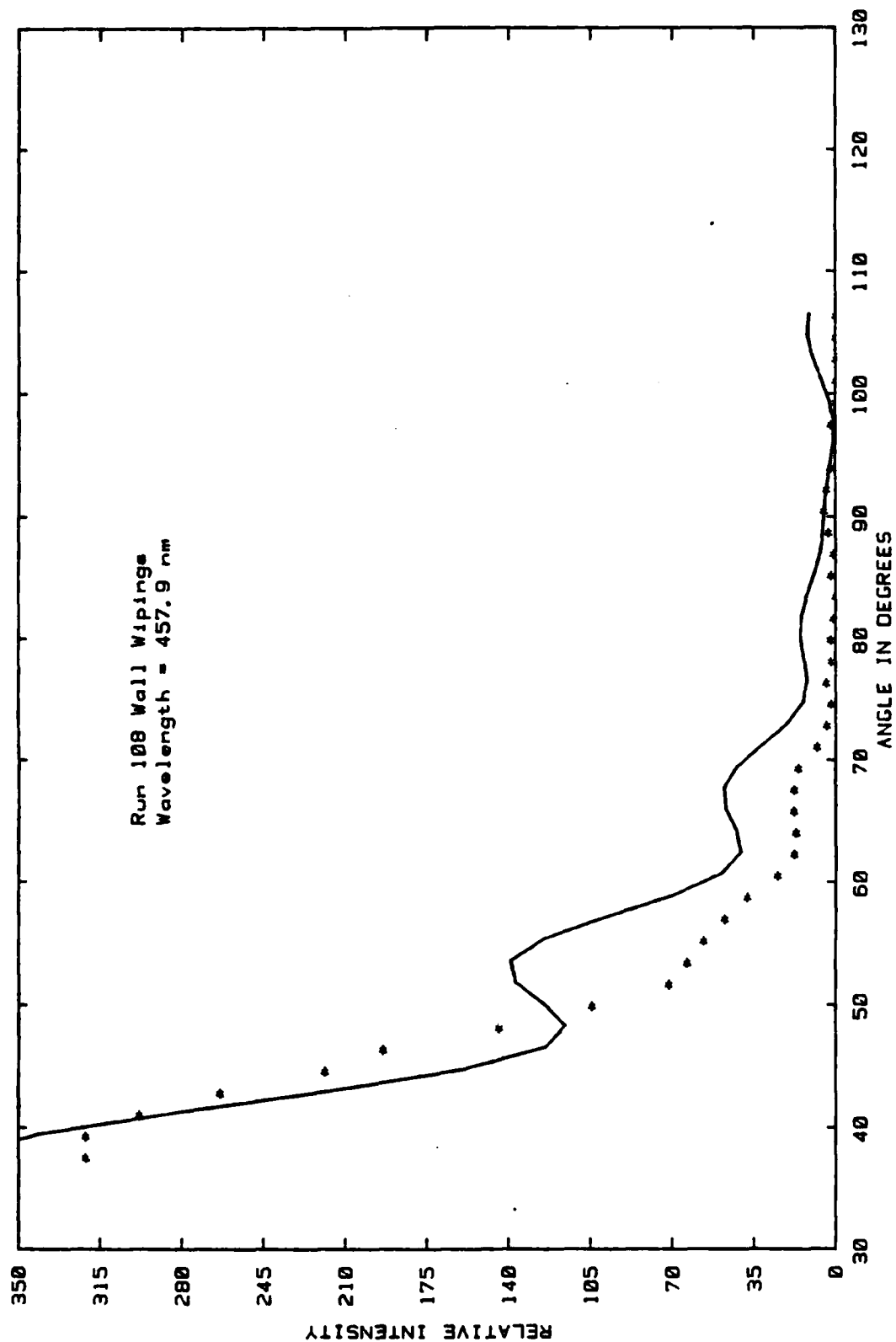


Figure A21. Experimental phase function data (*) for a particle from Run 108 for $\lambda = 457.9$ nm compares with Mie theory (—) for $a = 12.8$ and $m = 1.529 - i0.005$.

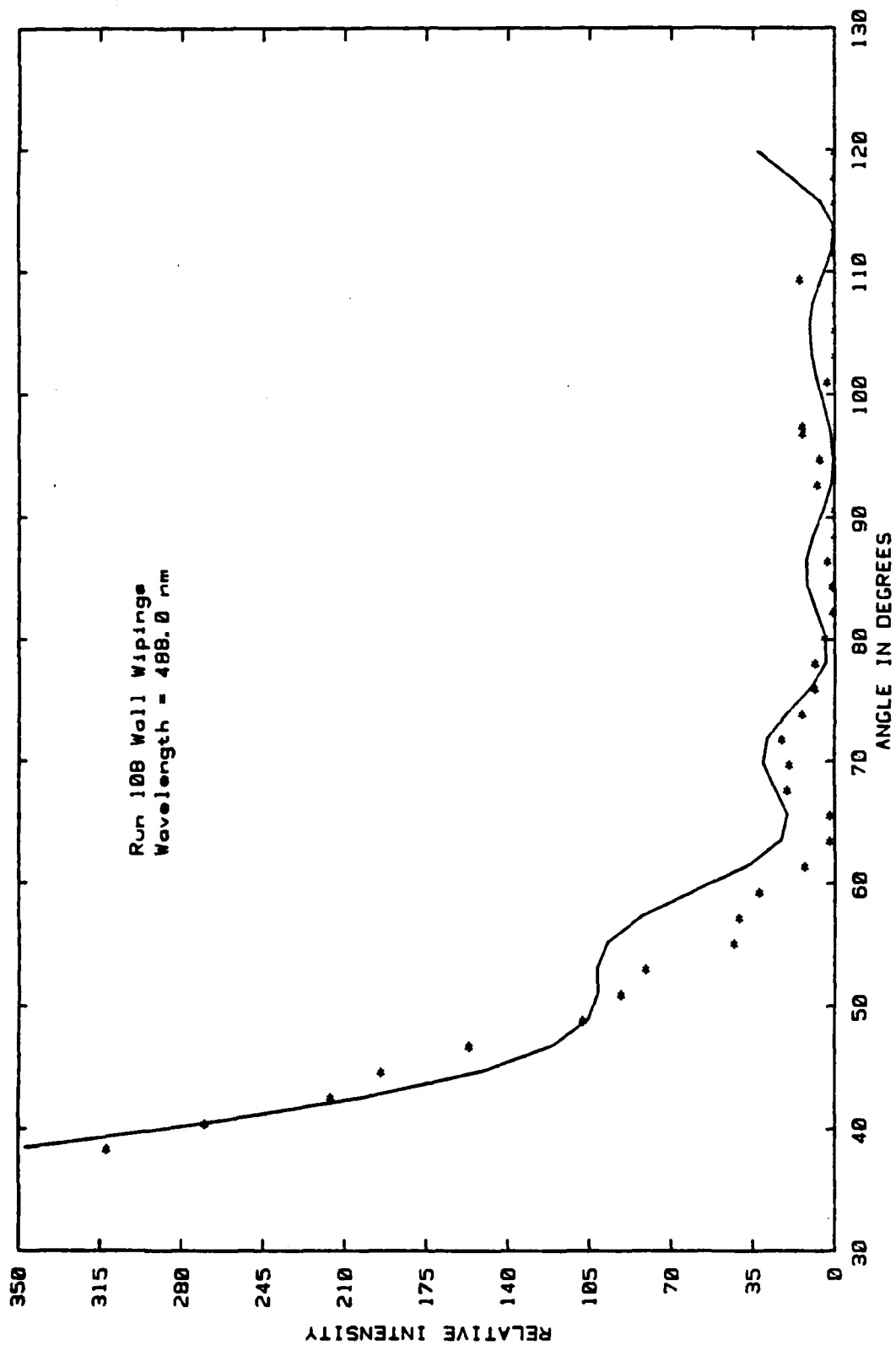


Figure A22. Experimental phase function data (*) for a particle from Run 108 for $\lambda = 488.0$ nm compared with Mie theory (—) for $\alpha = 12.9$ and $m = 1.510 - i0.005$.

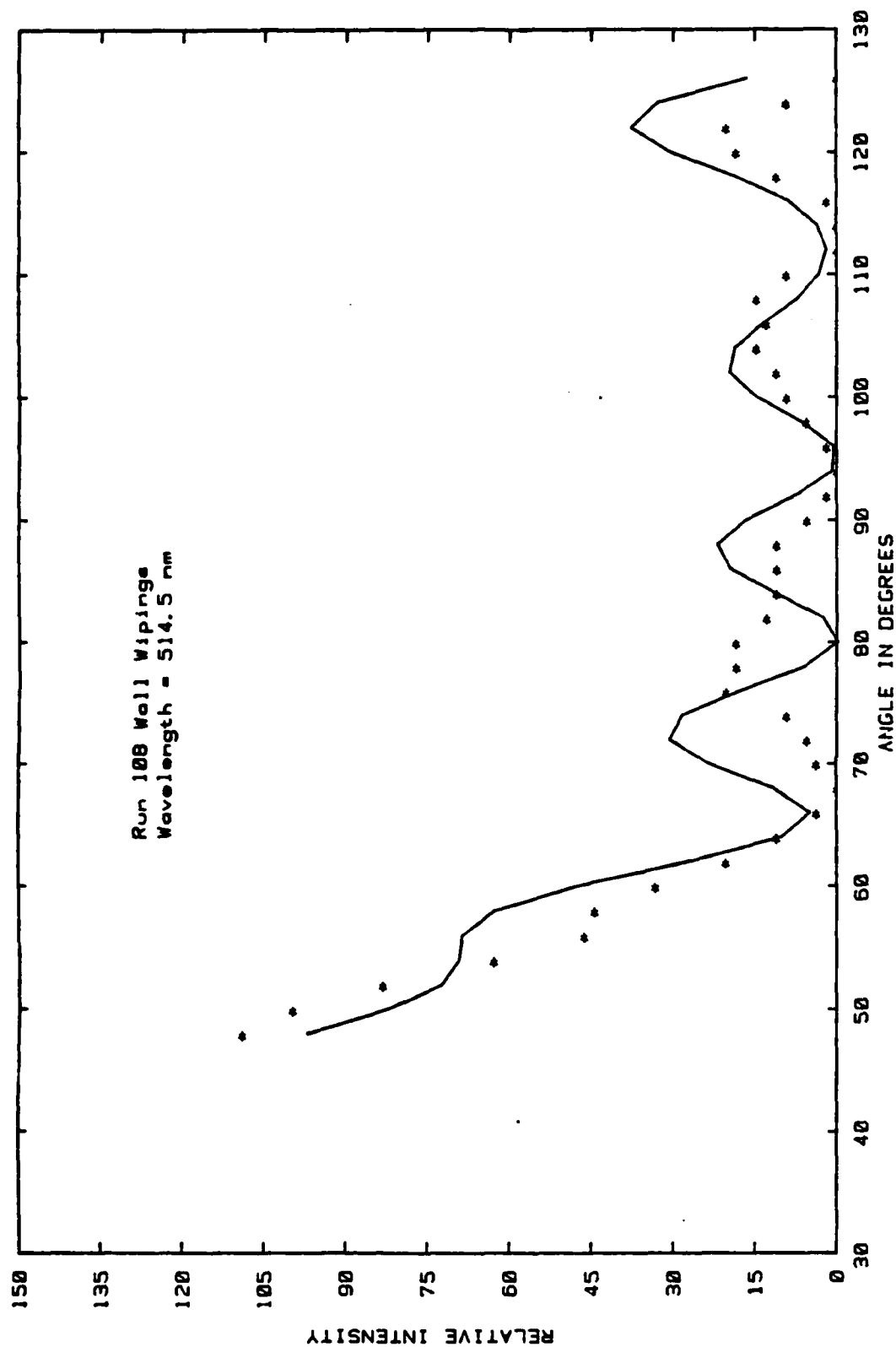


Figure A23. Experimental phase function data (*) for a particle from Run 108 for $\lambda = 514.5$ nm compared with Mie theory (—) for $a = 13.1$ and $m = 1.481 - i0.007$.

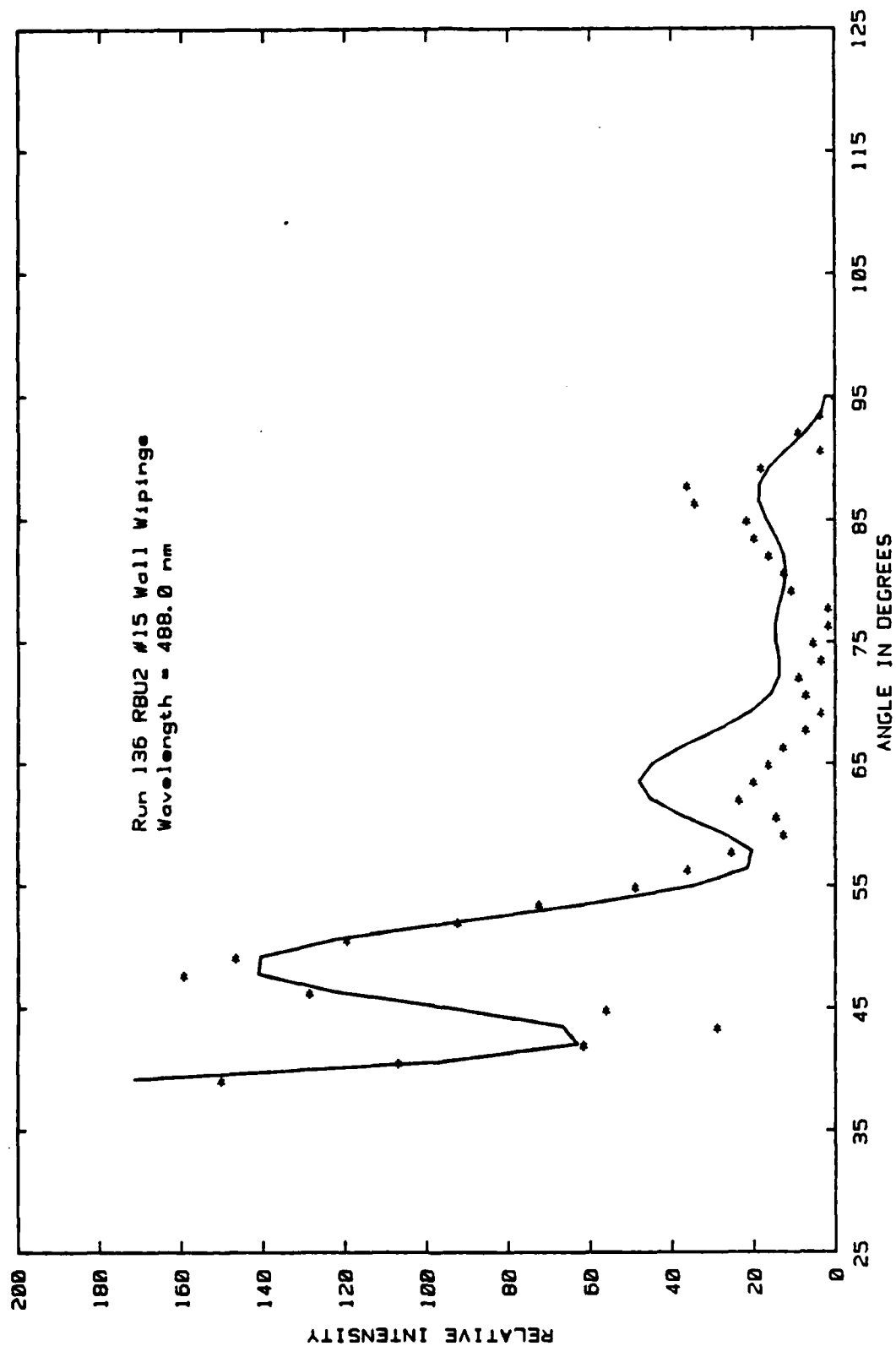


Figure A24. Experimental phase function data (*) for a particle from Run 136 for $\lambda = 488.0$ nm compared with Mie theory (—) for $\alpha = 12.4$ and $m = 1.582 - i0.002$.

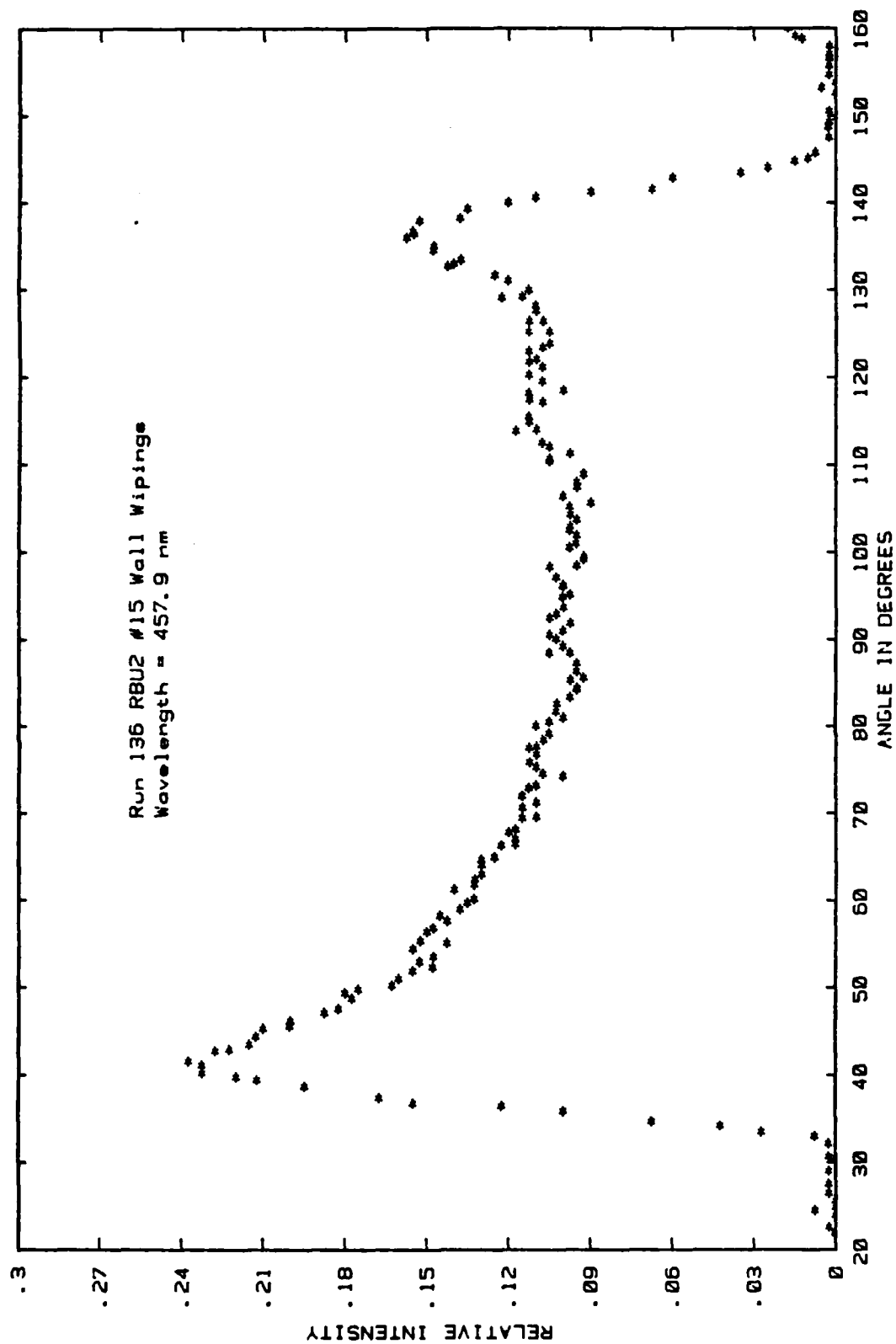


Figure A25. Experimental phase function data (*) for a particle from Run 136 for $\lambda = 457.9$ nm.

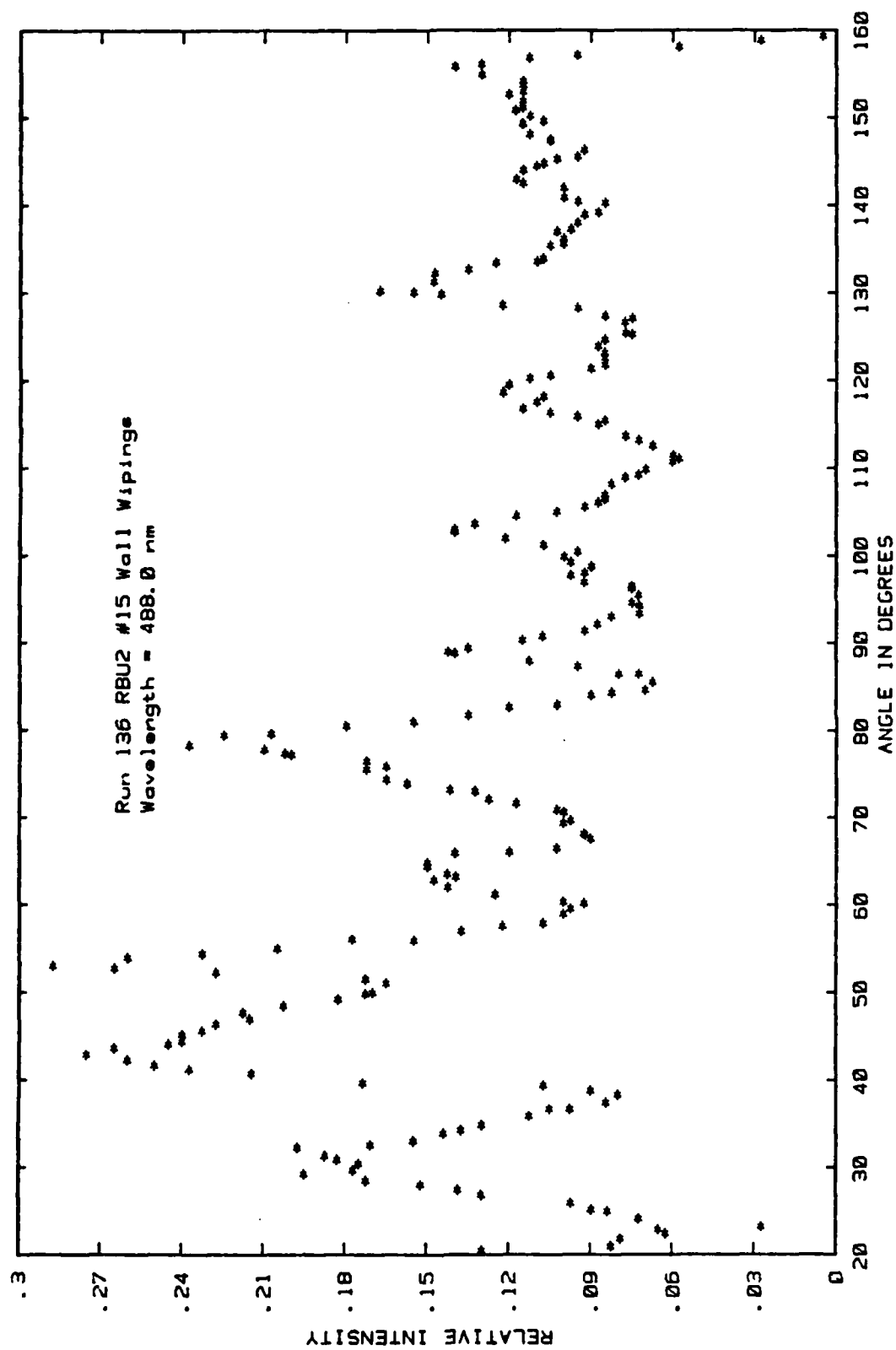


Figure A26. Experimental phase function data (*) for a particle from Run 136 for $\lambda = 488.0$ nm.

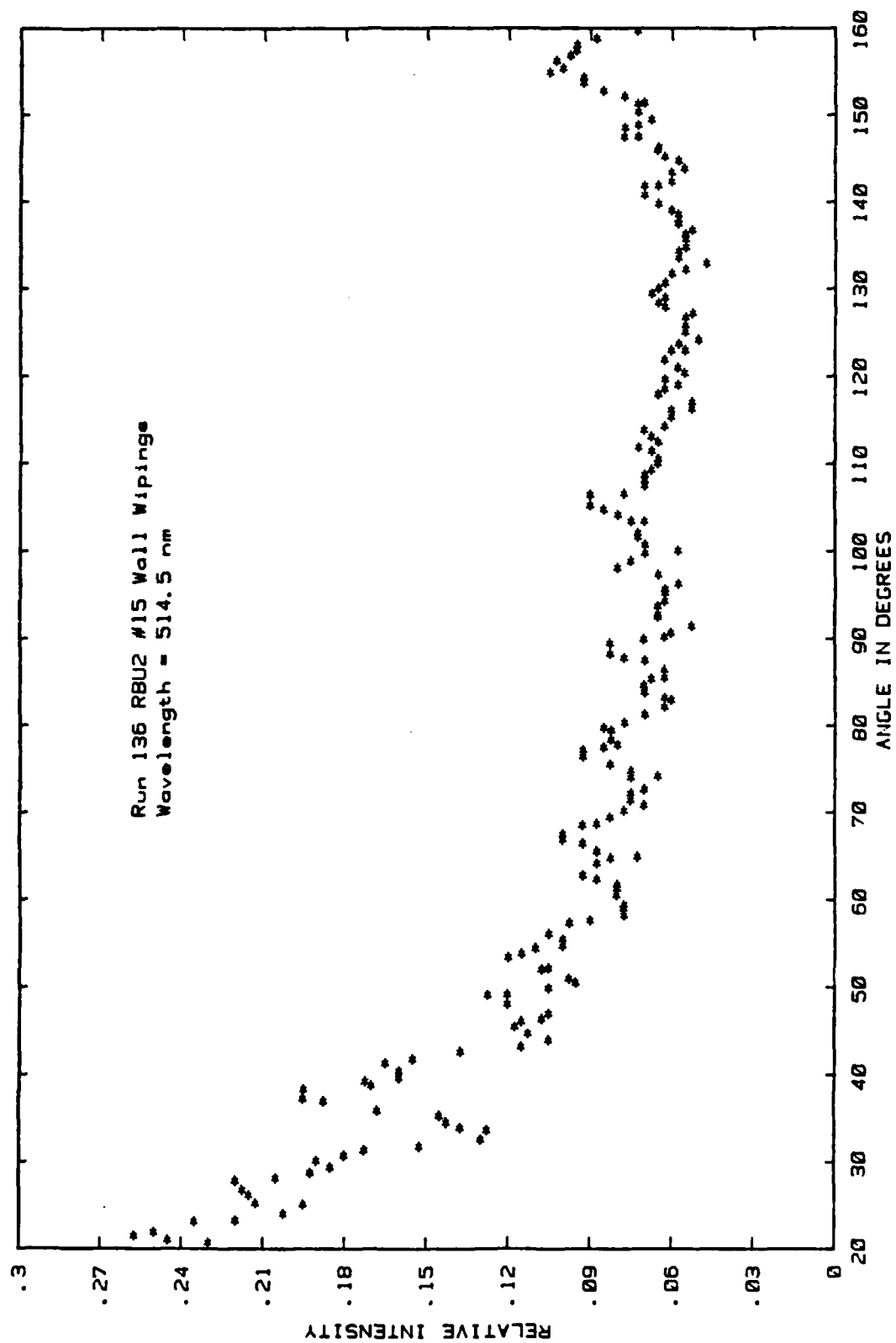


Figure A27. Experimental phase function data (*) for a particle from Run 136 for $\lambda = 514.5$ nm.

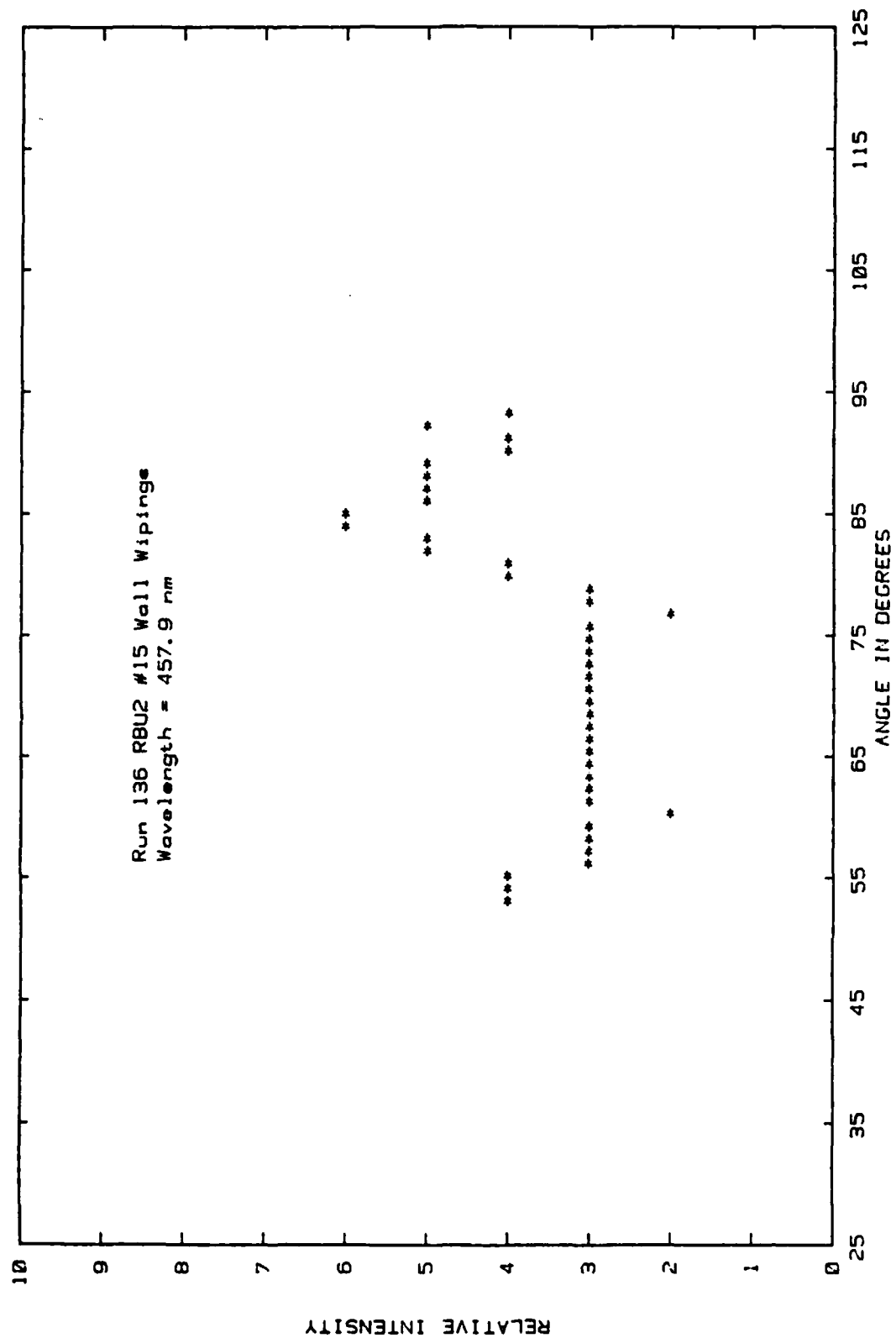


Figure A28. Experimental phase function data (*) for a particle from Run 136 for $\lambda = 457.9$ nm.

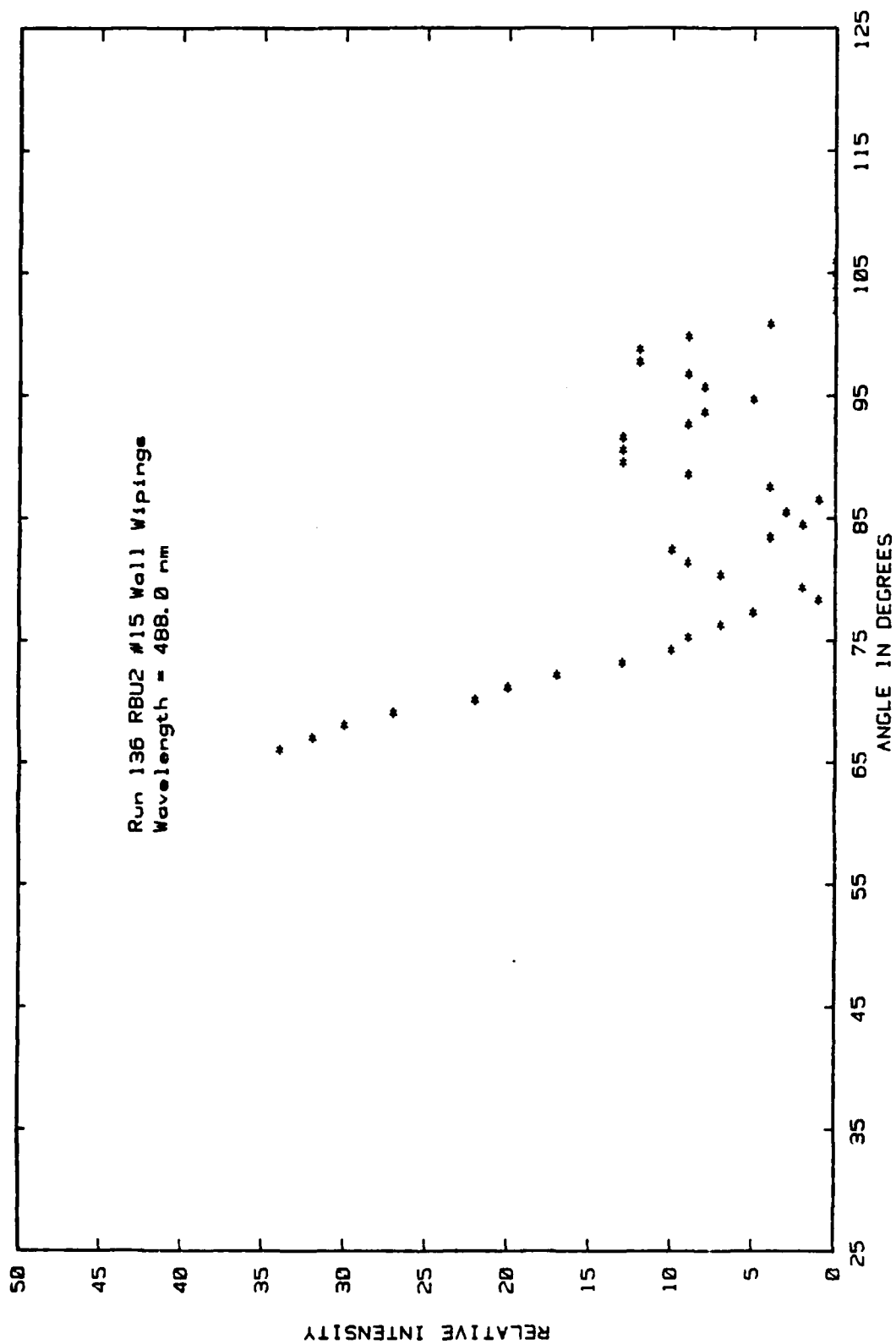


Figure A29. Experimental phase function data (*) for a particle from Run 136 for $\lambda = 488.0$ nm.

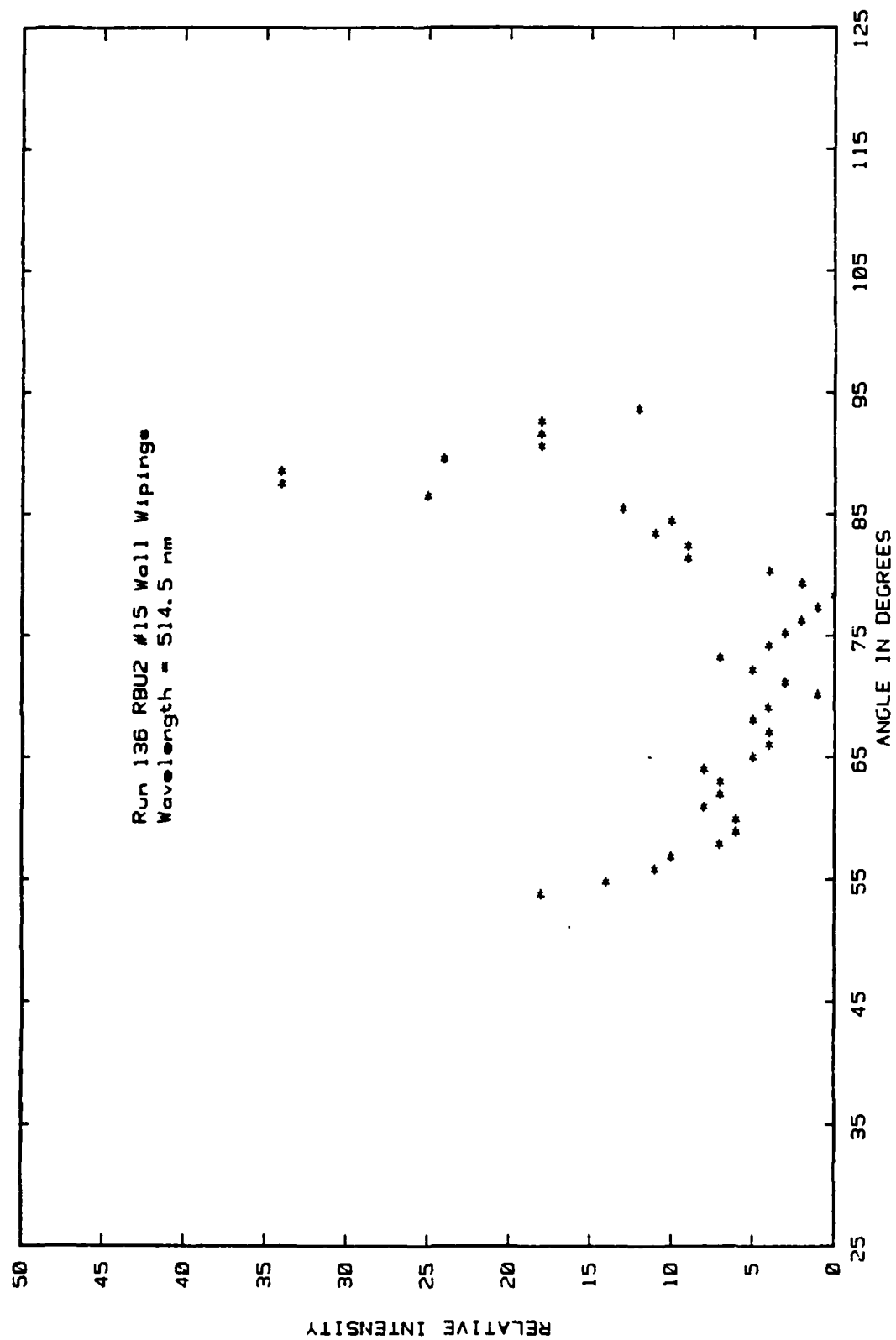


Figure A30. Experimental phase function data (*) for a particle from Run 136 for $\lambda = 514.5$ nm.

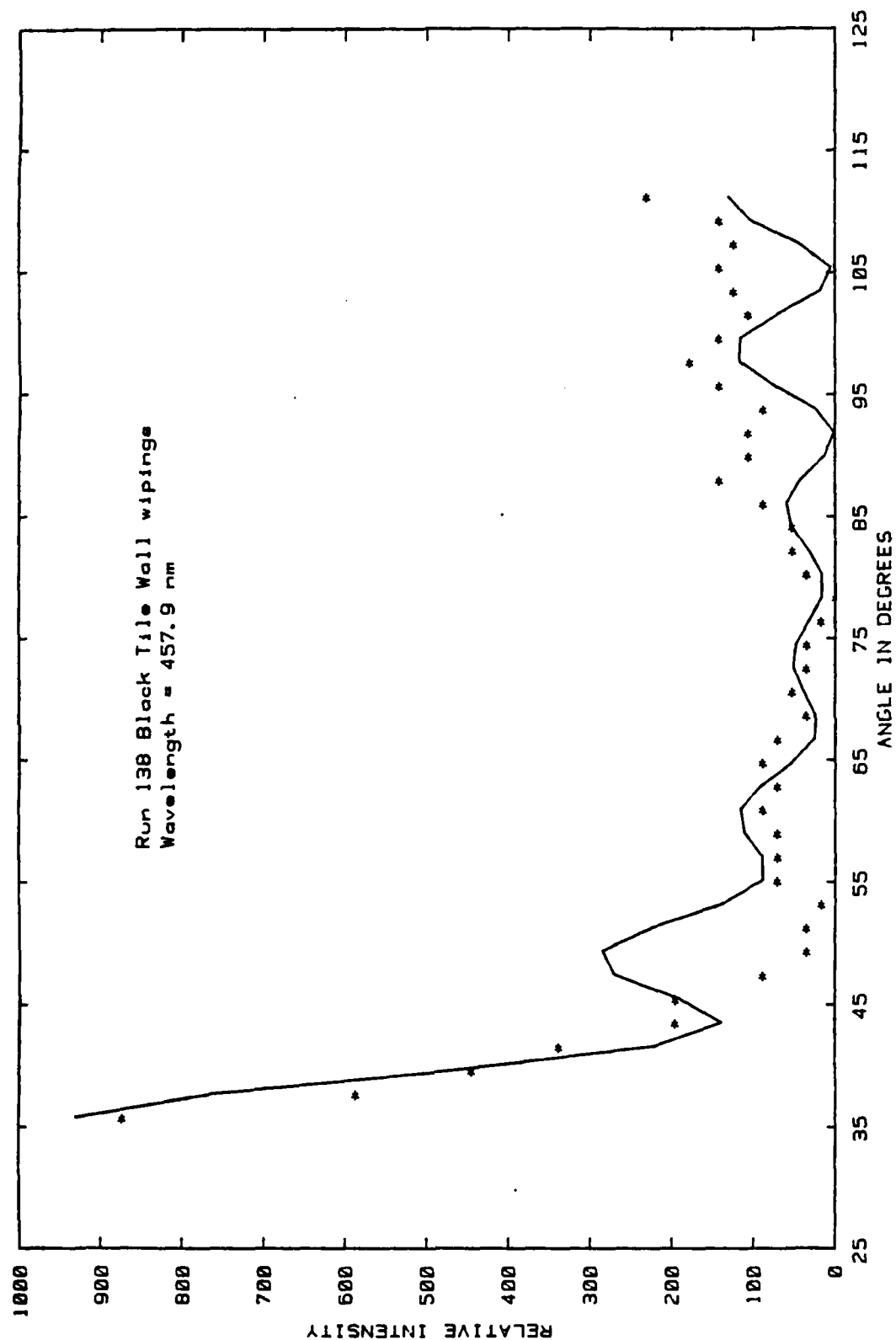


Figure A31. Experimental phase function data (*) for a particle from Run 138 for $\lambda = 457.9$ nm compared with Mie theory (—) for $a = 14.1$ and $m = 1.723 - i0.007$.

AD-A166 460

OPTICAL PROPERTIES OF BLOW-OFF PARTICULATES(U)

2/2

INSTITUTE OF PAPER CHEMISTRY APPLTTON WIS

E J DAVIS ET AL 29 FEB 84 DNA-RR-84-69

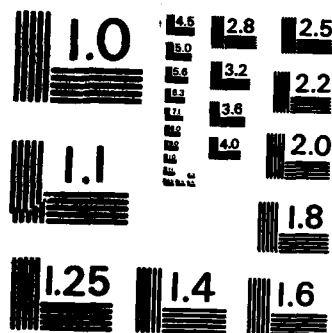
UNCLASSIFIED

DNA011-82-C-0224

F/G 20/6

NL





MICROCOPY RESOLUTION TEST CHART
NATIONAL BUREAU OF STANDARDS-1963-A

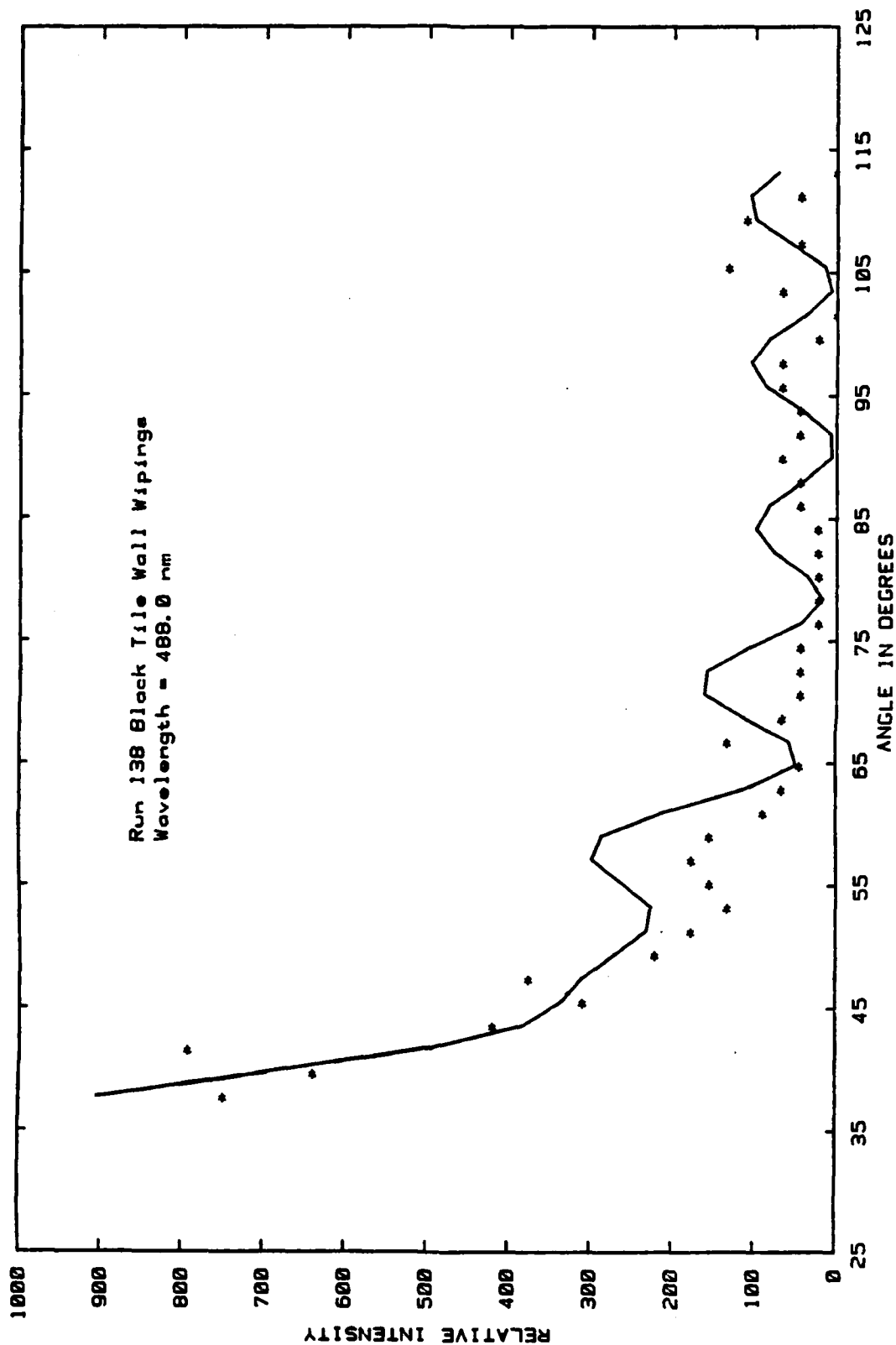


Figure A32. Experimental phase function data (*) for a particle from Run 138 for $\lambda = 488.0$ nm compared with Mie theory (—) for $\alpha = 14.6$ and $m = 1.674 - i0.010$.

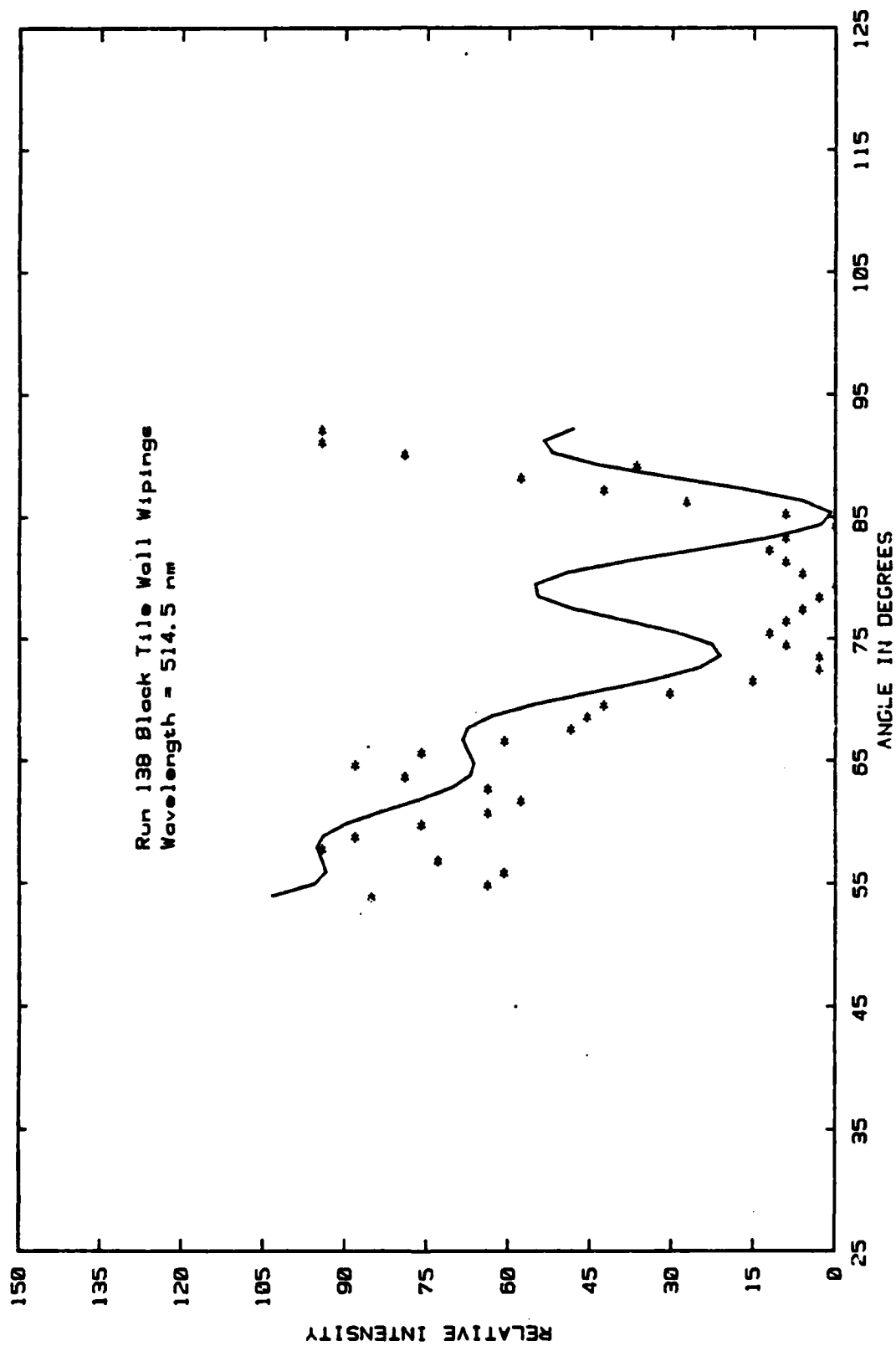


Figure A33. Experimental phase function data (*) for a particle from Run 138 for $\lambda = 514.5$ nm compared with Mie theory (—) for $a = 15.6$ and $m = 1.613 - i0.0$.

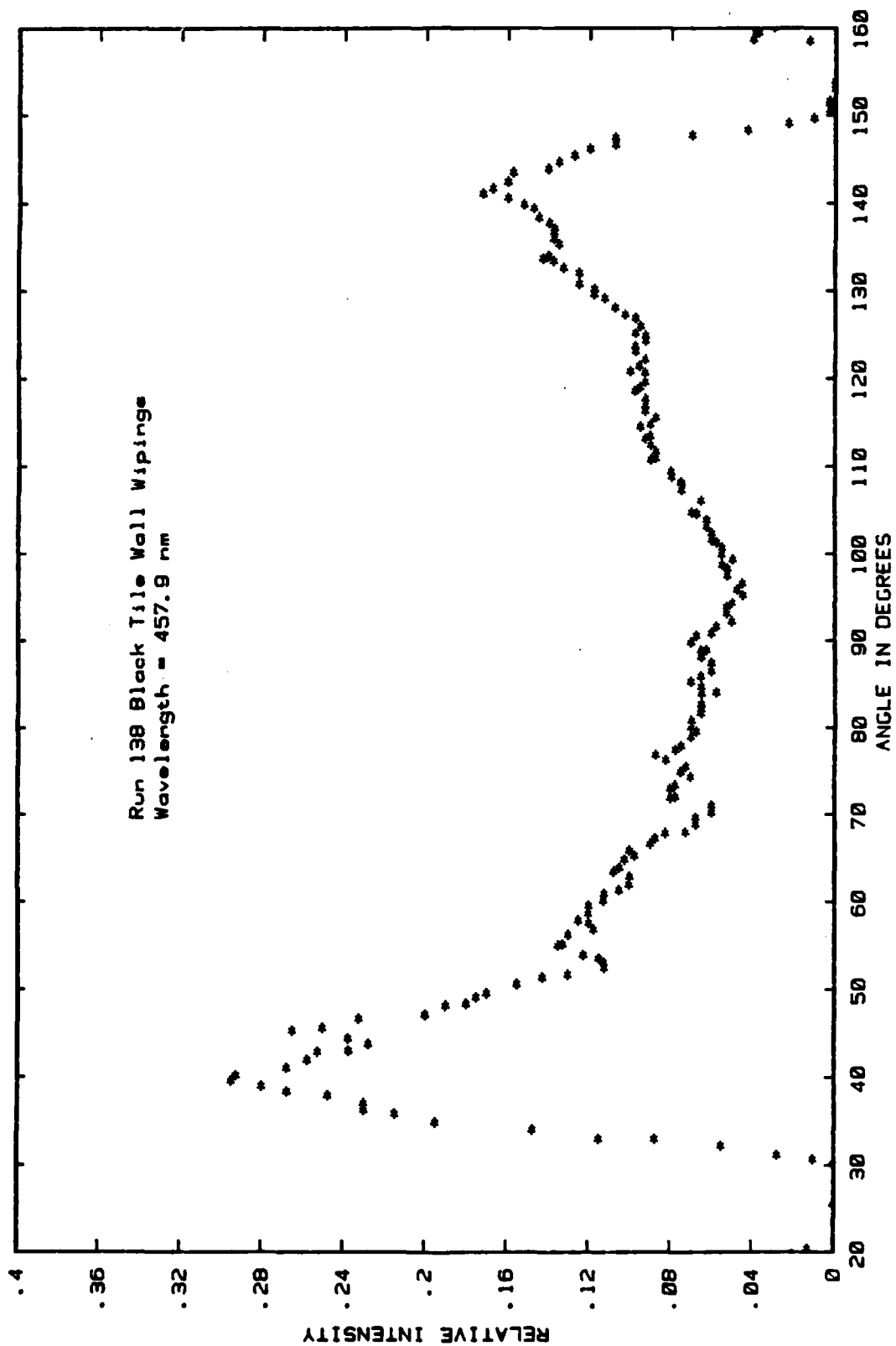


Figure A34. Experimental phase function data (*) for a particle from Run 138 for $\lambda = 457.9$ nm.

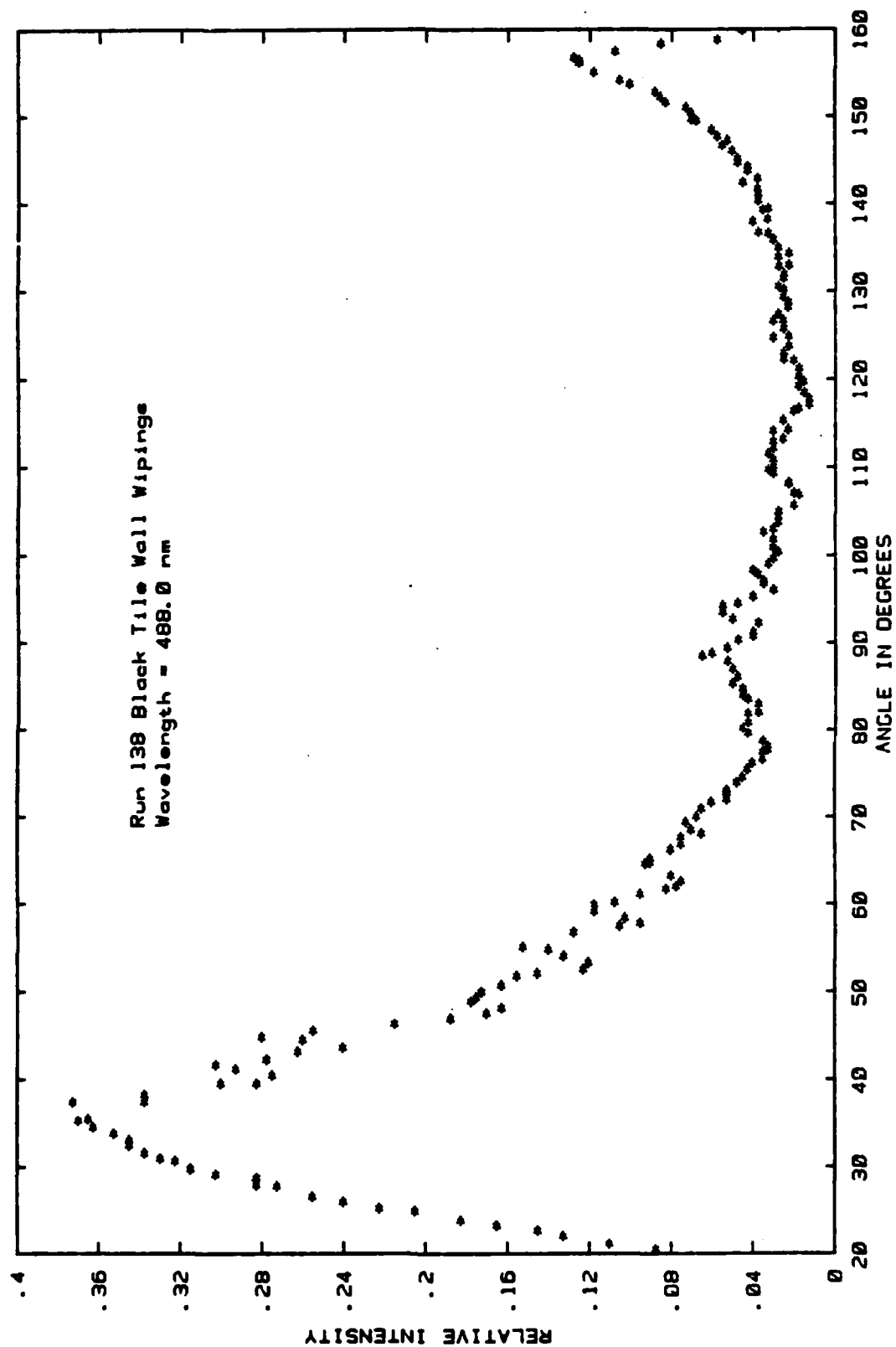


Figure A35. Experimental phase function data (*) for a particle from Run 138 for $\lambda = 488.0$ nm.

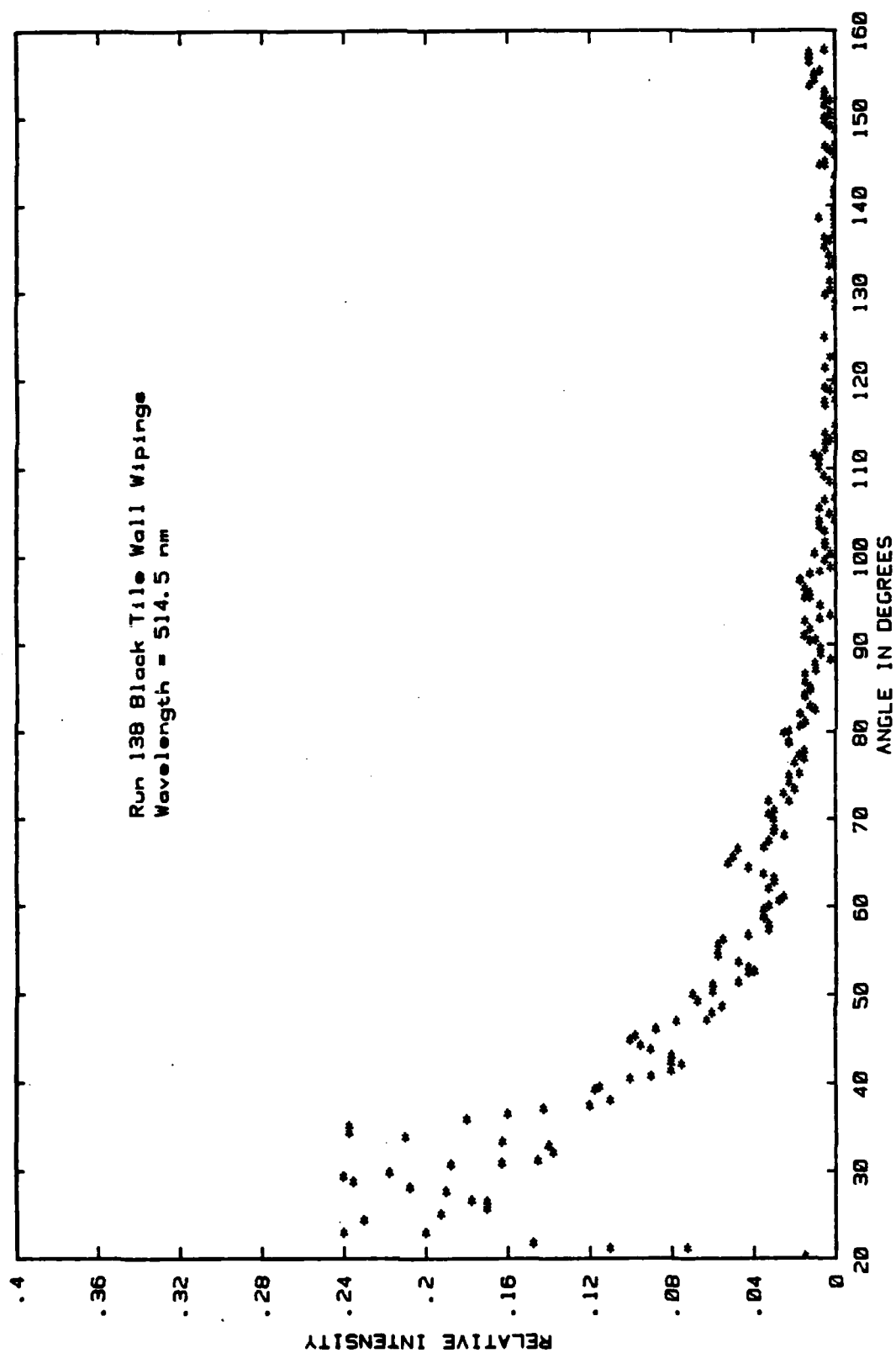


Figure A36. Experimental phase function data (*) for a particle from Run 138 for $\lambda = 514.5$ nm.

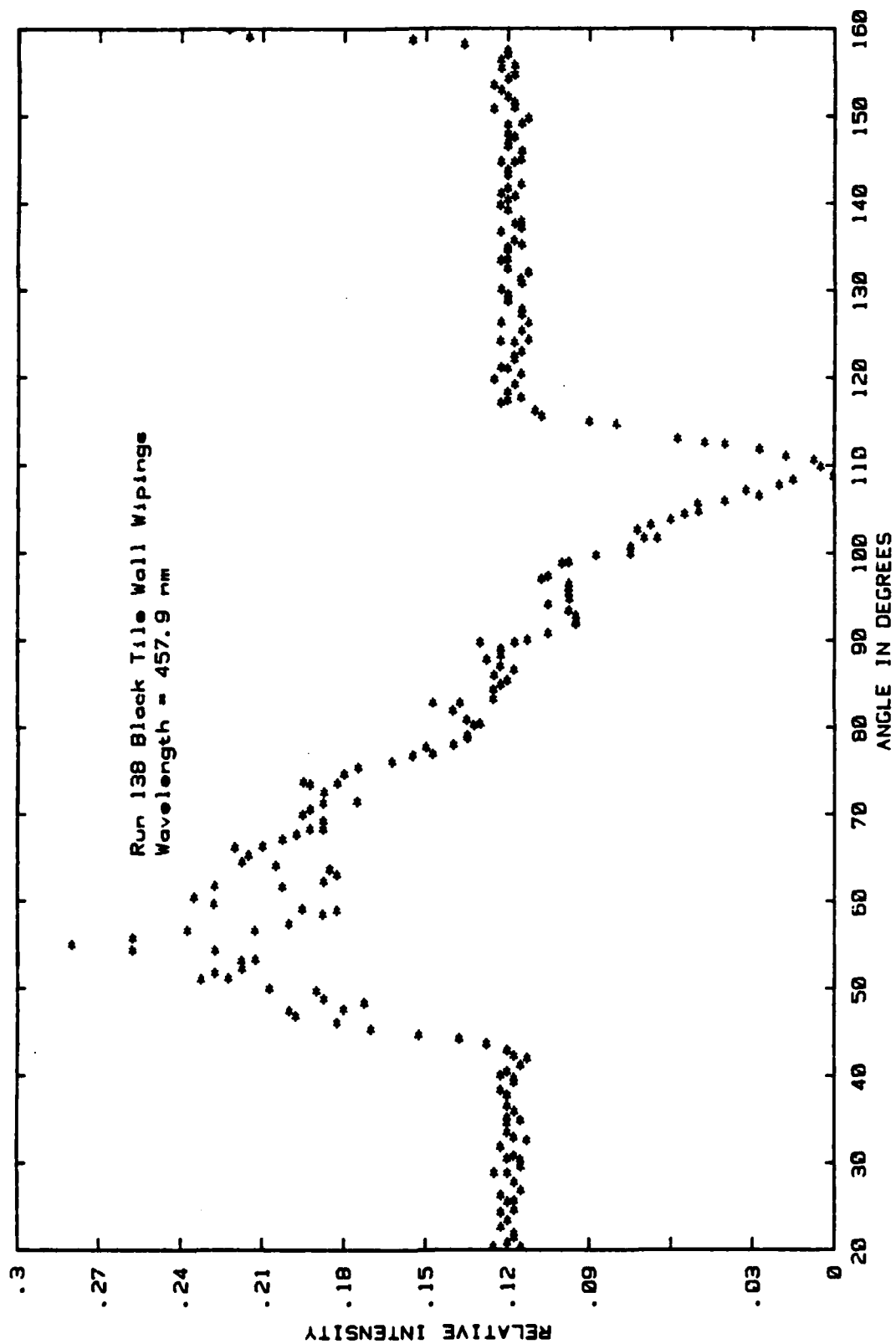


Figure A37. Experimental phase function data (*) for a particle from Run 138 for $\lambda = 457.9$ nm.

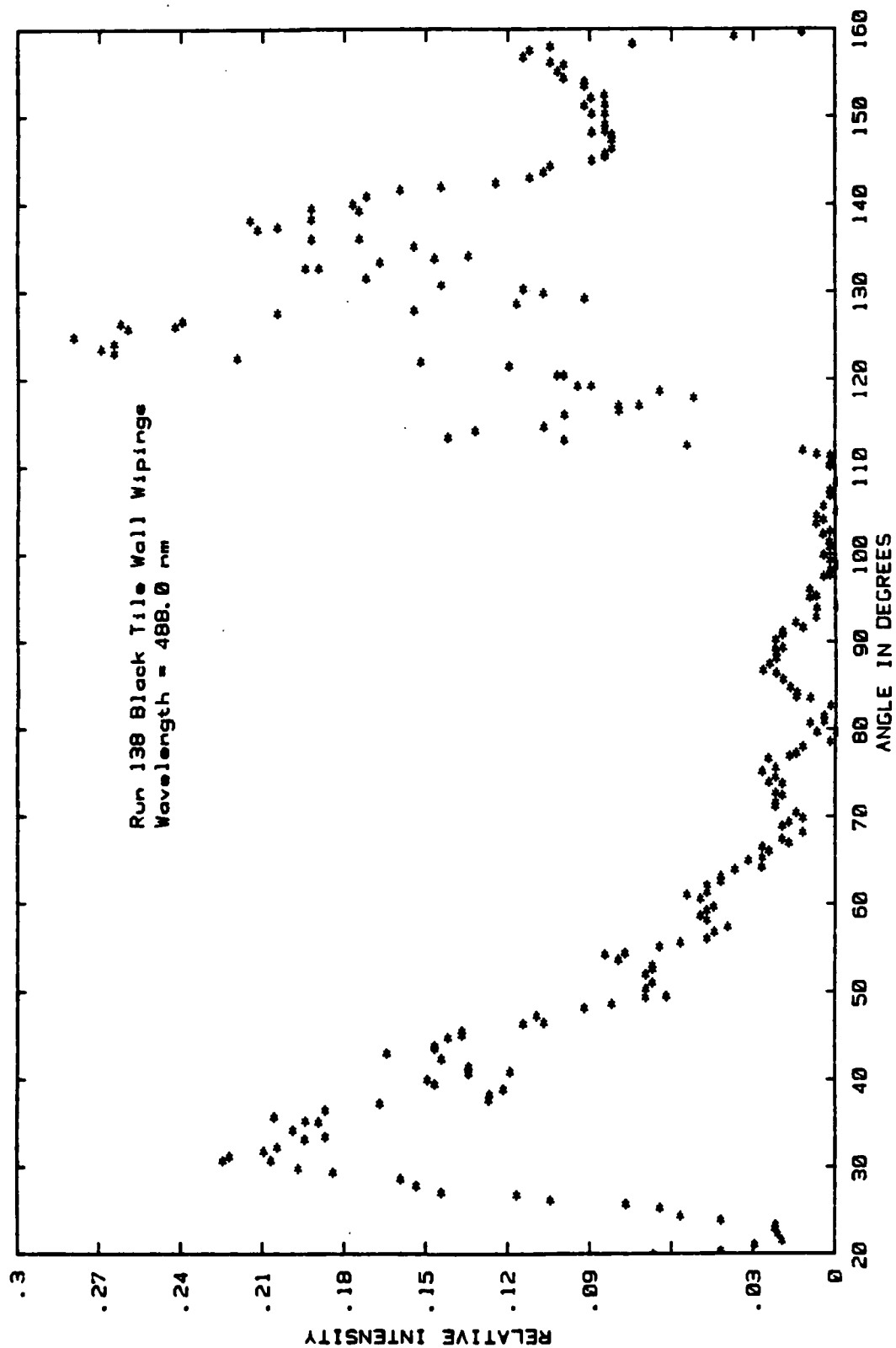


Figure A38. Experimental phase function data (*) for a particle from Run 138 for $\lambda = 488.0$ nm.

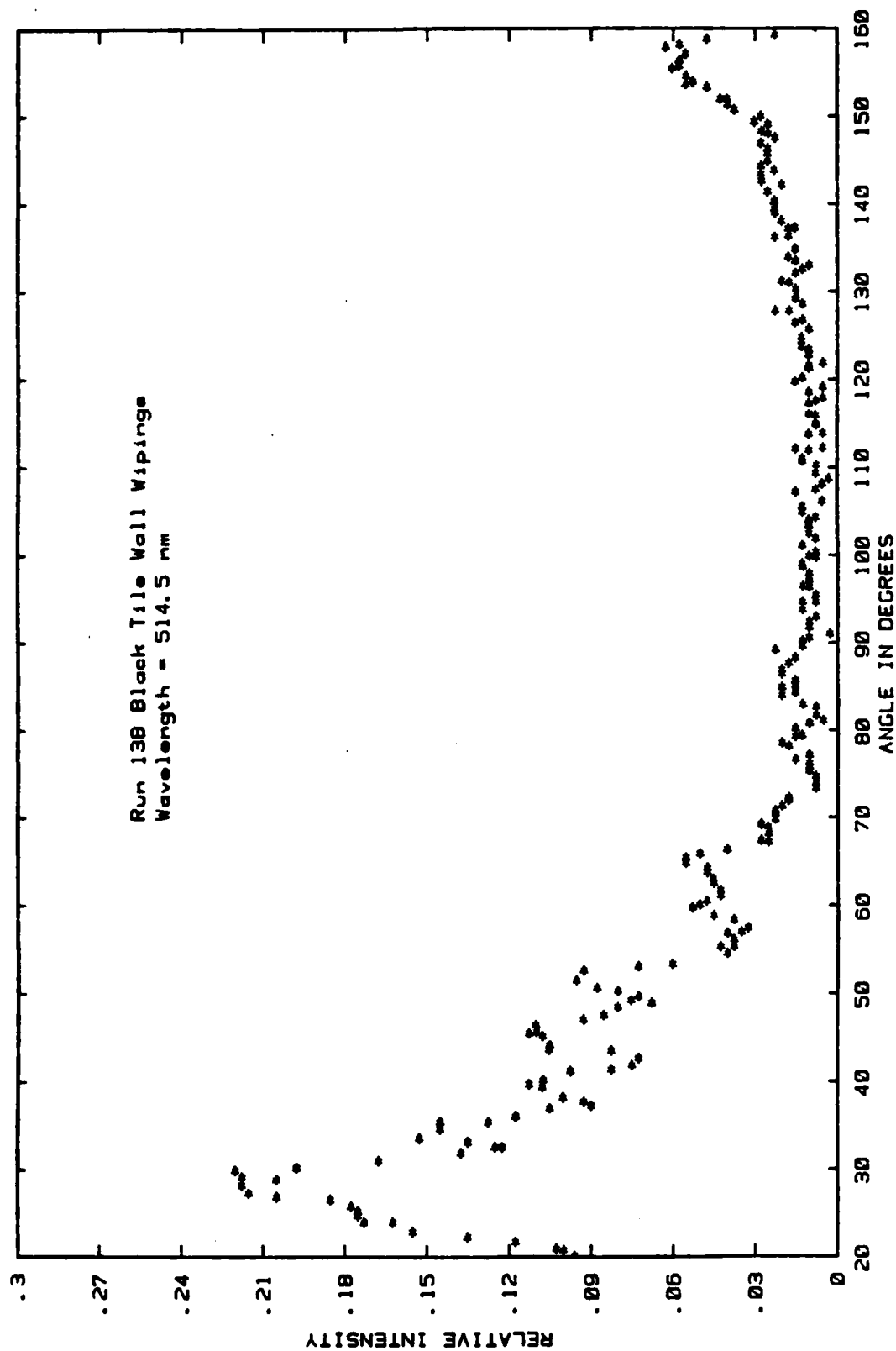


Figure A39. Experimental phase function data (*) for a particle from Run 138 for $\lambda = 514.5$ nm.

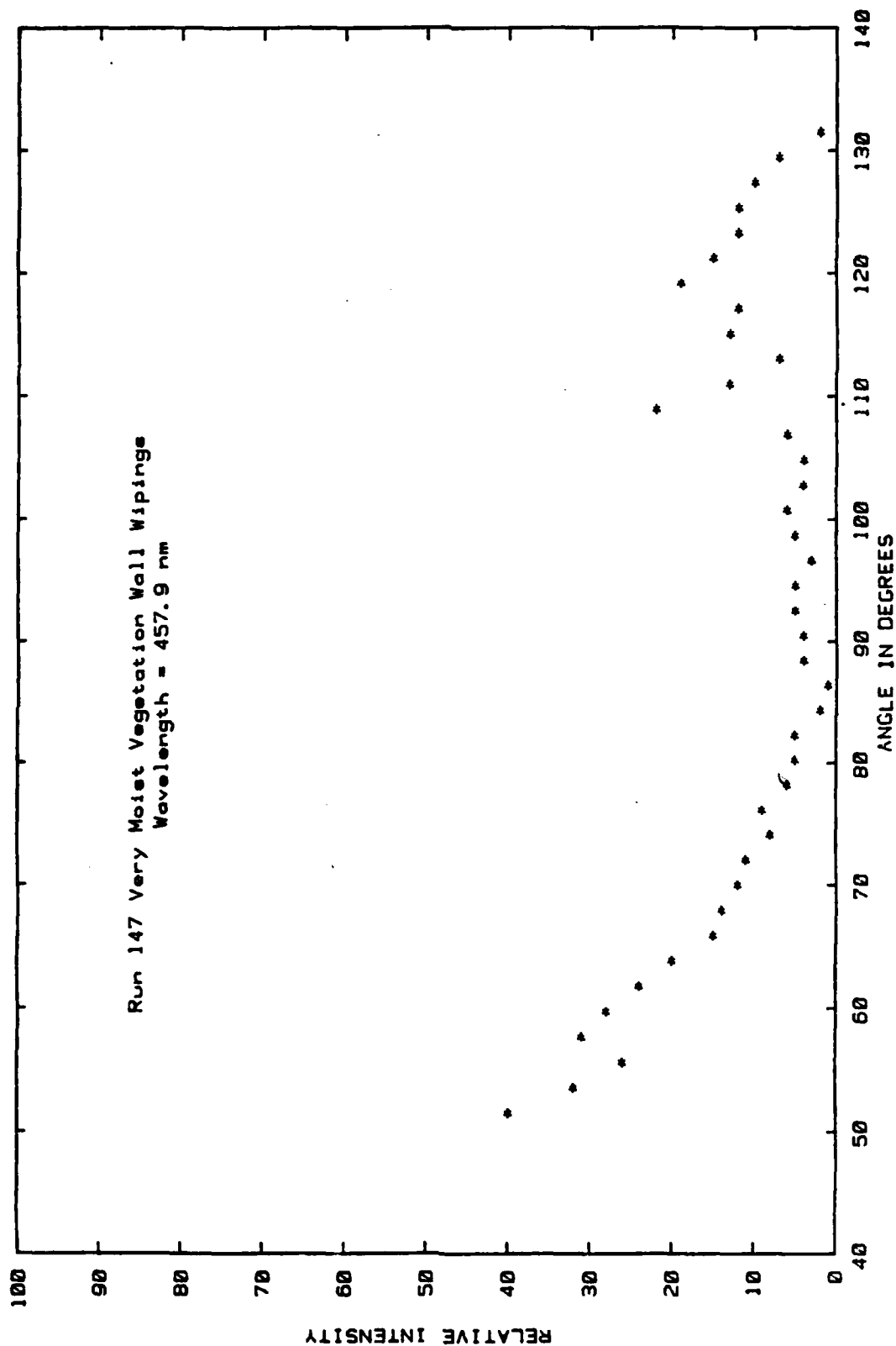


Figure A40. Experimental phase function data (*) for a particle from Run 147 for $\lambda = 457.9$ nm.

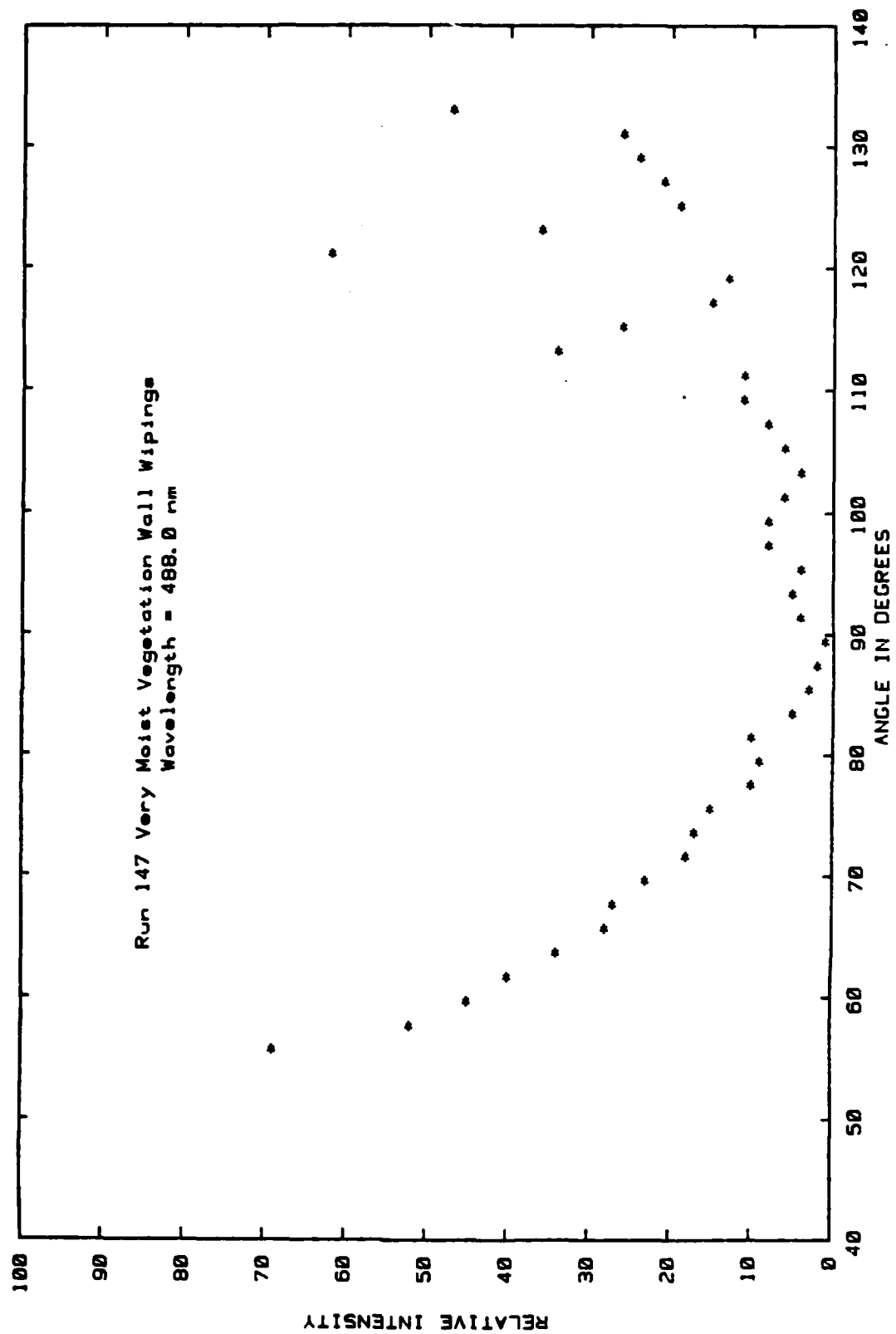


Figure A41. Experimental phase function data (*) for a particle from Run 147 for $\lambda = 488.0$ nm.

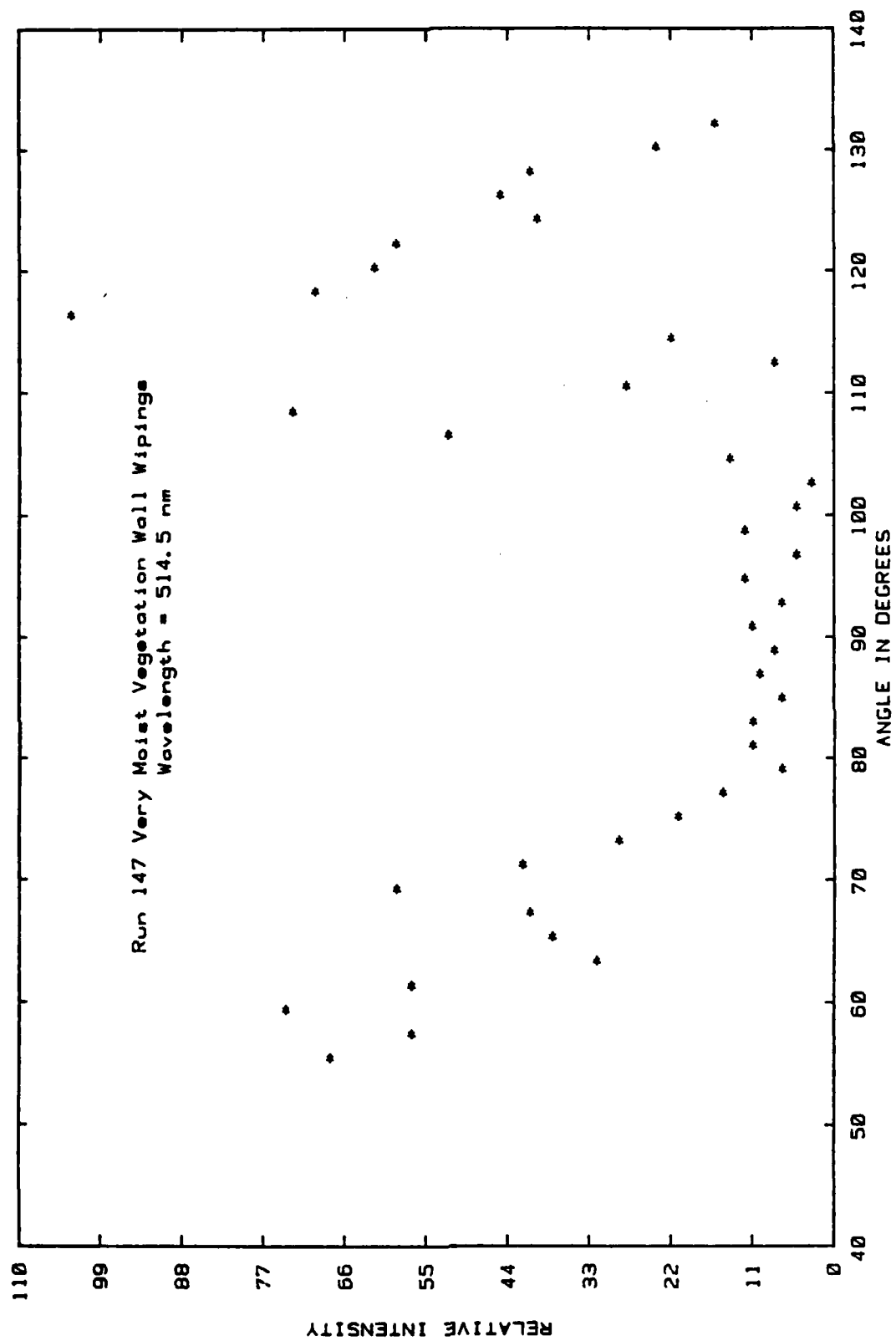


Figure A42. Experimental phase function data (*) for a particle from Run 147 for $\lambda = 514.5$ nm.

DEPARTMENT OF DEFENSE

Defense Intelligence Agency
ATTN: RTS-2A, Tech Library
ATTN: RTS-2B

Defense Nuclear Agency
ATTN: SPAS, G. Ullrich
4 cys ATTN: STTI-CA

Defense Technical Information Center
12 cys ATTN: DD

Field Command, Defense Nuclear Agency
ATTN: FCPR
ATTN: FCTT
ATTN: FCTT, W. Summa
ATTN: FCTXE

Joint Strat Tgt Planning Staff
ATTN: JLKS
ATTN: JPTM

Under Secy of Def for Rsch & Engrg
ATTN: Strat & Space Sys (OS)
ATTN: Strat & Theater Nuc For, F. Vajda

DEPARTMENT OF THE ARMY

BMD Advanced Technology Center
ATTN: ATC-T

BMD Systems Command
ATTN: BMDSC-LEE, R. Webb

Harry Diamond Laboratories
ATTN: DELHD-NM-P
ATTN: DELHD-TA-L, 81100, Tech Library

US Army Ballistic Research Lab
ATTN: DRDAR-BLA-S, Tech Library
ATTN: DRDAR-BLT, J. Keefer

US Army Corps of Engineers
ATTN: DAEN-ECE-T

US Army Engineer Ctr & Ft Belvoir
ATTN: Tech Library

US Army Engineer Div, Huntsville
ATTN: HNDE-FO

US Army Nuclear & Chemical Agency
ATTN: Library
ATTN: MONA-WE, J. Uecke

DEPARTMENT OF THE NAVY

Naval Research Laboratory
ATTN: Code 4040, D. Book
ATTN: Code 4040, J. Boris
ATTN: Code 2627, Tech Library

Naval Surface Weapons Center
ATTN: Code F31
ATTN: Code R44, H. Glaz
ATTN: Code X211, Tech Library

DEPARTMENT OF THE NAVY (Continued)

Naval Surface Weapons Center
ATTN: Tech Library & Info Svcs Br

DEPARTMENT OF THE AIR FORCE

Air Force Institute of Technology
ATTN: Library

Air Force Weapons Laboratory
ATTN: NTED-A
ATTN: SUL

Assist Ch of Staff, Studies & Analysis
ATTN: AF/SAMI, Tech Info Div

Ballistic Missile Office/DAA
ATTN: ENBF, D. Gage
ATTN: ENSN
ATTN: MGEN, A. Schenker
ATTN: PP

Strategic Air Command
ATTN: NRI/STINFO

DEPARTMENT OF ENERGY

Los Alamos National Laboratory
ATTN: C. Keller
ATTN: M. Sandford
ATTN: R. Whitaker

Sandia National Laboratories
ATTN: Div 1111, J. Reed
ATTN: J. Bannister
ATTN: Org 7112, A. Chabal

OTHER GOVERNMENT AGENCY

Central Intelligence Agency
ATTN: OSWR/NED

DEPARTMENT OF DEFENSE CONTRACTORS

Acurex Corp
ATTN: C. Wolf

Aerospace Corp
ATTN: H. Mirels
ATTN: Library Acquisition M1/199

Applied Research Associates, Inc
ATTN: N. Higgins

Applied Research Associates, Inc
ATTN: D. Peipenburg

Applied Theory, Inc
ATTN: J. Trulio

Boeing Co
ATTN: Aerospace Library
ATTN: S. Strack

California Research & Technology, Inc
ATTN: K. Kreyenhagen
ATTN: Library

DEPARTMENT OF DEFENSE CONTRACTORS (Continued)

California Research & Technology, Inc
ATTN: F. Sauer

Carpenter Research Corp
ATTN: H. Carpenter

University of Denver
ATTN: Sec Officer for J. Wisotski

H&H Consultants, Inc
ATTN: J. Haltiwanger
ATTN: W. Hall

H-Tech Labs, Inc
ATTN: B. Hartenbaum

Kaman Sciences Corp
ATTN: R. Ruetenik

Kaman Tempo
ATTN: DASIAC

Kaman Tempo
ATTN: DASIAC

McDonnell Douglas Corp
ATTN: H. Herdman
ATTN: R. Halprin

Mission Research Corp
ATTN: C. Longmire

University of New Mexico
ATTN: G. Leigh
2 cys ATTN: D. Calhoun

University of New Mexico
ATTN: J. Kovarna

Nichols Research Corp, Inc
ATTN: N. Byrn

Pacific-Sierra Research Corp
ATTN: H. Brode, Chairman SAGE

Pacific-Sierra Research Corp
ATTN: D. Gormley

Pacfica Technology
ATTN: R. Allen
ATTN: Tech Library

Patel Enterprises, Inc
ATTN: M. Patel

Physical Research, Inc
ATTN: R. Deliberis
ATTN: W. Mendes

Physics International Co
ATTN: H. Wampler

DEPARTMENT OF DEFENSE CONTRACTORS (Continued)

R&D Associates
ATTN: A. Kuhl
ATTN: P. Haas
ATTN: Tech Info Center

Rand Corp
ATTN: B. Bennett

S-CUBED
ATTN: C. Dismukes
ATTN: J. Barthel
ATTN: K. Pyatt
ATTN: Library

S-CUBED
ATTN: C. Needham

Science & Engrg Assoc, Inc
ATTN: B. Chambers

Science Applications International Corp
ATTN: G. Binninger

Science Applications Intl Corp
ATTN: H. Wilson
ATTN: R. Schlaug
ATTN: Tech Library

Science Applications Intl Corp
ATTN: J. Cockayne
ATTN: W. Layson

SRI International
ATTN: G. Abrahamson
ATTN: J. Colton
ATTN: Library

Teledyne Brown Engineering
ATTN: B. Hartway
ATTN: D. Ormond
ATTN: F. Leopard

TRW Electronics & Defense Sector
ATTN: N. Lipner
ATTN: Tech Info Center

TRW Electronics & Defense Sector
ATTN: E. Wong
ATTN: G. Hulcher
ATTN: P. Dai

University of Washington
2 cys ATTN: E. Davis
2 cys ATTN: R. Periasamy

Weidlinger Assoc, Consulting Engrg
ATTN: I. Sandler

END

Dtic

5-86